(Corrected Copy)

Development of Nanoscale Magnetic Systems for Spin Wave Propagation

Thesis submitted for the degree of

DOCTOR OF PHILOSOPHY (TECHNOLOGY)

in

NANOTECHNOLOGY

by

DHEERAJ KUMAR

CENTER FOR RESEARCH IN NANOSCIENCE AND NANOTECHNOLOGY
UNIVERSITY OF CALCUTTA

2014

Dedicated to Nanaji, whose stories I am made of . . .

Acknowledgements

I would like to begin by expressing my sincere gratitude to my guide and mentor, Prof. Anjan Barman for giving me the wonderful opportunity to work under his supervision. It was a great pleasure and honour to conduct research under his guidance in a competitive and yet friendly environment. I had backgrounds in mechanical engineering, fabrication and software development. He first introduced me to the realms of solid state physics, nanotechnology and magnonics. He gave me enough time to learn the ropes at my own pace without sacrificing my prior knowledge. This helped me qualify the national eligibility test in physical sciences, which eventually lead to my fellowship.

When I joined his fledgeling team as a doctoral candidate on 14$^{\text{th}}$ September, 2009, we essentially started from empty laboratory spaces. It is due to his incredible skills as a scientist and group leader that we were able to expand so rapidly and eventually ended up with publications in several prestigious peer–reviewed journals. Our labs now have strong funding and state of the art equipment. We can now perform in-house sample fabrication with several sputtering, lithography and chemical synthesis techniques. Experimental facilities include MOKE, TR–MOKE, VNA–FMR and BLS setups which he basically built himself to probe magnetization dynamics in different ways. A host of computers are dedicated to simulate problems and analyse results.

Under his wise tutelage, I also learned several skills directly related to the publication and presentation of ones output, which are necessary to be successful as an independent scientist. Like many of his students, I strove to inherit all the attributes of good scientist from him. He also encouraged me to leverage my diverse background and use the tools that I possessed to come up with new techniques and ideas. I hope to repay a fraction of this massive debt by building upon these learnings and sharing them with my own batch of students some day to become a part of the grand *guru–shishya* tradition. Apart from demonstrating what it takes to build a laboratory, he also trained all his students in its proper maintenance. He always motivated me to work hard and think independently. He provided me with several collaborative research opportunities so that I may also learn to make myself useful as a part of a team and contribute to the generation of new knowledge from a whole new platform. He gave me a lot of autonomous control over the manner in which I was to overcome my challenges. To cherish and enhance that kind of trust in me has been my strongest source of motivation during my life as a doctoral researcher.

I am also thankful to Dr. Saswati Barman for initiating me in the ways of micromagnetic simulations and magnetic vortex dynamics. She helped me in developing our own Landau–Lifshitz-Gilbert equation solver in MATLAB. The prompt completion of this deliverable was key in my transition from a software developer to a researcher.

Next, I would like to thank my colleges and collaborators. The first names among those are that of Dr. Jarosłow Kłos and his team leader Dr. Maciej Krawczyk. They developed the plane wave method to obtain the dispersion relation of spin–waves in magnonic crystals;

while I calculated the same using complete micromagnetic simulations. Agreements and disagreements between our results have granted us new insights into the dynamics of spin–waves. I would also like to acknowledge Dr. Oleksandr Dmytriiev, who carefully observed some of my initial results and provided very helpful inputs. Dr. Sabareesan Ponraj helped me with technicalities involving the preparation of a manuscript itself. He along with Weiwei Wang and Dr. Hans Fanghor did simulations using Nmag and also shared their knowledge of the finite element method.

Bivas Rana helped me set up my life in Kolkata. Semanti Pal is a fierce researcher and a wonderful human being who also helped me learn OOMMF. They, along with Bipul Kumar Mahato and Ruma Mandal are some of the experimentalists in our group who tested my numerical tools and validated them experimentally while generating new knowledge on their own. Dr. Michael Donahue helped me understand the inner workings of OOMMF. Susmita Saha, Dr. Arabinda Haldar and Dr. Pinkai Laha helped me in sample fabrication and TR–MOKE measurements. I also received training in advanced fabrication procedures from groups led by Profs. P. S. Anil Kumar and Yoshi–Chika Otani at IISc Bangalore and RIKEN, respectively. Discussions with Milan Agrawal, Profs. Abhihit Mookerjee and Partha Guha also proved to be valuable.

I would also like to acknowledge the moral support from my mother Mrs. Usha Rakesh and sisters Dr. Deepti Sharma and Ms. Tripti Sharma. Unlike my father, they showed great restraint and hardly ever bothered me with the annoying question about when will all this be over! I understand that all their actions, including those of my father's, were guided by my best interests at their hearts. Deepti's decision to pursue doctoral research had also encouraged mine. Her advice also came in handy on different occasions. Tripti is studying the law. She advised me — free of charge, of course — on how to apply for a patent. I must also thank my wife Prachi, for her exceptional moral support.

Finally, I thank the S. N. Bose National Centre for Basic Sciences for giving me an opportunity to work here. The common research facilities under the Technical Cell were very helpful for initial characterization of my samples. Thanks to Council of Scientific and Industrial Research for providing me with the Senior Research Fellowship. I must thank various funding agencies including the Departments of Science and Technology and Information Technology (Government of India) and the European Union's Seventh Framework Programme for their financial support of my research work.

Dheeraj Kumar,
S. N. Bose National Centre for Basic Sciences,
Salt Lake, Kolkata, India.

Patent and Publications

Patent Title: *A Spin Wave Waveguide with Bandgaps in the Microwave and Submillimeter Wave Frequency Bands*
Inventors: *Mr. Dheeraj Kumar and Prof. Anjan Barman*
Country of Application: *India*
Status: *Applied for* (September 2013)

This thesis is based upon the following peer–reviewed publications and manuscripts:

1. Numerical calculation of spin wave dispersions in magnetic nanostructures
   D. Kumar, O. Dmytriiev, S. Ponraj and A. Barman
   J. Phys. D: Appl. Phys. **45**, 015001 (2012).

2. Effect of magnetization pinning on the spectrum of spin waves in magnonic antidot waveguides
   J. W. Kłos, **D. Kumar**, J. Romero–Vivas, H. Fangohr, M. Franchin, M. Krawczyk and A. Barman
   Phys. Rev. B **86**, 184433 (2012).

3. Proposal for a Standard Micromagnetic Problem: Spin Wave Dispersion in a Magnonic Waveguide
   G. Venkat, **D. Kumar**, M. Franchin, O. Dmytriiev, M. Mruczkiewicz, H. Fangohr, A. Barman, M. Krawczyk and A. Prabhakar
   IEEE Trans. Magn. **49**, 015001 (2013).

4. Effect of hole shape on spin-wave band structure in one-dimensional magnonic antidot waveguide
   D. Kumar, P. Sabareesan, W. Wang and H. Fangohr and A. Barman
   J. Appl. Phys. **114**, 023910 (2013).

5. Magnonic Band Engineering by Intrinsic and Extrinsic Mirror Symmetry Breaking in Antidot Spin-Wave Waveguides
   J. W. Kłos,* **D. Kumar**,* M. Krawczyk and A. Barman
   Sci. Rep. **3**, 2444 (2013).

6. Influence of structural changes in a periodic antidot waveguide on the spin-wave spectra
   J. W. Kłos,* **D. Kumar**,* M. Krawczyk and A. Barman

Phys. Rev. B **89**, 014406 (2014)

7. Magnonic Band Structure, Complete Bandgap and Collective Spin Wave Excitation in Nanoscale Two–Dimensional Magnonic Crystals
D. Kumar,* J. W. Kłos,* M. Krawczyk and A. Barman
J. Appl. Phys. **115**, 043917 (2014)

8. Magnetic Vortex Based Transistor Operations
D. Kumar, S. Barman and A. Barman
Sci. Rep. **4**, 4108 (2014).

9. Development of Nanoscale Systems for Spin–Wave Propagation
D. Kumar and A. Barman *To be Submitted.*

The following co–authored publications are not included in this thesis:

1. Detection of Picosecond Magnetization Dynamics of 50 nm Magnetic Dots down to the Single Dot Regime
B. Rana, **D. Kumar**, S. Barman, S. Pal, Y. Fukuma, Y. Otani and A. Barman
ACS Nano **5**, 9559 (2011).

2. Optically Induced Tunable Magnetization Dynamics in Nanoscale Co Antidot Lattices
R. Mandal, S. Saha, **D. Kumar**, S. Barman, S. Pal, K. Das, A. K. Raychaudhuri, Y. Fukuma, Y. Otani and A. Barman
ACS Nano **6**, 3397 (2012).

3. Anisotropy in collective precessional dynamics in arrays of $Ni_{80}Fe_{20}$ nanoelements
B. Rana, **D. Kumar**, S. Barman, S. Pal, R. Mandal, Y. Fukuma, Y. Otani, S. Sugimoto and A. Barman
J. App. Phys. **111**, 07D503 (2012).

4. Tunable Magnonic Spectra in Two-Dimensional Magnonic Crystals with Variable Lattice Symmetry
S. Saha, R. Mandal, S. Barman, **D. Kumar**, B. Rana, Y. Fukuma, S. Sugimoto, Y. Otani and A. Barman
Adv. Funct. Mater. **23**, 2378 (2013).

5. Configurational anisotropic spin waves in cross-shaped $Ni_{80}Fe_{20}$ nanoelements
B. K. Mahato, B. Rana, R. Mandal, **D. Kumar**, S. Barman, Y. Fukuma, Y. Otani and A. Barman
Appl. Phys. Lett. **102**, 192402 (2013).

*These authors contributed equally to the work.

6. Micromagnetic study of size–dependent picosecond dynamics in single nanomagnets
   S. Pal, **D. Kumar**, and A. Barman
   J. Phys. D: Appl. Phys. **44**, 105002 (2011).

Abstract

It has been proposed that spin–waves, particularly those with frequencies in microwave and submillimetre wave bands, can be used for information transmission and processing. Having shorter wavelengths as compared to electromagnetic waves of the same frequency, spin–wave based devices hold the potential to aid the miniaturization of microwave communication. Designs have been proposed which use nanoscale magnetic systems to create elements which can function as attenuators, filters, phase–shifters, interferometers and logic gates. Here, we study the magnetization dynamics of spin–wave dispersion and magnetic vortex gyration. Both phenomenon are related and have their characteristic frequencies in the microwave frequency band. The nanoscale systems considered here are ferromagnetic thin films, uniform waveguides, magnonic crystals (spatially modulated magnetic systems) and magnetic vortices. Effects like magnetization pinning and mirror symmetry breaking, which alter the spin–wave dispersion characteristic call for greater spatial resolution and precision in fabrication. Thus, we summarize with what needs to be done and the future directions the research needs to take in order to make nanoscale devices technically feasible.

The spectrum of spin–waves propagating in magnetic systems is important from both fundamental and applied points of views. Propagating spin–waves in magnonic crystals will form the building blocks of future microwave data processing and communication. While magnonic modes and band gaps can help in the formulation of filters and attenuators, understanding other phenomena like spin–wave reflection, refraction and interference will help in designing magnonic circuit elements like logic gates and diodes.

The Landau–Lifshitz–Gilbert (LLG) equation has been used in this work to simulate the spin dynamics in different nanoscale magnetic systems. This equation was solved mainly using the finite difference method based Object–Oriented Micromagnetic Framework (OOMMF) or the finite element method based Nmag. In addition to using some existing software packages, we also developed our own LLG equation solver (which can also take spin–transfer torque terms into account) using MATLAB programming. The combined packages of simulation and post–processing has been named DotMag. DotMag can simulate spin dynamics in two–dimensional systems and can analyse results for any kind of nanoscale system — even those solved using third party packages, such as OOMMF. The results obtained from the newly developed software have been inspected for any magnonic bands and bandgaps using multi–domain discrete Fourier transform. Various issues related to the numerical calculations like aliasing, spectral leakage and scalloping loss have been addressed in Chap. 3. The tools prepared for analysing these magnonic conductors will also allow for the visualization of propagation and power and phase distribution of the spin–wave over the entire region of interest. These tools will be generically designed, so as to accommodate any kind of magnonic conductor.

The newly developed package DotMag, was used for the calculations of magnonic band structures of one– and two–dimensional periodic arrays of dots, anti-dots (holes created in

continuous magnetic medium) and filled antidots (the holes are now filled with a different magnetic medium). Influence of different structural and material parameters over the spin–wave band structure was studied in these cases. The results obtained using the micromagnetic simulations were also compared with those obtained from the plane wave method (PWM) and any differences were examined. Iso–frequency lines, which are magnonic analogues of the electronic Fermi surfaces were also calculated in the case of two–dimensional antidot arrays. With the knowledge obtained from above we investigated magnonic waveguides embedded with regular and filled antidots to design magnonic filters of tunable bandwidth and bandgaps. Some of the numerically examined magnonic crystals have been fabricated by using different lithography techniques. The low wavevector magnonic modes in some of these magnonic crystals were experimentally investigated by using our TR–MOKE experimental setup.

In Chap. 5, we study the spin–wave spectra in magnonic antidot waveguides (MAWs) versus the surface anisotropy at the ferromagnet/air interface. The MAWs under investigation have the form of a thin stripe of permalloy with a single row of periodically arranged antidots in the middle. The introduction of a magnetization pinning at the edges of the permalloy stripe and the edges of antidots is found to modify quantitatively the spin–wave spectrum. This effect is shown to be necessary for magnonic gaps to open in the considered systems. Our study demonstrates that the surface anisotropy can be crucial in the practical applications of MAWs and related structures and in the interpretation of experimental results in one- and two-dimensional magnonic crystals. We used three different theoretical methods *i.e.* PWM, finite difference method and finite element method to validate the results. We showed that PWM in the present formulation assumes pinned magnetization while in micromagnetic simulations special care must be taken to introduce pinning.

In Chap. 6, we show that structural changes breaking the mirror symmetry of a MAW can close the magnonic bandgaps. But, the effect of these intrinsic symmetry breaking factors can be compensated by a properly adjusted asymmetric external bias magnetic field, *i.e.*, by an extrinsic factor. This allows for the recovery of the magnonic bandgaps occurring in the ideal symmetric structure. The described methods can be used for developing parallel models for recovering bandgaps closed due to an intrinsic defect, *e.g.* a fabrication defect. The theoretical model developed here is particular to the field of magnonics, a rapidly emerging field combining spin dynamics and spintronics. However, the underlying principle of this development is squarely based upon the translational and mirror symmetries associated with the crystal structure. Thus, we believe that this idea of correcting an intrinsic defect by extrinsic means, should be applicable to spin–waves in both exchange and dipolar interaction regimes, as well as to electron, electromagnetic and acoustic waves in general.

In Chap. 7, we present the possibility of tuning the spin–wave band structure, particularly the bandgaps in a nanoscale MAW by varying the shape of the antidots. The effects of changing the shape of the antidots on the spin–wave dispersion relation in a waveguide have been carefully monitored. We interpret the observed variations by analysing the equilibrium magnetic configuration and the magnonic power and phase distribution profiles during spin–wave dynamics. The inhomogeneity in the exchange fields at the antidot boundaries within the waveguide is found to play a crucial role in controlling the band structure at the discussed length scales. The observations recorded here will be important for future developments of magnetic antidot based magnonic crystals and waveguides.

In Chap. 8, we demonstrate that the magnonic band structure, including the band gap for a MAW, can be significantly tuned by a relatively weak modulation of its structural parameters. The calculations were performed with consideration of both the exchange and dipolar interactions. For the exchange dominated regime, we discuss, in details, the impact of the changes of the lattice constant, size, and shape of the antidots on the spin–wave spectra. We have shown that a precise choice of these parameters is crucial for achieving desired properties of the antidot waveguides, *i.e.*, a large group velocity and filtering properties due to existence of magnonic band gaps. We discuss different mechanisms of magnonic gap opening resulting from Bragg scattering or anticrossing of modes. We have shown that the dipolar interactions start to assert their role in the spin–wave spectrum when the waveguide is scaled up, but even for a period of few hundreds of nanometres, the magnonic band structure preserves qualitatively the properties found in the exchange dominating regime. The obtained results are important for future development of magnonic crystal based devices.

In Chap. 9, we present the observation of a complete bandgap and collective spin–wave excitation in two–dimensional magnonic crystals comprised of arrays of nanoscale antidots and nanodots, respectively. Considering that the frequencies dealt with here fall in the microwave band, these findings can be used for the development of suitable magnonic metamaterials and spin–wave based signal processing. We also present the application of a numerical procedure, to compute the dispersion relations of spin–waves for any high symmetry direction in the first Brillouin zone. The results obtained from this procedure has been reproduced and verified by the well–established PWM for an antidot lattice, when magnetization dynamics at antidot boundaries is pinned. The micromagnetic simulation based method can also be used to obtain iso–frequency contours of spin–waves. Iso–frequency contours are analogous of the Fermi surfaces and hence, they have the potential to radicalise our understanding of spin–wave dynamics. The physical origin of bands, partial and full magnonic bandgaps has been explained by plotting the spatial distribution of spin–wave energy spectral density. Although, unfettered by rigid assumptions and approximations, which afflict most analytical methods used in the study of spin–wave dispersion, micromagnetic simulations tend to be computationally demanding. Thus, the observation of collective spin–wave excitation in the case of nanodot arrays, which can obviate the need to perform simulations may, also prove to be valuable.

DotMag was developed with the ability to excite vortex core gyration by using external magnetic field and spin transfer torque. Magnetic vortex dynamics was investigated in the cases of isolated and coupled vortices. Transducer and transistor like operations were demonstrated based on these results. Transistors constitute the backbone of modern day electronics. Since their advent, researchers have been seeking ways to make smaller and more efficient transistors. In Chap. 12, we demonstrate a sustained amplification of magnetic vortex core gyration in coupled two and three vortices by controlling their relative core polarities. This amplification is mediated by a cascade of antivortex solitons travelling through the dynamic stray field. We further demonstrated that the amplification can be controlled by switching the polarity of the middle vortex in a three vortex sequence and the gain can be controlled by the input signal amplitude. An attempt to show fan–out operation yielded gain for one of the symmetrically placed branches which can be reversed by switching the core polarities of all of the vortices in the network. The above observations promote the magnetic vortices as suitable candidates to work as stable bipolar junction transistors (BJT).

Contents

List of Abbreviations

1D : One–Dimensional.

2D : Two–Dimensional.

3D : Three–Dimensional.

ADL : AntiDot Lattice.

BV : Backward Volume.

BZ : Brillouin Zone.

CAD : Computer Aided Design.

CCD : Charged Coupled Diode.

CMOS : Complementary Metal–Oxide–Semiconductor.

CW : Clockwise.

CCW : Counter–Clockwise.

Co : Cobalt.

DE : Damon–Eshbach.

DFT : Discrete Fourier Transform.

ESD : Energy Spectral Density.

FDM : Finite Difference Method.

FEM : Finite Element Method.

FFT : Fast Fourier Transform.

FIB : Focused Ion Beam.

FV : Forward Volume.

LLG : Landau–Lifshitz–Gilbert.

MAW : Magnonic Antidot Waveguide.

MC : Magnonic Crystal.

MMA : Methyl MethAcrylate.

MRAM : Magnetic Random Access Memory.

MS : Micromagnetic Simulation.

OBD : Optical Bridge Detector.

ODE : Ordinary Differential Equation.

OOMMF : Object Oriented MicroMagnetic Framework.

PBC : Periodic Boundary Condition.

PPDP : Power and Phase Distribution Profile.

PMMA : PolyMethyl MethAcrylate.

PWM : Plane Wave Method.

PVFT : Precessing Vector Fourier Transform.

Py : Permalloy ($Ni_{80}Fe_{20}$).

SEM : Scanning Electron Microscopy.

SHG : Second Harmonic Generator.

STT : Spin–Transfer Torque.

SW : Spin–Wave.

TR–MOKE: Time–Resolved Magneto–Optic Kerr Effect.

YIG : Yttrium Iron Garnet.

w.r.t. : with respect to.

List of Commonly Used Symbols*†

Γ	: Centre of the Brillouin zone.
μ_{B}	: Bohr magneton.
α	: Gilbert damping.
γ, $\lvert\bar{\gamma}\rvert$, $\lvert\gamma\rvert$	: Gyromagnetic ratio.
μ_0	: Magnetic permeability of free space.
μ_{B}	: Bohr magneton.
θ^f	: Phase of SWs.
ω	: SW angular frequency.
A	: Exchange coefficient.
$\mathbf{H}_{\mathrm{anis}}$	: Anisotropy field.
$\mathbf{H}_{\mathrm{bias}}$	: Bias field.
$\mathbf{H}_{\mathrm{dem}}$	: Demagnetizing field.
$\mathbf{H}_{\mathrm{eff}}$	: Effective field.
$\mathbf{H}_{\mathrm{exch}}$	: Exchange field.
$\mathbf{H}_{\mathrm{ext}}$	: External field.
$\mathbf{H}_{\mathrm{sig}}$	: Excitation signal.
J	: Total angular momentum quantum number.
K_1, K_2, K_1', K_2'	: Magneto–crystalline anisotropy.
$\mathbf{M}$	: Magnetization.
M_{s}	: Saturation magnetization.
$\mathbf{m}$	: $\mathbf{M}/M_{\mathrm{s}}$.
S^f	: Energy spectral density of SWs.

*These symbols are used to mean the following, unless stated otherwise in a chapter.

†Magnitude of vector quantities has been represented by the italicized non–boldface version of its symbol.

f : SW frequency.

h; $\hbar$: Plank constant; Reduced Plank constant.

$\mathbf{k}$: SW wavevector.

k_{B} : Boltzmann constant.

k_x : x–component of SW wavevector.

k_y : y–component of SW wavevector.

k_z : z–component of SW wavevector.

t : Time.

u : Film or waveguide thickness.

w : Width of waveguide or sub–waveguide.

x : x–coordinate.

y : y–coordinate.

z : z–coordinate.

Material Parameters Used During Simulations*

Material	$M_s(10^6)$ A/m	$A(10^{-12})$ J/m	$K1(10^3)$ J/m^3	α
Co	1.4	30	520	10^{-4}
Py	0.8	13	0	10^{-4}

*Gyromagnetic ratio $|\bar{\gamma}| = 2.21 \times 10^5$ m A^{-1} s^{-1} is used in all cases. Gilbert damping $\alpha = 0.9$ or 0.95 is used to develop the steady state before starting the magnetization dynamics; which is observed at low values of 10^{-4} to obtain sharper peaks in the frequency domain. Where specified, more realistic values of $\alpha = 0.008$ or 0.01 is used.

List of Tables

List of Figures

1. Introductions

Magnetization dynamics at nanoscale had been predicted to be characterized by a few interesting phenomena, which are deemed useful for practical applications such as information transmission, processing and storage. For example, the theorization of some key aspects of spin–waves (SWs) occurred over fifty years ago.[1,2] Recent advances in fabrication techniques have allowed for the examination of such phenomena on micro– and nanoscale. As SWs of microwave frequency have considerably lower wavelengths (in comparison to light), the potential to miniaturize microwave communication appears to be the guiding motivation of most of the recent studies. SWs can be more dispersive than sound or light waves and have a band structure which typically starts at a certain non–zero minimum frequency. SW dispersion is also anisotropic in most cases. The ability to alter the response of nanoscale magnetic structures simply by controlling the external field has also attracted a lot of attention.[3,4] The characteristic time scales τ, of different manifestations of magnetization dynamics can be obtained using the Heisenberg relation $\tau = h/E$, where h is the Planck constant and E is the involved interaction energy.[5] This has been presented in Fig. 1.1.

As seen from Fig. 1.1, the exchange interaction, which favours the parallel alignment of spins in a ferromagnet, has a characteristic time–scale between one and ten femtoseconds. The effects of spin–orbit coupling and spin–transfer torque (STT) are apparent under a picosecond. Laser induced ultrafast demagnetization can typically be obtained within a few hundred femtoseconds.[6] The precession of magnetization[7] and its (Gilbert) damping[8] feature a timespan of one picosecond to tens of nanoseconds (see Fig. 1.1). SWs have the similar characteristic time–scales depending upon the strength of the damping. The phenomena of magnetic vortex core gyration[9] has a characteristic timespan of one nanosecond to tens of nanoseconds. The movement of magnetic domain walls, on the other hand, occurs in a

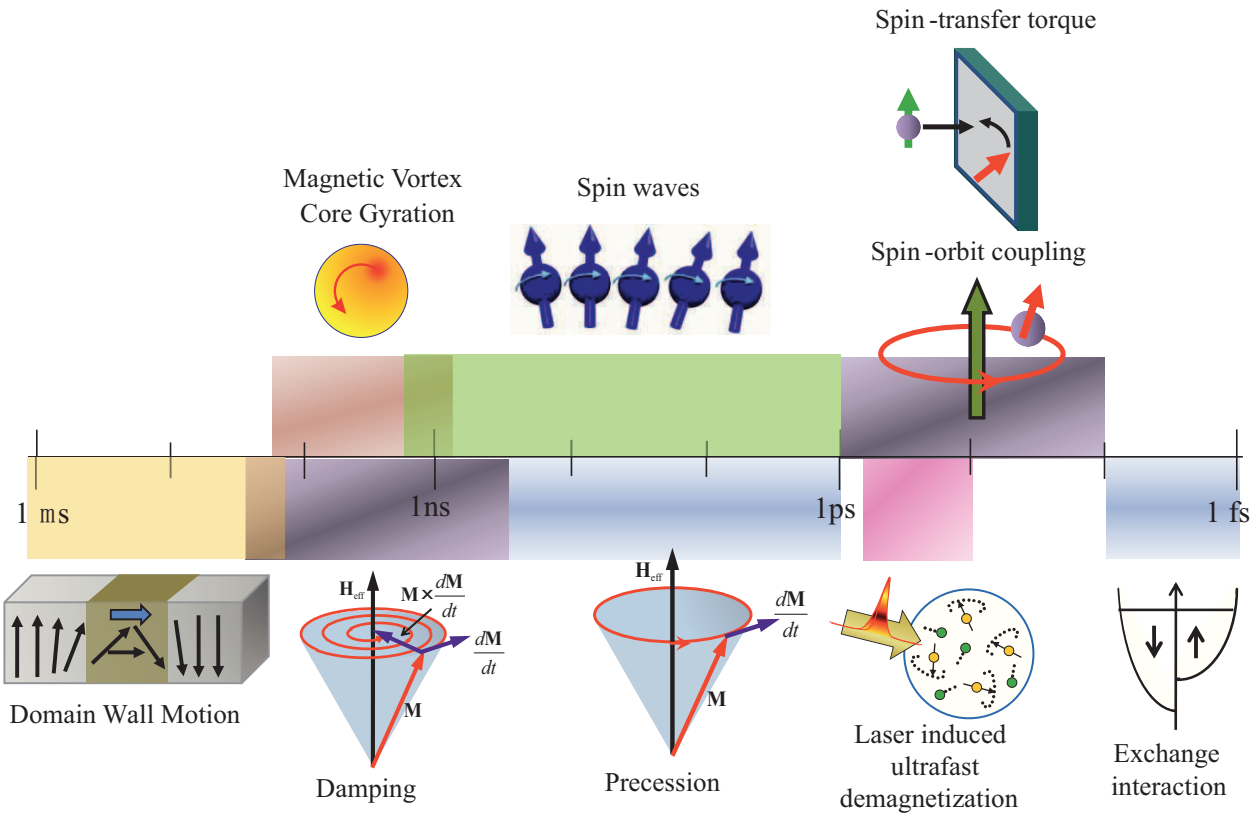

Figure 1.1.: Characteristic time scales for different manifestations of magnetization dynamics. Source: Ref. 5.

time–scale above 10 ns.

The focus of this thesis is to study SWs and magnetic vortex dynamics in nanoscale systems. As seen from Fig. 1.1,[6] these two roughly span the microwave and the submillimetre wave frequency bands. These two forms of magnetization dynamics are also very closely related in theory. Nanoscale magnetic systems exhibit interesting phenomena, such as, giant magnetoresistance,[10,11] giant Faraday rotation[12] and high out–of–plane magnetic anisotropy.[13,14] Current nanofabrication techniques give us the ability to create systems with artificial periodic modulation with high spatial resolution. SW propagating through such artificial mediums feature a characteristic spectrum complete with bands and *bandgaps* – forbidden regions in frequency domain. To this end, SW dynamics has been studied in nanoscale ferromagnetic systems such as thin–films, uniform and patterned waveguides, and nanodot and antidot arrays. *Antidots* are holes in planer ferromagnetic structures. Bi–component waveguides, where the antidots are replaced with another ferromagnet, have also been considered. Dynamics of magnetic vortices, which can also be used for the generation of

SWs[15] along with very efficient signal transmission and logical operations, have been studied in isolated and dipole coupled ferromagnetic nanodisks.

1.1. Spin–Waves

If the local magnetization $\mathbf{M}$ of a ferromagnet gets misaligned with the effective field $\mathbf{H}_{\text{eff}}$, it experiences a torque leading to its precession. The precessing magnetization vector also changes its surrounding exchange and dipolar fields and spreads the information of the original misalignment of effective field to its neighbourhood. Owing to spin–orbit coupling and several other factors (like spin diffusion, magnon–phonon interaction, etc.[16]) the precession slowly gets damped. The processes of magnetization precession and its damping can be modelled using the Landau–Lifshitz–Gilbert (LLG) equation. Since the LLG equation describes the magnetization dynamics in terms of incremental changes in the magnetization vector, they can model any given systems as long as the involved parameters, such as the saturation magnetization, do not vary greatly during the dynamics. Thus, phenomena like SW dynamics and magnetic vortex gyration, which occur above one picosecond in time–scale and one nanometre in length–scale can be described accurately by the LLG equation.[5] Theoretical details of this equation has been presented in sub–Sec. 2.3.2.

The Gilbert damping is preferred over the *Bloch–Bloembergen damping*[17] description while dealing with ferromagnets, as the former keeps the amplitude of magnetization constant with time.[18] Non–Gilbert type magnetization relaxation can also be introduced by magnon–magnon scattering[19,20] or spin–polarized current.[21] In this work, we focus only on the Gilbert type damping. In frequency domain analysis of various magnetization dynamics, damping manifests itself as line–width. As it causes the information in a signal to loose coherence, damping is considered undesirable in most cases. Some recently published literature[22,23] seeks to lower this damping by working with different types of materials. Long range coherence of SW edge modes has also been theorized in an insulating ferromagnet[24] and other nanoscale systems.[25]

The largest contributor to $\mathbf{H}_{\text{eff}}$ is typically the bias field $\mathbf{H}_{\text{bias}}$, while the SW is usually produced during a simulation by using the excitation signal $\mathbf{H}_{\text{sig}}$. To study the nature of

SWs generated with different bias directions, it is sometimes desirable to avoid the anisotropy field $\mathbf{H}_{\text{anis}}$ by using materials like permalloy (Py: $Ni_{80}Fe_{20}$) which have negligible magnetocrystalline anisotropy. Typically, a high bias field of strength (> 1 T) is used to completely saturate the Py medium. A high value of $\alpha \geq 0.9$ is used at the beginning of any simulations; so that the magnetic ground state may be achieved quickly. Later, α is reduced to an artificially low value of 10^{-4}; so that a better resolution may be obtained in the frequency domain during a Fourier analysis. Any deviations from these parameters will be explicitly stated.

When the information of the any misalignment between the effective magnetic field and the magnetization starts to propagate as a collective excitation, SWs are said to be generated.[1,26–28] SWs can also be produced by STT from spin polarized current.[29] Figure 1.2 depicts this wave as a green curve being traced by one of the dynamical components of magnetization $\mathbf{M}$. As in the case of photonic or phononic waves, SWs too are capable of carrying information in the form of energy and momentum.

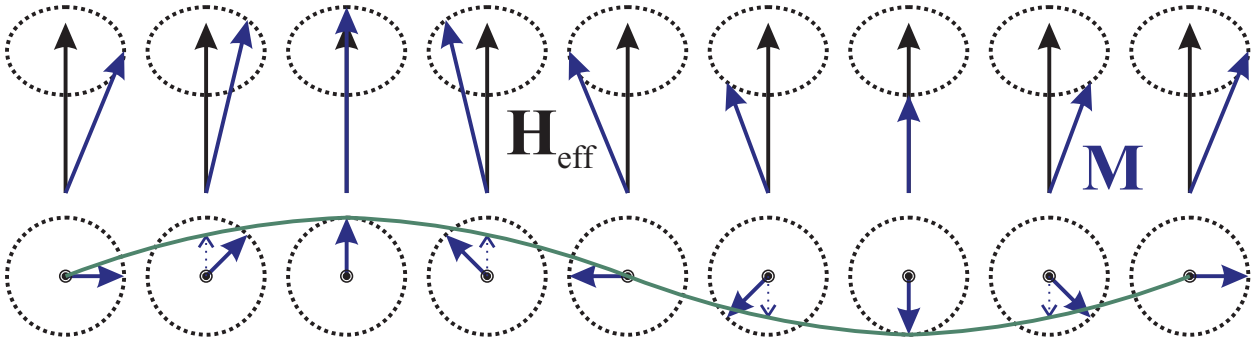

Figure 1.2.: (Top panel) Precession of blue magnetization $\mathbf{M}$ vector around the black effective field $\mathbf{H}_{\text{eff}}$ vector. Here the spins are arranged in an one–dimensional chain with discrete translational symmetry. (Bottom panel) Top view of the precessional dynamics showing an imaginary green wave–like curve being traced by one of the components of $\mathbf{M}$.

Magnons were theorized[2,30] as the quasi–particles associated with the quantization of SWs. Like photons or phonons, magnons too are classified as bosons.[31–33] The same, however, is not the case with electrons. Nevertheless, several techniques developed to study electrons, photons or phonons as information carriers can also be used in the case of magnons. Compared with light or sound waves, the dispersion relation in the case of SWs can be much easily controlled by controlling an extrinsic parameter — the external field,[4] even while the

SW dynamics is in progress.[3] This introduces the most significant advantage that a SW based system can have over its electronic, photonic or phononic analogues.

Magnonic crystals[34–39] (MCs) are metamaterials typically created by spatially modulating the magnetic parameters such as saturation magnetization, M_s or exchange coefficient, A[40–42] of a known material and where SWs are the transmission waves. MCs can be regarded as the magnonic analogues of photonic and phononic crystals. Knowledge of SW dispersion within such structures is necessary for their design and operation. An MC can be realized by a combination of periodic modulation of structural and material parameters of a magnetic material and a control over the external bias magnetic field.[40–42] This creates a periodic magnetic potential within an MC, which scatters the SWs eventually yielding a characteristic dispersion relation comprising of stop and pass bands. Most MCs that form the topic of current research in magnonics are either 1D[43,44] or 2D[45–50] as they are easier to fabricate on a wafer when compared to 3D MCs. Nevertheless, few theoretical reports on the study of dispersion of SWs in 3D MCs have been made.[2,51,52] Magnetic antidots arrays, which support higher group velocities (as compared to MCs based on dot arrays), have emerged as an important system of MCs; and a thorough investigation of high frequency magnetization dynamics in them have been reported in the literature.[50,53–59] Recently, the first MCs made by arranging two ferromagnetic materials with nanoscale discrete translational symmetry (bi–component MCs) have been fabricated[49] and bandgaps in their SW spectrum was experimentally verified.[60–62] Tunability of SW spectra based on the lattice symmetry in a 2D lattice of nanodots has also been reported.[63,64] 2D antidots lattices, formed by periodic array of holes in a ferromagnetic film, can be fabricated much easily. These systems have been intensively studied in recent years on different length–scales as well.[65,66]

For antidot lattices with large spatial periodicity,[66] the inhomogeneity of the internal magnetic field is decisive for the formation of the magnonic band structure.[67] With the decreasing period of antidot lattice the Brillouin zone (BZ) border will move to larger wave–vectors and the exchange interactions at some point will start to play a primary role in the formation of magnonic band structure.[68] Thus, based on the nature of this dependence SWs can be classified as *dipole–dominated* and *exchange–dominated*, respectively. Dipole–dominated SWs have wavelengths much greater than λ_{ex}, where $\lambda_{ex} = \sqrt{2A/(\mu_0 M_s^2)}$ is

the characteristic exchange length of the ferromagnetic medium. Typically, the wavelength of dipole–dominated SWs is in the order of a few microns. On the contrary, exchange–dominated SWs have wavelengths of the order of λ_{ex}. This value is commonly of the order of 5 nanometres. SWs with intermediate wavevector values are called *dipole–exchange* SWs.

Magnonics[37,38,69–71] is an emerging sub–field of solid state physics, which deals with the study of SWs and related aspects of magnetization dynamics. Magnonics is mainly aimed at exploiting the properties of SWs for technological applications in the fields of microwave systems, metamaterials for electromagnetic waves, spintronics, and other magnonic devices using SWs for information communication. Compared to microwave technology, the other three fields are relatively new and in their nascent stage.[69,72–75] Signal processing in electronic devices relies on the electronic band structure of semiconductors. Recent developments in silicon photonics, such as the cascaded Raman laser,[76] also exploit the discovery of suitable bands and bandgaps. Thus, one cannot proceed with the design or development of nanoscale *magnonic devices*[77,78] without the study SW band structure. The possibility of tailoring metallic magnetic materials with nanoscale precision provides a tool for miniaturization and shaping the dispersion of high–frequency SWs. Apart from magnonic crystals, waveguides,[79] SW interferometers[80–82] and phase shifters[83] are some of the important components of magnonic devices. Like photonic devices, magnonic devices too promise a lower power consumption compared to today's electronic devices. However, once an electronic or photonic device is designed, not much can be changed to alter its characteristics during operation. This, however is not the case with SW based devices whose characteristics can be changed extrinsically by the control of $\mathbf{H}_{\text{bias}}$.[3,4] Further, structured SW waveguides[84–86] have recently attracted considerable attention due to their selective transmission of microwave bands in the micro– and nano–scales and their potential applications in on–chip microwave signal processing and communication.

Prototypes of basic magnonic devices have already been demonstrated to be promising for technological applications,[3,69,70,73,87] but the scaling down of magnonic elements to tens of nanometres in size and tens to hundreds of GHz of operating frequencies[88–91] are still a challenge. Waveguides for SWs are deemed to be of vital importance in most magnonic devices.[69] Various forms of waveguides, such as, flat stripes having filtering properties due

to periodically modulated width[85] or based on a (missing) row defect in 2D MCs have been studied.[38,55,92–97] But so far, experiments are only done for SWs in the frequency range up to a few gigahertzs. Owing to the recent advances in fabrication techniques, it has become feasible to fabricate structures with resolution better than 10 nm. For example, the spot size during focused ion beam lithography can go below 10 nm with low ($\approx$ 30 pA) ion current.[50,98–100] To predict properties of magnonic devices at nanometre length scale, more basic research needs to be conducted. Therefore, theoretical investigation of the SW waveguides and MCs operating in the range of tens to hundreds of GHz is a frontier field of research.

Another topic of technological importance deals with the generation and detection of SWs on nanoscale. The interactions of magnons with electrons, photons and phonons have been exploited to generate and detect SWs. SWs can be produced by spin torque nano–oscillators[101,102] or spin–polarized current[103] or by using phenomenon such as spin–Hall effect[104] or spin–Seebeck effect[105–108] and they can be detected using the inverse spin–Hall effect.[109] SWs can also be generated by certain magnon–soliton interactions.[15] A time–resolved magneto–optic Kerr effect (TR–MOKE) experimental setup uses high energy photons to excite SWs[110–114] and low energy photons to detect them.[115–117] Any time–resolved measurement done on SWs should have a temporal resolution below one picosecond to account for SWs upto 500 GHz. Short bursts of terahertz SWs have been also optically excited in ferromagnetic[118,119] and anti–ferromagnetic[120,121] mediums, testifying to the quantum nature of magnons. A vector network analyzer[122,123] can be used to directly detect the SW spectra while a Brillouin light scattering setup[111,124,125] can be used to experimentally examine the SW dispersion relation in wavevector domain as well.

1.2. Magnetic Vortices

Micro– and nanoscale ferromagnetic disks can support a non–trivial spin configuration called a magnetic vortex,[126,127] which is another kind of magnetic system studied here with the view point of information processing. Magnetic vortices can find applications in magnetic data storage, magnetic random access memory,[128–131] magnetic logic circuitry,[132] information processing devices[132] or the detection of impurities in a magnetic material.[133] Often the

magnetization aligns itself along the boundaries of laterally confined geometries in order to minimize the energy stored in the stray field. This can lead to an anti–parallel arrangement of magnetization close to the centre of the geometry. Thus, in ferromagnetic circular nanodisks, the exchange interaction pushes the magnetization at the centre of the disk out of plane: either up or down. The sense of flux closed magnetization structure — clockwise (CW) or counter–clockwise (CCW) — represents the *chirality* of the vortex.[134] The part of the vortex with out of plane component is called its core which can support either 'up' or 'down' *polarity*.[135] The chirality and the polarity of the magnetic vortex can be seen in Fig. 1.3.[127]

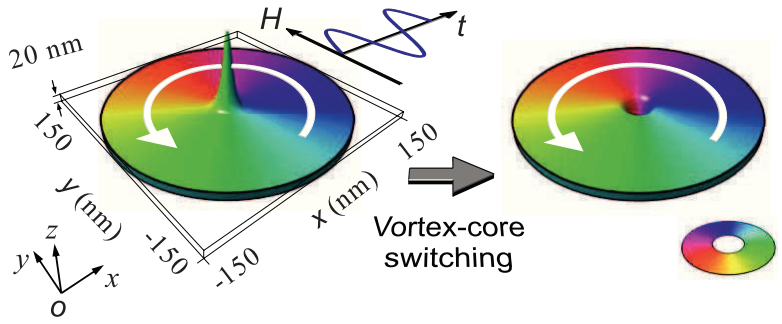

Figure 1.3.: Colour coded cyclic arrangement of magnetization in a magnetic vortex. The spikes in middle of the geometry represent the vortex core, which can be switched by applying an in–plane rotating magnetic field. Source: Ref. 127.

Apart from waveguides and MCs, micro- and nanomagnetic disks and rings are also useful in signal processing as they cover the sub-GHz regime, which is usually inaccessible by SWs. Resonating vortices, for example can be phase locked using SWs.[136] As seen in Fig. 1.3, magnetic vortex cores can be switched from 'up' to 'down' by the application of an external magnetic field. This polarity reversal can also be used for SW generation.[15] It can also be brought to gyration[137,138] by the application of the magnetic fields and spin polarized currents.[128,139–143] External magnetic fields and spin polarized currents couple to the magnetic moments of the vortex core and drive it away from the equilibrium position. In addition to these external forces, the displaced vortex core experiences an internal force arising from the demagnetizing field of the non–equilibrium magnetization pattern. This force attempts to restore the core to its equilibrium position, thus aiding the gyrotropic motion. For large amplitude excitation, the internal force increases nonlinearly and this results into a non linear vortex core gyration, and vortex core switching occurs along with creation and annihi-

lation of new vortex and antivortex.[144,145] For small amplitude excitation, the internal force increases linearly and the vortex core motion remains in the linear regime.[146] Apart from saturation magnetization, the natural gyration frequency of a magnetic vortex also depends on the aspect ratio (the ratio of disk's diameter and thickness) of the ferromagnetic disk.[147]

The presence of polarity dependent rotational asymmetry makes them very attractive candidates for studying the interaction between the local magnetization and externally applied magnetic fields or spin polarized currents.[139,148–157] The magnetization dynamics resulting in the gyrotropic vortex core motion can also be described by the LLG equation[8,158] (see sub–Sec. 2.3.2). In the linear regime, the vortex core equation of motion can be derived from the Thiele's equation.[146] The CW or CCW sense of vortex core gyration direction is solely controlled by its polarity. In the linear regime, vortex core can be described by a harmonic oscillator model.[159] Consequently, magnetostatically coupled vortex gyration can be considered as coupled oscillators. Therefore, one expects mutual energy transfer and a consistent phase relation between the gyrating vortices.[160,161] Logic operations based on magnetic vortex state networks have been demonstrated experimentally via the vortex gyration mediated information signal transfer mechanism.[162]

Subsequently, the mutual transfer of energy between magnetostatically coupled vortices where one of the vortices is locally excited is extremely important for microwave communication and logic operations. In this regard, the parameters like the signal transport rate and efficiency are the key factors in determining the device performance. Vortex gyration transfer rate and energy attenuation coefficients have been calculated by analytical method and micromagnetic simulations.[163] Stimulated vortex gyration based energy transfer between spatially separated dipolar coupled magnetic disks has been observed by time resolved soft x-ray microscopy.[155] The rate of energy transfer is found to be determined by the frequency splitting caused by the dipolar interaction between the vortices.[162]

This energy transfer efficiency may depend on several factors such as the frequency of the exciting field pulse as compared to the gyration frequency of the vortex core, the amplitude and nature of the exciting pulse, the distance between the vortices and their relative polarity. Until recently,[155] the energy transfer efficiency was found to be well below 100%[160,161] and no amplification has been reported thus far. It has also been reported that the interaction

strength between coupled vortices is maximum when their core polarities are opposite,[155] although, higher interaction strength is not the sufficient condition for higher transfer efficiency. For higher amplitude input, the vortex motion enters the non–linear regime and vortex core switching occurs; making it impossible to increase and maintain a large amplitude output and a constant phase relation between gyrotropic motion of both the vortices. On the other hand, if the input signal is very weak and the frequency is close to the gyration frequency of the vortex core, the amplitude of the response gradually increases indicating that the core switching may occur at some point, which is not desirable for device application.

In Chap. 2, we introduce the background theory on which the new contributions presented in this thesis are based. Some state of the art prior to this work has also been presented here. In Chap. 3, we introduce parts of the scientific method employed during this work. Basics of the numerical methods have been presented in Chap. 4. Here we show how to obtain the SW spectra in different kinds of nanoscale magnetic systems. In Chap. 5, we study the effect free or pinned boundary conditions may have on the SW dispersion relation of a magnonic antidot waveguide (MAW) — a magnetic waveguide like structure with a row of holes (or antidots) milled along their central axis. We noticed that bandgaps can be opened in the same system if pinned boundary conditions are used without changing any material or geometrical parameters. From Chaps. 6 to 8, we consider the effects of different geometrical parameters of a MAW over its characteristic SW dispersion. Among other things, we also establish that bandgaps which collapse due to a loss of physical mirror symmetry can be recovered by using an asymmetric bias field. We extend the numerical methods to analyse the SW dispersion in 2D MCs in Chap. 9. In Chap. 10, another enhancement of the numerical method is introduced which nullifies the aliasing associated with the Fourier transforms of real valued data. As a result, we could confirm the existence of bandgaps in submillimetre frequency band in the case of a MAW. The dependence of SW spectra on lattice and bias field has been experimentally examined in Chap. 11. Polarity dependent asymmetric gain in the gyrotropic modes of magnetostatically coupled magnetic vortices has been presented in Chap. 12. Based on this observation, we also demonstrate how the operational states of a conventional transistor may be obtained using a chain of magnetic vortices. We summarize the observation made during this work in Chap. 13.

2. Theoretical Background

2.1. Ferromagnetism

A material placed within a *magnetic field* **H**, may develop a non–zero magnetic moment. Magnetic moment per unit volume is termed as *magnetization* and is conventionally represented by the symbol **M**. *Magnetic susceptibility* χ is defined as the ratio of magnetization **M** to the magnetic field **H**:

$$\mathbf{M} \equiv \chi \mathbf{H}. \tag{2.1}$$

The dependence of magnetic susceptibility χ, on field **H** determines the *magnetic ordering* of the material. On the basis of this criteria a material can be classified as diamagnetic, paramagnetic, ferromagnetic, antiferromagnetic or ferrimagnetic. *Langevin's classical theory of diamagnetism* uses the electron's orbital angular momentum to adequately explain why the diamagnetic susceptibility χ_d (typically of the order of 10^{-6} cm^3/mol), is always negative and independent of changes to temperature or magnetic field **H**. If the material has N atoms per unit volume and each atom contains Z electrons, then the diamagnetic susceptibility χ_d is given as

$$\chi_d = -\frac{Ne^2}{6mc^2} \sum_{i=1}^{Z} \left\langle r^2 \right\rangle r_i. \tag{2.2}$$

Here, m is the mass of an electron and c is the speed of light.

Curie's law for paramagnetism uses a quantum mechanical model to explain why the susceptibility in a paramagnetic material χ_p, is independent of the magnetic field and varies inversely with temperature T. If g represents the Landé g–factor, the paramagnetic susceptibility is given as

$$\chi_p = \frac{C}{T}, \tag{2.3}$$

where

$$C = \frac{Ng^2 J(J+1)\mu_{\mathrm{B}}^2}{3k_{\mathrm{B}}}. \tag{2.4}$$

The ferromagnetic susceptibility χ_f is similarly given by the following *Curie–Weiss law*:

$$\chi_f = \frac{C}{T - WC} = \frac{C}{T - T_c}, \tag{2.5}$$

where $T_c = WC$ is called the *Curie temperature* below which, all ferromagnetic materials demonstrate spontaneous magnetization. In order to derive the Curie–Weiss law (Eq. (2.5)), Weiss assumed an average molecular field of the form $\mathbf{H} + W\mathbf{M}$, where W is known as the *Weiss constant*. The Heisenberg theory establishes that this molecular field comes from the quantum mechanical *exchange interaction*. Pauli's exclusion principle dictates that the two electronic wavefunctions of a hydrogen molecule must combine antisymmetrically. Using separation of variables, the wavefunction $\psi(r_i, s_i)$ of an electron can be expanded as

$$\psi(r_i, s_i) = \rho(r_i)\,\sigma(s_i), \tag{2.6}$$

where ρ and σ are functions of electron's position r_i and spin s_i, respectively. Now, the antisymmetric wavefunctions can be expressed as either

$$\psi_S = \rho_{sym}(r_1, r_2)\,\sigma_{anti}(s_1, s_2), \text{ or} \tag{2.7}$$

$$\psi_T = \rho_{anti}(r_1, r_2)\,\sigma_{sym}(s_1, s_2). \tag{2.8}$$

Here, ψ_S and ψ_T represent the *singlet* and the *triplet* states, respectively. They can be expanded as

$$\psi_S = A\left[\rho_a(r_1)\,\rho_b(r_2) + \rho_a(r_2)\,\rho_b(r_1)\right]\left[\sigma_\alpha(s_1)\,\sigma_\beta(s_2) - \sigma_\alpha(s_2)\,\sigma_\beta(s_1)\right], \text{ and} \tag{2.9}$$

$$\psi_T = B\left[\rho_a(r_1)\,\rho_b(r_2) - \rho_a(r_2)\,\rho_b(r_1)\right]\begin{bmatrix} \sigma_\alpha(s_1)\,\sigma_\alpha(s_2) \\ \sigma_\alpha(s_1)\,\sigma_\beta(s_2) + \sigma_\alpha(s_2)\,\sigma_\beta(s_1) \\ \sigma_\beta(s_1)\,\sigma_\beta(s_1) \end{bmatrix}. \tag{2.10}$$

Spins are antiparallel in the singlet state with a total spin quantum number $S = 0$. How-

ever, in the triplet state, the total spin quantum number $S = 1$ allows for a degeneracy of $(2S + 1) = 3$ states. The energies for singlet (E_S) and triplet (E_T) states can be written as

$$E_S = A^2 (K_{12} + J_{12}), \text{ and} \tag{2.11}$$

$$E_T = B^2 (K_{12} - J_{12}). \tag{2.12}$$

Here, K_{12} and J_{12} denote the Coulomb interaction and *exchange integral*, respectively. They can be expressed by the following two integrals:

$$K_{12} = \int \rho_a^* (r_1) \rho_b^* (r_2) \mathcal{H}_{12} \rho_a (r_1) \rho_b (r_2) d\tau_1 d\tau_2, \text{ and} \tag{2.13}$$

$$J_{12} = \int \rho_a^* (r_1) \rho_b^* (r_2) \mathcal{H}_{12} \rho_a (r_2) \rho_b (r_1) d\tau_1 d\tau_2. \tag{2.14}$$

Here $\mathcal{H}_{12} = e^2/r_{ab} + e^2/r_{12} - e^2/r_{1b} - e^2/r_{a2} : r_{ij} = |r_i - r_j|$, is the Hamiltonian for electrons 1 and 2 in a hydrogen molecule with nuclei a and b.

A positive J_{12} favours the triplet state – and the parallel arrangement of spins – as E_T decreases. This is the case with ferromagnets, where the interatomic spacing r_{ab} is larger as compared to the radii of the d and f electronic orbitals. J_{12} becomes negative in *antiferromagnetic* materials leading to an antiparallel arrangement of neighbouring spins. This results in a zero net magnetism. In the case of *ferrimagnets* the antiparallel magnetic moments do not have the same magnitude. This is due to the presence of two sublattices hosting two types of ions with differing magnetic moments. This bestows ferrimagnets with some net magnetization at low temperatures. Analogous to the Curie temperature for ferromagnets, there exists a *Néel temperature* for antiferromagnets and ferrimagnets above which the thermal energy overcomes the energy of the magnetic ordering and a paramagnetic behaviour unfolds.

In this work, we deal with ferromagnetic materials like permalloy (Py: $Ni_{80}Fe_{20}$) and cobalt (Co) only (the description of the hydrogen molecule has been used for the sake of simplicity). Hence, the term 'magnetic material' is used interchangeably with 'ferromagnetic material'.

2.2. Magnetic Energies

Different components of the effective field $\mathbf{H}_{\text{eff}}$, is the vector sum of the external field, the demagnetizing field and the magnetocrystalline anisotropy field. Each of these components of the effective field $\mathbf{H}_{\text{eff}}$, contribute to the total magnetic energy E_{tot} of the system:

$$E_{\text{tot}} = E_Z + E_e + E_d + E_K, \tag{2.15}$$

where E_Z, E_e, E_d and E_K are the Zeeman energy, the exchange energy, the magnetostatic self–energy and the magnetocrystalline anisotropy energy, respectively. These different energy terms and their dependence on magnetization $\mathbf{M}$ are discussed in the following subsections. Other magnetic energies, such as magnetostriction can be considered in Eq. (2.15) as well. However, they are outside the scope of this work.

2.2.1. Zeeman Energy

Zeeman energy E_Z, is the energy which originates from the interaction of external magnetic field $\mathbf{H}_{\text{ext}}$ (which itself can be described as the sum of the bias magnetic field $\mathbf{H}_{\text{bias}}$ and any applied signal $\mathbf{H}_{\text{sig}}$), with magnetization $\mathbf{M}$. It can be expressed as follows:

$$E_Z = -\mu_0 \int \mathbf{M} \cdot \mathbf{H}_{\text{ext}} dV. \tag{2.16}$$

Here, V is the volume of the magnetic material. The external field is generally specified explicitly. The Zeeman energy is minimized when magnetization is parallel to the external field.

2.2.2. Exchange Energy

Exchange energy is the main cause of ferromagnetism (see Sec. 2.1). Assuming an isotropic exchange interaction, the Heisenberg Hamiltonian for exchange energy E_e can be evaluated as[164]

$$E_e = -2 \sum_{ij} \left(J_e \mathbf{S}_i \cdot \mathbf{S}_j \right), \tag{2.17}$$

where J_e is the isotropic exchange integral and $\mathbf{S}_i$ and $\mathbf{S}_j$ are total spins at neighbouring sites i and j. We can replace the summation with an integral to rewrite Eq. (2.17) for a continuous geometry as

$$E_e = A \int (\nabla \mathbf{m})^2 \, dV, \tag{2.18}$$

where $\mathbf{m} = \mathbf{M}/M_\mathrm{s}$ is the ratio of magnetization to the saturation magnetization, $(\nabla \mathbf{m})^2$ is a shorthand for $(\nabla m_x)^2 + (\nabla m_y)^2 + (\nabla m_z)^2$. A is the *exchange coefficient* given by

$$A = A_{ij} = \frac{2 J_e S^2}{\Delta_{ij}}, \tag{2.19}$$

where Δ_{ij} is separation between neighbouring sites i and j. Isotropy is assumed with $A = A_{ij}$. For ferromagnets such as nickel, permalloy ($Ni_{80}Fe_{20}$), iron and cobalt, the typical values of the exchange coefficient are[6] 9×10^{-12} J/m, 13×10^{-12} J/m, 21×10^{-12} J/m and 30×10^{-12} J/m, respectively.

2.2.3. Magnetostatic Self–Energy

The Maxwell's equations for a ferromagnet can be written as[6]

$$\nabla \times \mathbf{H}_\mathrm{dem} = 0, \text{ and} \tag{2.20}$$

$$\nabla \cdot \mathbf{B} = 0. \tag{2.21}$$

Here, $\mathbf{H}_\mathrm{dem}$ is the demagnetizing field. Using $\mathbf{B} = \mu_0 (\mathbf{H}_\mathrm{dem} + \mathbf{M})$ and the fact that curl of a gradient is zero, we can now deduce

$$\mathbf{H}_\mathrm{dem} = -\nabla U_\mathrm{dem}, \text{ and} \tag{2.22}$$

$$\nabla \cdot \mathbf{H}_\mathrm{dem} = -\nabla \cdot \mathbf{M}. \tag{2.23}$$

Thus, we arrive at

$$\nabla^2 U_\mathrm{dem} = \nabla \cdot \mathbf{M}. \tag{2.24}$$

Here, U_dem is a scalar potential corresponding to the demagnetizing field $\mathbf{H}_\mathrm{dem}$.

The component of $\mathbf{H}_\mathrm{dem}$ parallel to the ferromagnet's surface S needs to be continuous

near S. Similar constraint is obeyed by the component of $\mathbf{B}$ which is normal to the surface S. Apart from these boundary conditions, far away from the ferromagnet, we also have $U_{\text{dem}} \to 0$. Equation (2.24) can be solved analytically with these boundary conditions to obtain[165,166]

$$U_{\text{dem}}(\mathbf{r}) = \frac{1}{4\pi}\left(-\int_{V'} \frac{\nabla' \cdot \mathbf{M}(\mathbf{r}')}{|\mathbf{r}-\mathbf{r}'|} dV' + \oint_{S'} \frac{\hat{\mathbf{n}} \cdot \mathbf{M}(\mathbf{r}')}{|\mathbf{r}-\mathbf{r}'|} dS'\right), \tag{2.25}$$

where V' represents the volume of the ferromagnet bounded by surface S'. Thus, from Eqs. 2.22 and 2.25, we get

$$\mathbf{H}_{\text{dem}}(\mathbf{r}) = \frac{1}{4\pi}\left(-\int_{V'} \frac{(\mathbf{r}-\mathbf{r}')\,\nabla' \cdot \mathbf{M}(\mathbf{r}')}{|\mathbf{r}-\mathbf{r}'|^3} dV' + \oint_{S'} \frac{(\mathbf{r}-\mathbf{r}')\,\hat{\mathbf{n}} \cdot \mathbf{M}(\mathbf{r}')}{|\mathbf{r}-\mathbf{r}'|^3} dS'\right). \tag{2.26}$$

Knowing $\mathbf{H}_{\text{dem}}$ from Eq. (2.26), the magnetostatic self–energy E_d can now be calculated as

$$E_d = -\frac{\mu_0}{2}\int_V (\mathbf{H}_{\text{dem}} \cdot \mathbf{M})\, dV. \tag{2.27}$$

2.2.4. Magnetocrystalline Anisotropy Energy

Spin–orbit coupling in a crystal structure can force the electronic spins to favour some crystallographic directions more than others. Thus, depending upon the crystal structure of a ferromagnet, certain directions may be preferred by the magnetization vector $\mathbf{M}$. The magnetocrystalline anisotropy energy is minimum if $\mathbf{M}$ points along these crystallographic axes. They are defined as *easy axes*. *Hard axis* is the crystallographic direction along which, it is very difficult for the magnetization vector to align itself as doing so would result in a high magnetocrystalline anisotropy energy E_K. It is conventional to express such *uniaxial anisotropy* as a polynomial of sines of the angle θ made by magnetization $\mathbf{M}$ with the easy axis:[164]

$$E_K = K_1 \sin^2\theta + K_2 \sin^4\theta, \tag{2.28}$$

where, the *anisotropy constants* K_1 and K_2 (typically $K_1 \gg K_2$) change with temperature. If $K_1 < 0$, the easy axis lies in plane — known as the *easy plane* — perpendicular to a predefined crystallographic direction.

Similar to the uniaxial anisotropy, the *cubic anisotropy* can be expressed in terms of

Table 2.1.: Magnetocrystalline anisotropy for some common ferromagnets. Source: Ref. 6.

Metal	**Crystal Structure**	**Easy axis**	**Hard axis**	K_1 or K_1' ($\mathrm{J/m^3}$)	K_2 or K_2' ($\mathrm{J/m^3}$)
Py	*fcc*	—	—	—	—
Ni	*fcc*	[111]	[110], [100]	-5.0×10^3	—
Fe	*bcc*	[100], [110]	[111]	4.6×10^4	1.5×10^4
Co	*hcp*	**c** *	**a**, **b** *	4.1×10^5	1×10^5

cosines α_1, α_2 and α_3 of the angular direction of magnetization w.r.t. the edges of the cubic crystal:[164]

$$E_K = K_1' \left(\alpha_1^2\alpha_2^2 + \alpha_2^2\alpha_3^2 + \alpha_3^2\alpha_1^2\right) + K_2'\alpha_1^2\alpha_2^2\alpha_3^2. \tag{2.29}$$

Ni and Fe exhibit cubic anisotropy, while (*hcp*) Co features uniaxial anisotropy. Py does not have a significant magnetocrystalline anisotropy. Thus, it is ideally suited for cases where one wishes to examine the magnetization dynamics without considering the effects of magnetocrystalline anisotropy. The values of K_1 (or K_1') and K_2 (or K_2') for some common ferromagnets are presented in Tab. 2.1.

2.3. Magnetization Dynamics

2.3.1. Brown's Equations

Let us recall the Eq. (2.15):

$$E_{\mathrm{tot}} = E_Z + E_e + E_d + E_K.$$

Assuming uniaxial anisotropy, we can now substitute the terms on the right hand side of the above equation by using Eqs. (2.16), (2.18), (2.27) and (2.28) to obtain:

$$E_{\mathrm{tot}} = \int_V \left(-\mu_0 \mathbf{M}\cdot\mathbf{H}_{\mathrm{ext}} + A\left(\nabla\mathbf{m}\right)^2 - \frac{\mu_0}{2}\mathbf{M}\cdot\mathbf{H}_{\mathrm{dem}} + K_1\sin^2\theta\right) dV. \tag{2.30}$$

*$\mathbf{a}$, $\mathbf{b}$ and $\mathbf{c}$ are the basis vectors of the *hcp* lattice.

The value of total energy E_{tot}, near its minima should not change with minor variations in the magnetization:

$$\frac{\delta E_{\text{tot}}}{\delta \mathbf{M}} = 0. \tag{2.31}$$

With that assumption we get the following *Brown's equations*:[167]

$$\mathbf{m} \times \left(2A\nabla^2\mathbf{m} + \mu_0 M_{\text{s}} \left(\mathbf{H}_{\text{ext}} + \mathbf{H}_{\text{dem}}\right) + 2K_1 \cos\theta \hat{\mathbf{c}}\right) = 0, \text{ or} \tag{2.32}$$

$$\mathbf{M} \times \left(\lambda_{\text{ex}}^2 \nabla^2 \mathbf{m} + \mathbf{H}_{\text{ext}} + \mathbf{H}_{\text{dem}} + \frac{2K_1}{\mu_0 M_{\text{s}}} \cos\theta \hat{\mathbf{c}}\right) = 0. \tag{2.33}$$

Here, $\hat{\mathbf{c}}$ is the unit vector along the easy axis and λ_{ex}^2 is the ratio of the exchange coefficient A to the stray field energy constant $\mu_0 M_{\text{s}}^2/2$. λ_{ex} is called the *exchange length* below which the exchange field is believed to play a greater role in magnetization dynamics when compared to the demagnetizing field.

As the cross product of magnetization with another term in Eq. (2.33) is zero, both of them must be collinear. So we define the effective field as:

$$\mathbf{H}_{\text{eff}} = \overbrace{\lambda_{\text{ex}}^2 \nabla^2 \mathbf{m}}^{\mathbf{H}_{\text{exch}}} + \mathbf{H}_{\text{ext}} + \mathbf{H}_{\text{dem}} + \overbrace{\frac{2K_1}{\mu_0 M_{\text{s}}} \cos\theta \hat{\mathbf{c}}}^{\mathbf{H}_{\text{anis}}}. \tag{2.34}$$

Here $\mathbf{H}_{\text{exch}}$ and $\mathbf{H}_{\text{anis}}$ are the exchange and anisotropy fields, respectively.

If the torque $\mathbf{M} \times \mathbf{H}_{\text{eff}}$ is not zero then magnetization $\mathbf{M}$ will keeps precessing about the effective field $\mathbf{H}_{\text{eff}}$ until the dynamics gets damped out. The same is discussed in the next sub–section.

2.3.2. Landau–Lifshitz–Gilbert Equations

The Hamiltonian $\mathcal{H}$ for a spin observable $\mathbf{S}$ in the presence of a magnetic flux density $\mathbf{B}$ is given by

$$\mathcal{H} = -g\mu_{\text{B}} \mathbf{S} \cdot \mathbf{B}/\hbar, \tag{2.35}$$

where μ_{B} is the Bohr magneton and $\hbar$ is the reduced Plank constant. The time rate of change the spin observable $\mathbf{S}$, can be expressed in terms of its commutation with the Hamiltonian

as:[6]

$$i\hbar \frac{d}{dt} \langle \mathbf{S} \rangle = [\mathbf{S}, \mathcal{H}] \,. \tag{2.36}$$

As per the commutation rule between different components of the spin operator, we have

$$[S_x, S_y] = i\hbar \epsilon_{xyz} S_z. \tag{2.37}$$

From Eqs. (2.35), (2.36) and (2.37), we get

$$\frac{d}{dt} \langle \mathbf{S} \rangle = \frac{g\mu_{\mathrm{B}}}{\hbar} \mathbf{S} \times \mathbf{B}. \tag{2.38}$$

Using Eq. (2.38), Landau & Lifshitz[7] suggested:

$$\frac{d\mathbf{M}}{dt} = -\left|\gamma\right| \mathbf{M} \times \mathbf{H}_{\mathrm{eff}}, \tag{2.39}$$

where $|\gamma|$ is known as the *gyromagnetic ratio* and the local effective field $\mathbf{H}_{\mathrm{eff}}$ is defined by Eq. (2.34). Equation (2.39) is known as the *Landau–Lifshitz equation*. It describes the precession of magnetization $\mathbf{M}$ in the presence of an effective field $\mathbf{H}_{\mathrm{eff}}$.

This precession is gradually damped by dissipative processes such as spin–orbit coupling, spin diffusion, magnon–phonon interaction or misalignment of atomic spins.[16] Gilbert modified Eq. (2.39) to account for this damping by introducing a phenomenological damping term:

$$\frac{d\mathbf{M}}{dt} = -\left|\gamma\right| \mathbf{M} \times \mathbf{H}_{\mathrm{eff}} + \frac{\alpha}{M_{\mathrm{s}}} \mathbf{M} \times \frac{d\mathbf{M}}{dt}. \tag{2.40}$$

Here, the Gilbert damping constant $\alpha > 0$ needs to be determined by careful experimentation. For transition metals $\alpha \ll 1$. Its respective values for nickel, iron, cobalt and permalloy ($Ni_{80}Fe_{20}$) are 0.064, 0.0019, 0.011 and 0.008.[168–170] Equation (2.40) is known as the *Gilbert*

equation. Upon replacing $d\mathbf{M}/dt$ on the right–hand–side of Eq. (2.40) with itself, we get

$$\begin{aligned}
\frac{d\mathbf{M}}{dt} &= -|\gamma|\,\mathbf{M}\times\mathbf{H}_{\text{eff}} + \frac{\alpha}{M_{\text{s}}}\mathbf{M}\times\left(-|\gamma|\,\mathbf{M}\times\mathbf{H}_{\text{eff}} + \frac{\alpha}{M_{\text{s}}}\mathbf{M}\times\frac{d\mathbf{M}}{dt}\right) \\
&= -|\gamma|\,\mathbf{M}\times\mathbf{H}_{\text{eff}} - \frac{\alpha\,|\gamma|}{M_{\text{s}}}\mathbf{M}\times(\mathbf{M}\times\mathbf{H}_{\text{eff}}) - \alpha^2\frac{d\mathbf{M}}{dt} \\
\implies \left(1+\alpha^2\right)\frac{d\mathbf{M}}{dt} &= -|\gamma|\,\mathbf{M}\times\mathbf{H}_{\text{eff}} - \frac{\alpha\,|\gamma|}{M_{\text{s}}}\mathbf{M}\times(\mathbf{M}\times\mathbf{H}_{\text{eff}}) \\
\implies \frac{d\mathbf{M}}{dt} &= -|\bar{\gamma}|\,\mathbf{M}\times\mathbf{H}_{\text{eff}} - \frac{\alpha\,|\bar{\gamma}|}{M_{\text{s}}}\mathbf{M}\times(\mathbf{M}\times\mathbf{H}_{\text{eff}}) \qquad (2.41)
\end{aligned}$$

Equation (2.41) is known as the *Landau–Lifshitz–Gilbert* (LLG) *equation* and is equivalent to the Gilbert equation under the relation $|\gamma| = (1+\alpha^2)\,|\bar{\gamma}|$. $|\gamma|$ and $|\bar{\gamma}|$ are known as Gilbert and Landau–Lifshitz gyromagnetic ratios, respectively. Since, $\alpha \ll 1$ in most cases considered here, we can sometimes assume $|\gamma| \approx |\bar{\gamma}|$. In most cases, an analytical solution is not possible and a numerical approach is adopted by using micromagnetic solvers (see Tab. 3.1). As the time derivative appears on only one side of the LLG Eq. (2.41), it is preferred over the Gilbert Eq. (2.40).[171]

2.3.3. Ferromagnetic Resonance and The Kittel Formula

As per the LLG Eq. (2.41), the frequency ω with which the magnetization vector $\mathbf{M}$ (of a continuous ferromagnet) precesses around the effective field $\mathbf{H}_{\text{eff}}$ can be approximated by $\omega \approx |\bar{\gamma}|\,H_{\text{eff}}$. If a small signal $\mathbf{H}_{\text{sig}}$, varying with the same frequency ω, is applied orthogonally to the external bias field then a resonance occurs and the magnetization dynamics starts to draw power from the signal. This is known as the *ferromagnetic resonance*.

In the absence of any external field, Eq. (2.23) could have been used to determine $\mathbf{H}_{\text{dem}}$ for a uniformly magnetized ferromagnet of infinite size. The macrospin model deals with uniformly magnetized ferromagnets. Magnetization tends to align itself parallel to the surfaces of ferromagnetic body. The effects of this shape anisotropy is significantly pronounced in the case of nanoscale systems such as thin films or nanowires. This is also why the experimentally reported precession frequencies[172] were two to four times higher than that predicted by the macrospin model.[173]

Consider a uniformly magnetized ferromagnetic slab depicted in Fig. 2.1 (a) with a face

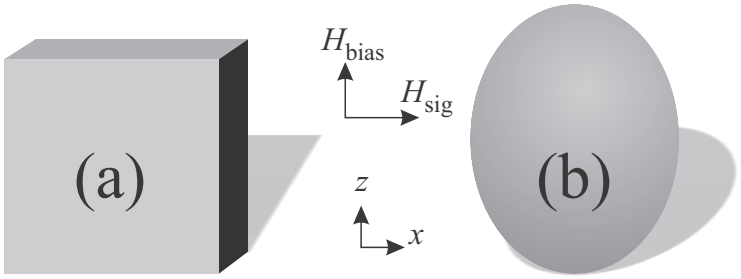

Figure 2.1.: Uniformly magnetized ferromagnetic (a) slab and (b) ellipsoid.

at $y = 0$. Let the applied external field $\mathbf{H}_{\text{ext}}$ be given by

$$\mathbf{H}_{\text{ext}} = (H_{\text{sig}}, 0, H_{\text{bias}}), \tag{2.42}$$

where H_{sig} is the microwave frequency signal and H_{bias} is the external bias field. Exploiting the continuity of the normal component B_y of magnetic flux density $\mathbf{B}$, one can write $H_y = -M_y$. Thus, the effective field $\mathbf{H}_{\text{eff}}$ of $(H_{\text{sig}}, -M_z, H_{\text{bias}})$ should be used for calculation of the resonant frequency with the LLG Eq. (2.41). The exchange field does not affect the ferromagnetic resonance frequency.[173] Ignoring the damping in Eq. (2.41), we get:

$$\begin{aligned}
\frac{dM_x}{dt} &= -|\bar{\gamma}|\,(M_y H_z - H_y M_z) \\
&= -|\bar{\gamma}|\,(M_z + H_z)\,M_y \\
&= -|\bar{\gamma}|\,B_z M_y/\mu_0, && (2.43) \\
\frac{dM_y}{dt} &= -|\bar{\gamma}|\,(M_z H_x - H_z M_x) \\
&= |\bar{\gamma}|\,M_x H_{\text{bias}}, \text{ and} && (2.44) \\
\frac{dM_z}{dt} &\approx 0. && (2.45)
\end{aligned}$$

Equation (2.44) is obtained with the assumption that the signal amplitude is sufficiently small. From Eqs. (2.43) and (2.44), we can now write

$$\frac{d^2 M_x}{dt^2} = -|\bar{\gamma}|^2\,B_z H_{\text{bias}} M_x/\mu_0. \tag{2.46}$$

Solving the above equation, we get the ferromagnetic resonant frequency of

$$\omega = |\bar{\gamma}| \sqrt{B_z H_{\text{bias}}/\mu_0}, \tag{2.47}$$

which agrees well with the experimentally observed value. Thus, it is important to consider the effect of demagnetization while interpreting any results involving ferromagnetic resonance at the nanoscale.

The demagnetizing field $\mathbf{H}_{\text{dem}}$, can be expressed using an inner product of magnetization $\mathbf{M}$ with the *demagnetizing tensor* $\overleftrightarrow{\mathbf{N}}$:[174]

$$\mathbf{H}_{\text{dem}} = -\overleftrightarrow{\mathbf{N}} \cdot \mathbf{M}. \tag{2.48}$$

Here $\overleftrightarrow{\mathbf{N}}$ is a second rank symmetric tensor with unit trace:[166]

$$\overleftrightarrow{\mathbf{N}} = \begin{bmatrix} N_{xx} & N_{xy} & N_{xz} \\ N_{xy} & N_{yy} & N_{yz} \\ N_{xz} & N_{yz} & N_{zz} \end{bmatrix} \; : \; N_{xx} + N_{yy} + N_{zz} = 1. \tag{2.49}$$

Equation (2.49) can be used to obtain the ω at which the ferromagnetic resonance (of a uniformly magnetized body with uniform demagnetization) will occur:[27]

$$\omega = \left\{ \left(\omega_H + |\bar{\gamma}| \, N_{xx} M_{\text{s}}\right) \left(\omega_H + |\bar{\gamma}| \, N_{yy} M_{\text{s}}\right) - |\bar{\gamma}|^2 \, N_{xy}^2 M_{\text{s}}^2 \right\}^{1/2}, \tag{2.50}$$

where we assume $M_z \approx M_{\text{s}}$ and

$$\omega_H = |\bar{\gamma}| \left(H_{\text{bias}} - N_{zz} M_{\text{s}}\right). \tag{2.51}$$

Equation (2.50) can be used when z–axis points in the direction of bias magnetic field. If needed, an analogous tensor $\overleftrightarrow{\mathbf{N}}_{\text{anis}}$, which can be defined for magnetocrystalline anisotropy field should also be used along with the demagnetizing tensor $\overleftrightarrow{\mathbf{N}}$.

As shown in Fig. 2.1 (b), if the principal axes of an ellipsoidal ferromagnet are aligned with the coordinate axes, only the diagonal components of tensor $\overleftrightarrow{\mathbf{N}}$ remain non–zero. This

gives a resonant frequency for a generic ellipsoidal ferromagnet as

$$\omega = |\bar{\gamma}| \sqrt{(H_{\text{bias}} + (N_{xx} - N_{zz})\, M_{\text{s}})\,(H_{\text{bias}} + (N_{yy} - N_{zz})\, M_{\text{s}})}. \tag{2.52}$$

Equation (2.52) is known as the *Kittel formula.*[173]

2.3.4. Laser Pulse Induced Ultrafast Demagnetization

One type of magnetization dynamics that is not completely described by the LLG equation is an ultrafast demagnetization process which can be triggered by a femtosecond laser pulse.[175] As seen in Fig. 1.1, this happens within a picosecond. But, how is the magnetization quenched so quickly while conserving the net angular momentum[176]? Photons from the laser pulse interact with the spin degrees of freedom of electrons while non–linearly modifying their own angular momentum. *Hot electrons*, with temperature up to 10^3 K,[177] are then created due to electron–electron scattering.[178] This is followed by electron–magnon interaction mediated thermalization of spin population.[179,180] This causes the loss of phase memory of electronic wavefunctions w.r.t. the excitation, eventually leading to the ultrafast demagnetization. The exact mechanism of this process is the subject of hot debate,[181–184] but most scientists believe that a phonon mediated spin–flip scattering plays an important role.[113,176,178,185–187]

Some time after the ultrafast demagnetization, the spins begin to relax in two time scales. The faster relaxation time scale of a few picoseconds is the result of electrons and spins exchanging energy with the lattice by the electron–phonon interaction. A *three temperature model*[175,188] involving electrons, spins and phonons has been proposed to describe this process. As the magnetocrystalline anisotropy field changed with rapidly changing temperature of phonons, it works as a trigger to initialize the precession of magnetization around the local effective field. The longer relaxation time scale of hundreds of picoseconds results due to the diffusion of electron and lattice heat.[189,190] Relaxation dynamics in both these time scales can be modelled by the LLG equation.

2.4. Magnonics

Like other physical waves, SWs exhibit phenomena like resonance,[172,173] reflection and refraction,[191–196] dispersion,[197] interference and diffraction,[80,198–201] tunnelling,[202,203] Doppler effect[204–206] and formation of envelop solitons.[207–209] Magnons, the quanta of SWs, have been identified as bosons.[2,30] Bose–Einstein condensation of magnons has also been observed in different magnetic systems.[31,32,210] Magnonics is the study of various aspects of SWs — both classical and quantum mechanical.[38,69,70] In the following sub–sections, we first introduce the theory of SW dynamics in terms of its dispersion relation in different kinds of nanoscale magnetic systems, then we discuss how magnonics as field of study has been developed so far.

2.4.1. Exchange Dominated SWs in Thin Films

SWs are called exchange dominated if their wavenumber $k \gg 1/\lambda_{\text{ex}}$. It has been demonstrated that the spectrum of exchange dominated SWs can be tuned by controlling the exchange field.[68] SW dispersion relation $\omega(k)$ for a 1D chain of ferromagnetic sites of spin S and distance a apart has been calculated as[211]

$$\omega = 4JS\left(1 - \cos ka\right)/\hbar, \tag{2.53}$$

where k is the SW wavevector. In the long wavelength limit ($ka \ll 1$), Eq. (2.53) reduces to

$$\omega = \left(2JSa^2/\hbar\right)k^2. \tag{2.54}$$

As the presence of boundaries or surfaces in a magnetic medium alters the exchange field in their immediate neighbourhood, the dispersion relation of exchange dominated SWs is generally regarded to be isotropic within a bulk magnetic medium. In the case of thin films, SWs obey the following dispersion relation[212]

$$f(k) - f(0) = |\bar{\gamma}| M_{\text{s}} \lambda_{\text{ex}}^2 k^2. \tag{2.55}$$

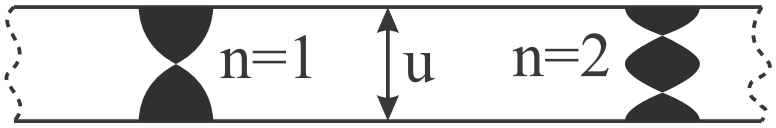

Figure 2.2.: Profile of perpendicular standing SW mode with $n = 1$ and 2 nodes in a thin film with antinodes at the surfaces.

Exchange dominated SWs, which propagate normal to the surface of a thin film, form a standing wave with quantized wavenumber $k = \pi n/u$, where n is the number of nodes in the mode profile and u is the thickness of the thin film. These are known as *perpendicular standing SWs*. A mode profile with one and two nodes is sketched in Fig. 2.2 such that the magnetization dynamics at surface is completely unpinned.[213]

2.4.2. Dipole Dominated SWs in Thin Films

The behaviour of SWs becomes *dipole dominated* if their wavenumber $k \ll 1/\lambda_{\text{ex}}$. It means that the band structure of a dipole dominated SW can be controlled by manipulating the demagnetizing field. Dipole dominated SWs are also known as *magnetostatic waves*. Unlike the exchange dominate SWs, the dispersion relation of magnetostatic waves depends heavily upon the relative orientation of the film, the effective magnetic field $\mathbf{H}_{\text{eff}}$ and the SW wavevector $\mathbf{k}$. The orientation of $\mathbf{H}_{\text{eff}}$ can change during SW dynamics. In the context of this sub–section we consider only the orientation that $\mathbf{H}_{\text{eff}}$ had during the steady state ($d\mathbf{M}/dt = 0$).

When $\mathbf{H}_{\text{eff}}$ (and magnetization) is normal to the surface of the thin film and the SW's propagation direction is in the plane of the film ($\mathbf{k} \perp \mathbf{H}_{\text{bias}}$), the spin wave (SW) mode is called *forward volume* (FV) *magnetostatic mode*. If $\mathbf{H}_{\text{eff}}$ is in the plane of the thin film then the conditions $\mathbf{k} \parallel \mathbf{H}_{\text{eff}}$ and $\mathbf{k} \perp \mathbf{H}_{\text{eff}}$ give rise to *backward volume* (BV) and surface — or *Damon–Eshbach* (DE) SWs, respectively. The dispersion relation of SWs in these different configurations is given as[79,214]

$$f^2 = \begin{cases} f_0\left(f_0 + f_{\text{M}}\frac{1-e^{-ku}}{ku}\right) & \text{(BV)}, \\ f_0\left(f_0 + f_{\text{M}}\left(1 - \frac{1-e^{-ku}}{ku}\right)\right) & \text{(FV)}, \\ f_0\left(f_0 + f_{\text{M}}\right) + \frac{f_{\text{M}}^2}{4}\left(1 - e^{-2ku}\right) & \text{(DE)}, \end{cases} \tag{2.56}$$

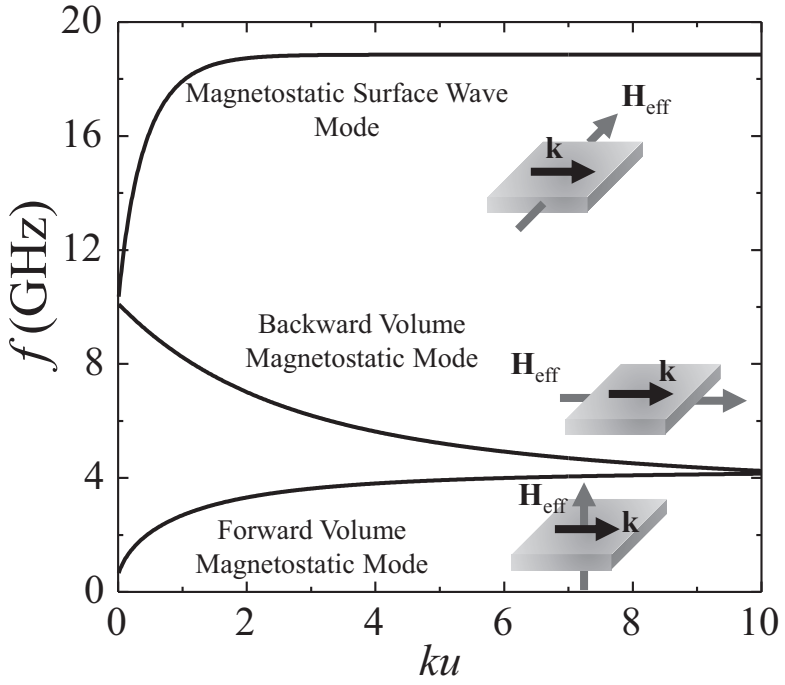

Figure 2.3.: Dispersion relation of magnetostatic SW modes in a film for different relative orientations of wavevector $\mathbf{k}$ and effective field $\mathbf{H}_{\text{eff}}$ in the steady state ($d\mathbf{M}/dt = 0$).

where $f_{\text{M}} = |\bar{\gamma}|\, M_{\text{s}}$ and

$$f_0 = \begin{cases} |\bar{\gamma}|\, H_{\text{bias}} & \text{BV and DE;} \\ |\bar{\gamma}|\, (H_{\text{bias}} - M_{\text{s}}) & \text{FV.} \end{cases} \tag{2.57}$$

The forms of these dispersion relations are shown in Fig. 2.3. For $k \to 0$, Eq. (2.56) converges to describe the Kittel modes of ferromagnetic resonance as presented here in sub–Sec. 2.3.3. BV modes are characterized by anti-parallel phase and group velocities. This character is evident till the angle ϕ between the in-plane $\mathbf{H}_{\text{eff}}$ and SW wavevector $\mathbf{k}$ increases from 0 to a critical value $\phi_{\text{c}} = \tan^{-1}\sqrt{H_{\text{bias}}/M_{\text{s}}}$. Here H_{bias} is the magnitude of the applied bias field. The power of DE modes decay exponentially away from the surface.[6] The associated penetration depth δ, is zero for $\phi = \phi_{\text{c}}$ and increases with increasing ϕ : $\phi_{\text{c}} \leq \phi \leq \pi/2$. Dispersion relation for SWs for a more general relative orientation of wavevector and effective field has been covered by Kalinikos and Slavin.[214]

For $k\lambda_{\text{ex}} \gg 1$, Eq. (2.56) converges to a value independent of k. Thus, if we take only

the dipolar field into account, all SWs will have negligible group velocity for larger values of $k\lambda_{\text{ex}}$. If $k\lambda_{\text{ex}} \approx 1$, the SWs are classified as dipole–exchange SWs. We can obtain the dispersion relation in that case by substituting f_0 with $f_{\text{ex}} = f_0 + k^2\lambda_{\text{ex}}^2 f_{\text{M}}$ in Eq. (2.56).

2.4.3. Effect of Lateral Confinement on SW Band Structure

In this sub–section* we discuss the SW dispersion in laterally confined uniform waveguides while taking both dipolar and exchange fields into consideration and ignoring any magnetocrystalline anisotropy. Rewriting Eq. (2.56) after replacing f_0 with $f_{\text{ex}} = f_0 + k^2\lambda_{\text{ex}}^2 f_{\text{M}}$, we get the relation:

$$f^2 = \begin{cases} f_{\text{ex}}\left(f_{\text{ex}} + f_{\text{M}}\frac{1-e^{-ku}}{ku}\right) & \text{(BV)}, \\ f_{\text{ex}}\left(f_{\text{ex}} + f_{\text{M}}\left(1 - \frac{1-e^{-ku}}{ku}\right)\right) & \text{(FV)}, \\ f_{\text{ex}}\left(f_{\text{ex}} + f_{\text{M}}\right) + \frac{f_{\text{M}}^2}{4}\left(1 - e^{-2ku}\right) & \text{(DE)}. \end{cases} \tag{2.58}$$

Let the two components k_x and k_y of wavevector $\mathbf{k}$ point along length and width of the waveguide, respectively; such that $\mathbf{k}\cdot\mathbf{k} = k^2 = k_x^2 + k_y^2$. Here, a uniform magnetization across the thickness of the waveguide has been assumed.[79] Broken continuous translational symmetry near the edges of the waveguides impose the following quantization along the width w of the waveguide:[215]

$$k_y = (n+1)\,\pi/w_{\text{eff}},\ n = 0, 1, 2, \ldots \tag{2.59}$$

Here,

$$w_{\text{eff}} = \frac{wd}{d-2}, \tag{2.60}$$

$$d = \frac{2\pi}{p\,(1 - 2\ln(p))}, \tag{2.61}$$

$$p = \frac{u}{w} \ll 1. \tag{2.62}$$

Different values of n, which denotes the number of lateral nodal lines in SW mode profile,

*This sub–section are based on Venkat *et al.*[79]

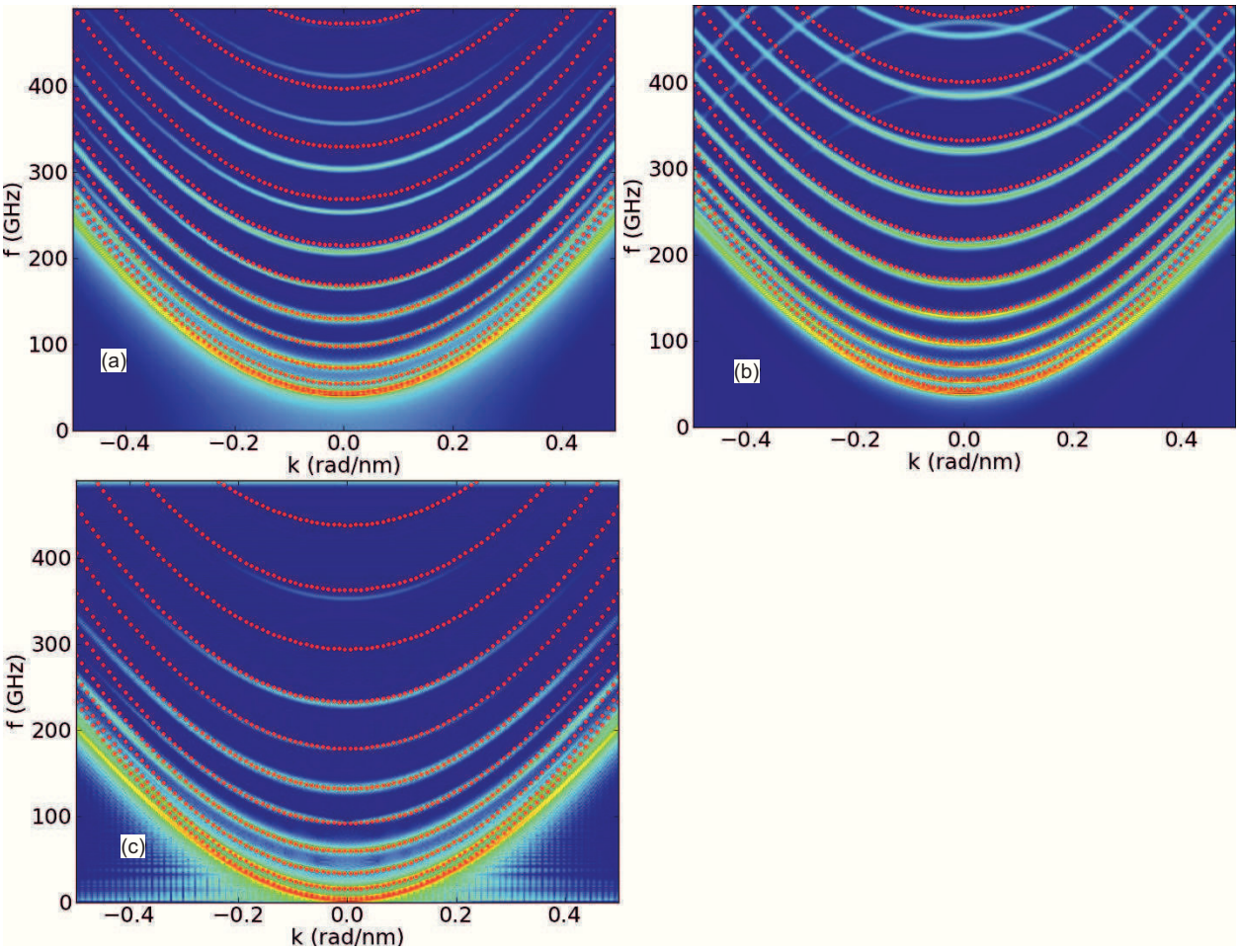

Figure 2.4.: Frequency – wavevector dispersion calculated under a bias field strength $\mu_0 H_{\text{bias}}$ of 1.01 T form numerical (solid lines) and analytical (dotted lines; see Eq. (2.58)) methods for (a) BV, (b) DE and (c) FV configurations. (d) Dimensions of the geometry under considerations with relative orientation of the bias field. Source: Ref. 79.

yield different modes for the same configuration as shown by the dotted lines in Fig. 2.4. SW dispersion relations for BV, DE and FV arrangements in the case of a 50 nm wide and 1 nm thick uniform Py waveguide under a bias field strength $\mu_0 H_{\text{bias}}$ of 1.01 T,[79] are shown is Fig. 2.4 (a), (b) and (c), respectively. It can be noticed that dotted lines calculated using Eq. (2.58) agree well with those calculated using micromagnetic simulations (MSs) for lower values of frequency and wavevector. For larger values of k_x the simulated branches of SW dispersion relation start to bend due to creation of false Brillouin zone boundaries during FDM related discretization of the waveguide.

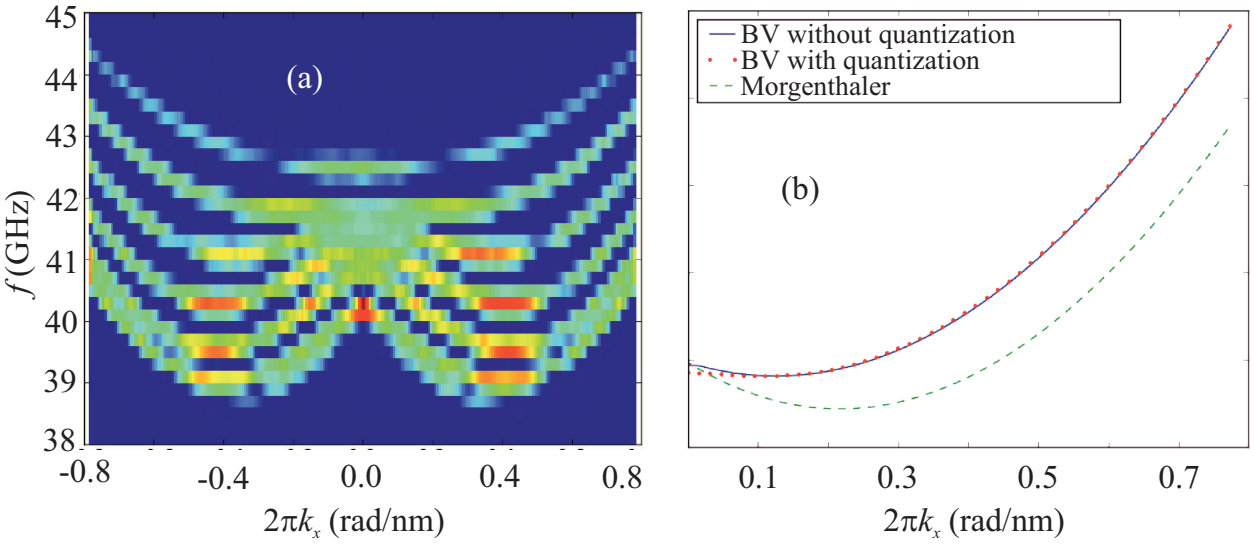

Figure 2.5.: Dispersion relation of SWs of the case presented in Fig. 2.4 (a), recalculated with exchange coefficient $A = 2.515 \times 10^{-13}$ J/m using (a) MSs and (b) analytical models (as noted in the legend). Source: Ref. 79.

For higher order bands, the simulated results underestimate the frequency values. It can also be noted that the opposite sign of phase and group velocity, which is the hallmark of BV configuration is not observed in Fig. 2.4 (a). The effect of exchange field, which gives a parabolic shape to dispersion curves, is too dominant to allow that phenomenon. Thus, the case presented in Fig. 2.4 (a) is recalculated with a reduced exchange coefficient $A = 2.515 \times 10^{-13}$ J/m. The results obtained using MSs are presented in Fig. 2.5 (a). This can be compared to results obtained using the analytical expression for BV configuration as given by Eq. (2.58), with and without the quantization specified by Eq. (2.59). Another model, which assumes comparable exchange and dipole interaction was presented by Morgenthaler[216] as

$$f^2 = f_{\mathrm{ex}} \left(f_{\mathrm{ex}} + f_{\mathrm{M}} \frac{k_y^2 + k_z^2}{k_x^2 + k_y^2 + k_z^2} \right), \tag{2.63}$$

where for the first mode, k_z can be obtained from $k_x = k_z \tan(k_z u)$. As seen from Fig. 2.5, this result most closely reproduces the first mode that is yielded by simulations.

The differences between simulated and analytical results presented here demonstrate that some finite size effects are not captured by analytical expressions. More complex nanoscale systems will be discussed in dedicated chapters, and there, we will need to rely more heavily

on results obtained from complete simulations instead of analytical models. Before continuing that study, let us now get an overview of technological aspects of magnonics.

2.4.4. Magnonic Crystals (MCs)

Using lithography techniques and nanofabrication, material can be removed from a uniform waveguide to create patterned waveguides[85] with discrete translational symmetry. This leads to a periodic variation in total energy E_{tot} as well. As E_{tot} depends upon both magnetization $\mathbf{M}$ and effective magnetic field $\mathbf{H}_{\text{eff}}$, its variation can also be controlled by controlling $\mathbf{H}_{\text{eff}}$.[3] Similar to how Bloch theorem may be used in terms of electronic or photonic crystals,[38] a theory for calculation of SW dispersion in magnonic crystals has also been developed.[51,217] MSs can also be used to calculate SW dispersion in MCs. These methods have been discussed in some detail in Chap. 3. Patterned waveguides are essentially 1D MCs. The dependence of SW dispersion in an 1D antidot waveguide on various factors is also studied in the following chapters. We also discuss 2D MCs in Chap. 9. Let us now consider how elements like magnonic waveguides and crystals function as active and passive components of magnonics devices.

2.4.5. Magnonic Devices

Magnonic devices – which aim to use SW for information processing – have attracted the attention of the research community due to the following potential advantages over their electronic and photonic counterparts:[69]

- Easy manipulation of device characteristics by controlling the bias magnetic field $\mathbf{H}_{\text{bias}}$.
- Magnetic nano–elements are also non–volatile memory elements, thus facilitating their easy integration with current technological ecosystem, e.g., magneto–optical disks and read heads in MRAMs.
- In microwave and submillimetre ranges, SWs have considerably lower wavenumbers, which can be used for miniaturization of certain devices.

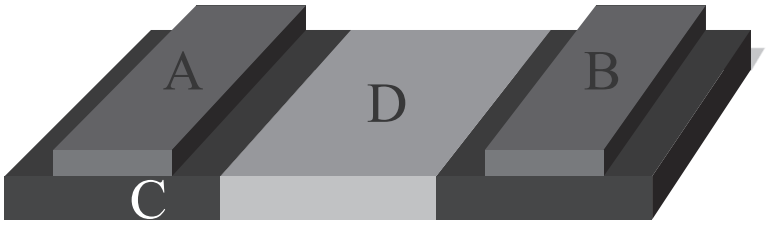

Figure 2.6.: A schematic of magnetostatic SW based generic magnonic device. Input and output antennae, waveguide and device's functional medium are marked as A, B, C and D, respectively. Source: Ref. 69.

A schematic of a typical magnonic device is presented in Fig. 2.6. Here, A and B are SW source and detector antennae. C is an uniform waveguide which conducts SWs as it is, and D is the functional medium such as an MC which manipulates the information contained in SWs. This assembly is usually micron sized and used with magnetostatic SWs. Ferrites, such as YIG, are typically used for waveguide C, because they tend to have very low SW damping and thus allow the signal to carry for longer (≈ 1 mm) distances. Magnetic parameters may or may not be homogeneous in D. In the former case, it becomes uniform and similar to C. By controlling the external magnetic field and material parameters, D can be made to function[69] as a *phase shifter*, an *amplifier*, a *frequency mixer*, a *filter* or a *generator* of short trains of magnetostatic SWs.

The functional region D can also divide the SW signal into two parts and recombine them after a phase–shift, either constructively or destructively to mimic a Mach–Zehnder–type *interferometer*[38] for SWs. Apart from *logical switches* this can also be used to *transduce* an electric signal to a magnonic one.[5] Even the NAND (an universal gate) functionality has now been demonstrated.[82]

Although, YIG has a very low (SW) damping,[70] their films are difficult to grow on silicon and Py, as a ferromagnet, is better suited for integration with current silicon based technologies.[38] It has also been projected[74] that the number of operations per unit area per unit time (throughput) of magnonic logic can outperform CMOS logic by more than three orders of magnitude.

2.5. Magnetic Vortex Dynamics

The core of a magnetic vortex is marked by out of plane magnetization. The radius of this core, r_{core}, depends largely on the exchange length λ_{ex}, and the film thickness u as[16]

$$r_{\text{core}} = 0.68\lambda_{\text{ex}}\sqrt[3]{u/\lambda_{\text{ex}}} \tag{2.64}$$

For vortices formed in circular nanodisks, the out of plane component of magnetization m_z can point either up or down at the centre. Based on this polarity p of the vortex (core) can be assigned a value 1 or -1. Immediately around core m_z takes the sign of $-m_z$ $(r = 0)$, before taking near zero values. This gives the magnetic vortex core its 'halo' or 'dip'. Multiple analytical models[218–220] have been offered to describe the profile of magnetization within its core, however the experimentally observed halo,[134] has so far only been reproduced by MSs[221] and the generalized trial function introduced by Hubert and Schäfer.[174] This halo plays a key role in ultrafast vortex dynamics.[16] Apart from polarity, another attribute of a magnetic vortex is known as chirality c, which, depending upon the curl of magnetization around the edge of vortex can either be 1 (CCW) or -1 (CW).

If $\varphi = \tan^{-1}(m_y/m_x)$, the *winding number* n of a vortex with boundary S is defined as

$$n \equiv \frac{1}{2\pi}\oint_S \frac{d\varphi}{dS} \tag{2.65}$$

The winding number is 1 for a vortex and -1 for an *antivortex*.[16] A non–zero winding number provides topological stability to vortices and antivortices,[222] imposing a rule regarding the conservation of winding number unless a high torque is applied to undo it.[223,224] This also implies that the formation of a vortex must occur simultaneously with the formation of an antivortex, unless the vortex core nucleation occur on the boundary S. *Skyrmion number* (also called Pontryagin index) q,[225] is another conserved topological index, which is defined as[226]

$$q \equiv pn/2. \tag{2.66}$$

This means that vortex–antivortex annihilation can be spontaneous only if the pair has the same polarity. Otherwise, it must be mediated by a singularity like a Bloch point,[227]

where change in magnetization direction is marked by the presence or a region with vanishing magnetization. Energy released in such vortex–antivortex annihilation leads to SW generation.[228]

2.5.1. Polarity Switching

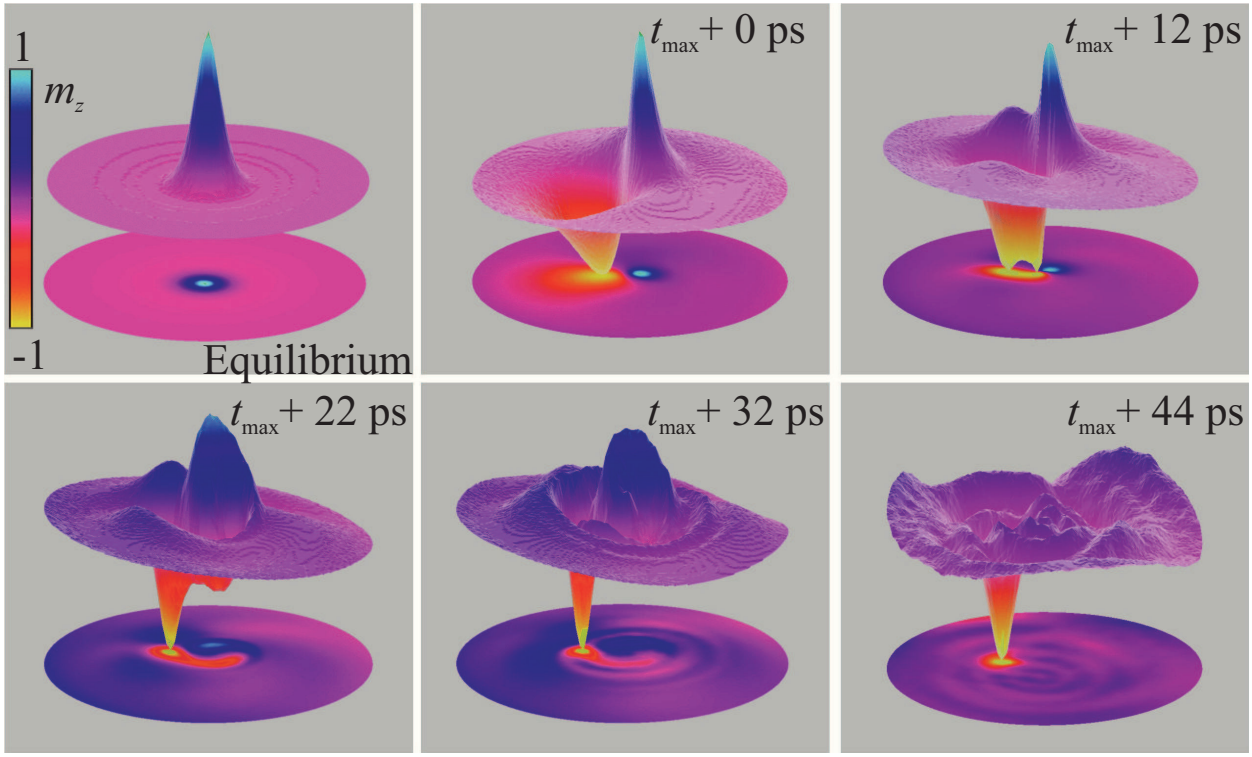

Figure 2.7.: Time evolution of z–component of magnetization in a magnetic vortex undergoing a core reversal. Source: Ref. 16.

Creation and annihilation of vortex–antivortex pairs also mediate *polarity switching* — a process where the polarity p changes to $-p$.[15] A time evolution of this core reversal, which lasts about 40 ps has been shown in Fig. 2.7.[16,229] Here, a circular nanodisk of radius 100 nm and thickness 20 nm are used with material parameters of Py assuming a damping $\alpha = 0.01$ and surface anisotropy $K_S = 0.1$ mJ/m^2. An in–plane Gaussian signal of 60 ps duration and a maxima of 80 mT at time t_{max}.

A production of vortex–antivortex pair, seen at $t_{max} + 12$ ps in Fig. 2.7, is believed to be mediating the polarity reversal.[128] While the energy from the signal is being absorbed, the winding and skyrmion numbers before and after this pair production remain conserved. Next,

the new antivortex annihilates with the old vortex, leaving the new vortex with opposite polarity intact. However, here the skyrmion number changes from 1/2 to −1/2. This, is marked by a release of energy in the form of SWs. Apart from the generation of SWs, the use of polarity switching in data storage has also been envisioned.[128,230]

2.5.2. Vortex Core Gyration

If the excitation signal, either in the form of a spin–polarized current or a changing magnetic field, is sufficiently small, it induces a translation of the vortex core around its equilibrium position. This is referred to as *magnetic vortex core gyration*. In the steady state — when the velocity of the core $\mathbf{v}$ does not change in magnitude, and if the shape of the magnetic structure is not altered greatly, the following Thiele's equation[146,174,231] describes this gyration:

$$\mathbf{F}_{\text{ext}} + \mathbf{G} \times \mathbf{v} + \alpha \overleftrightarrow{\mathbf{D}} \cdot \mathbf{v} = 0, \tag{2.67}$$

where $\mathbf{G}$ is the *gyrotropic vector* and $\overleftrightarrow{\mathbf{D}}$ is the net *dissipation tensor*. Using spherical polar co-ordinates where θ and ϕ are the polar and azimuthal angles, these quantities can be expressed as[16]

$$\mathbf{G} = -\frac{\mu_0 M_{\text{s}}}{|\gamma|} \int (\sin\theta \nabla\theta \times \nabla\phi)\, dV, \text{ and} \tag{2.68}$$

$$\overleftrightarrow{\mathbf{D}} = -\frac{\mu_0 M_{\text{s}}}{|\gamma|} \int \left(\nabla\theta\nabla\theta + \sin^2\theta \nabla\phi\nabla\phi\right). \tag{2.69}$$

For a magnetic vortex in a nanodisk, the above equations can be rewritten as[149,232,233]

$$\begin{aligned} \mathbf{G} &= -2\frac{\pi\mu_0 u M_{\text{s}}}{|\gamma|} np\hat{\mathbf{z}} \\ &= -Gp\hat{\mathbf{z}} : G > 0 \end{aligned} \tag{2.70}$$

$$\begin{aligned} \overleftrightarrow{\mathbf{D}} &= \begin{bmatrix} D_{xx} & D_{xy} \\ D_{yx} & D_{yy} \end{bmatrix} \\ &= \begin{bmatrix} D & 0 \\ 0 & D \end{bmatrix}, \end{aligned} \tag{2.71}$$

where

$$D = -\frac{\pi \mu_0 u M_\mathrm{s}}{|\gamma|} \ln \frac{R}{r_\mathrm{core}}. \tag{2.72}$$

Here R is the radius of the nanodisk.

Gyrotropic Frequency

If the vortex core is away from the centre of the nanodisk, a demagnetizing field is created, which attempts to restore the core's position $\mathbf{r}$ to the centre of the disk, resulting in a force

$$\mathbf{F}_\mathrm{ms} \equiv -\kappa \mathbf{r}, \tag{2.73}$$

where the positive constant κ is given by[137,234]

$$\kappa = \pi \frac{\mu_0 M_\mathrm{s}^2 u}{\chi_0}, \tag{2.74}$$

where, the initial susceptibility χ_0, can be obtained from the relation

$$\frac{1}{\chi_0} = \frac{2u}{R}\left[\ln\left(\frac{8R}{u}\right) - \frac{1}{2}\right] : \frac{u}{R} \ll 1. \tag{2.75}$$

Taking this into account while ignoring damping and any external forces, Eq. (2.67) changes to

$$\begin{aligned} -\kappa \mathbf{r} + \mathbf{G} \times \mathbf{v} &= 0 && (2.76)\\ \implies -\kappa \mathbf{r} - Gp\hat{\mathbf{z}} \times (2\pi f_0 p \hat{\mathbf{z}} \times \mathbf{r}) &= 0 && (2.77)\\ \implies f_0 &= \frac{|\gamma|\, M_\mathrm{s}}{4\pi\chi_0} \left(\because \mathbf{r} \perp \hat{\mathbf{z}}\ \&\ p^2 = 1\right). && (2.78) \end{aligned}$$

Equation (2.78) systematically overestimates[137] the gyration frequency f_0, because the rigid vortex model[149] used here, predicts the development of additional surface charges at the edge of nanodisk, attributing greater energy to the dynamics. By imposing a boundary condition which prohibits the development of surface charges we get[137,153]

$$f_0 = \frac{|\gamma|\, M_\mathrm{s}}{9\pi\chi_0}, \tag{2.79}$$

where

$$\frac{1}{\chi_0} = \frac{9.98u}{R} : \frac{u}{R} \ll 1. \tag{2.80}$$

The frequency of vortex core gyration as predicted by Eq. (2.79) has been verified by simulation[137] and also experimental results[147,235] using a Py (where damping is low). It can be seen from Eq. (2.79), that the gyrotropic frequency of a vortex in a nanodisk only depends upon its aspect ratio and the saturation magnetization of the material used.

External Forces on The Vortex Core

Let us rewrite Thiele's Eq. (2.67), taking the restoring force $\mathbf{F}_{\text{ms}}$ from Eq. (2.73):

$$\mathbf{F}_{\text{ext}} - \kappa\mathbf{r} + \mathbf{G} \times \mathbf{v} + \alpha \overleftrightarrow{\mathbf{D}} \cdot \mathbf{v} = 0. \tag{2.81}$$

At equilibrium $\mathbf{r} = 0$ and $\mathbf{v} = 0$. Thus, a non–zero $\mathbf{F}_{\text{ext}}$ is required to trigger the dynamics. This force is usually provided by an external magnetic field or by spin–transfer torque (STT). Force experienced due to an external magnetic field $\mathbf{H}_{\text{ext}}$ is given by[151] $\mu\,(\hat{\mathbf{z}} \times \mathbf{H}_{\text{ext}})$ where (assuming no side charges[153]), factor[145] $\mu = 2\pi M_{\text{s}} Ruc/3$. We can see that this force depends upon the chirality c of the vortex. Thus, the initial response to an applied magnetic field is mainly controlled by the chirality of the vortex.

STT can contribute to both gyrotropic and dissipative forces. In the presence of spin–polarized current where the drift velocity of the electrons is $\mathbf{u}$, the Thiele's equation changes to the following form:[236–239]

$$-\kappa\mathbf{r} + \mathbf{G} \times (\mathbf{v} - \mathbf{u}) + \overleftrightarrow{\mathbf{D}} \cdot (\alpha\mathbf{v} - \beta\mathbf{u}) = 0. \tag{2.82}$$

Here, the dimensionless factor β (typically of the order of 10^{-2})[236] is a measure of non–adiabaticity of the spin–current. When $\alpha \approx \beta$ and $\mathbf{r} \approx 0$, we get $\mathbf{v} \approx \mathbf{u}$. Thus, the initial displacement of vortex core is along the direction of the electrons' drift velocity, and unlike the initial displacement from the external field, it is independent of the vortex chirality.[239] This can be useful as chirality of vortex is difficult to manipulate.[240,241]

In a network of N interacting vortices, the force $\mathbf{F}^i_{\text{ext}}$ on the i^{th} vortex is given by

$$\mathbf{F}^i_{\text{ext}} = -\frac{\delta W\left(\mathbf{r}_1, \mathbf{r}_2, \mathbf{r}_3, \cdots, \mathbf{r}_N\right)}{\delta \mathbf{r}_i} \tag{2.83}$$

After an initial disturbance which can be triggered either by an external field or by dint of STT, the equation of motion (assuming no external forces and negligible damping) can be described by Eq. (2.76). We can also see from Eq. (2.70) that $\mathbf{G}$ depends on the polarity of the vortex (or antivortex). Thus the sense of rotation of the vortex core is controlled by polarity of the vortex. It has also been observed that an excitation signal rotating CCW (or CW) induces a greater gyration of the vortex core when the polarity is up (or down).[152] Further, polarity dependent logical operations[162] and high signal transfer efficiency[155] has also been reported. In Chap. 12, we note that an asymmetric amplification of gyration can be obtained when signal is transferred from one vortex to another by carefully controlling the relative polarities of the interacting vortices. This can be used to mimic the states of a conventional electronic transistor.

3. Methods

The scientific method followed in this thesis can be outlined in terms of the following steps:

- **Problem design**: To study the phenomena of SW dispersion in nanoscale systems, we first design the system. Then we agree upon either a geometrical or a material design parameter of the system which is theorized to affect SW dispersion.

- **Simulation**: Once the design of the system is finalized, we perform simulations to predict the nature of dependence of SW dispersion on the considered design parameter. Typically, the FDM based OOMMF is used for this purpose as it yields sufficiently accurate results in a manageable time frame.

- **Analysis of simulation data**: The simulation data is in the form of magnetization as a function of space and time where both space and time coordinates are evenly spaced. Discrete Fourier transform (DFT) is performed on this data, to obtain the energy spectral density (ESD) in different real and inverse domains. This gives us valuable information about the magnetization dynamics, such as, SW dispersion relation, iso–frequency lines or the eigenfrequency of vortex gyration.

- **Fabrication**: If the simulated results contain something of interest, we may want to verify the finding experimentally. In order to do that we first fabricate the simulated system as per the design. Fabrication can be done by using different synthesis or lithography techniques. Although, significant advancements have been made recently in this area, it is still difficult to fabricate huge arrays with features involving deep nanoscale precision. As it will be discussed in the following chapters, some aspects of the magnetization dynamics, such as SW dispersion, can tolerate some fabrication defects.[242] On the other hand, given finite amount of computational resources, it is also

impossible to simulate systems exactly as they are fabricated. Some, techniques like the use of periodic boundary condition (PBC)[243,244] have helped abridge this divide between simulated and fabricated systems, but there is still a lot of ground to be covered.

- **Characterization**: Some imaging techniques, such as scanning electron microscopy (SEM), are needed to verify if the fabricated sample is in good condition. This step is similar to quality inspection of a manufactured part or device. Any samples featuring systematic defects are rejected at this point. Magnetic parameters, which are also measured at this point, should be in good agreement with known values.

- **Experimentation**: Experimental techniques, such as Time Resolved–Magneto–Optic Kerr Effect (TR–MOKE) is used to directly observe the magnetization dynamics. The experimental technique should be chosen carefully to allow the study of the effects of geometrical or material parameter as determined during the problem design.

- **Analysis of experimental data**: Experimental data may also need to be analysed in order to obtain the characteristic response in different cases of the designed problem.

- **Conclusion**: A close agreement between simulated and experimental results validate our finding. These results may also be compared with existing theoretical models discussed in Chap. 2. If no analytical models exist at this point, a new one may be proposed. These results are now disseminated through a conference presentation, a journal publication or a patent application.

The effort described in this thesis is largely focused on problem design, simulation and analysis. The methods of simulation, fabrication and characterization are covered in further detail in the following sections of this chapter. Analysis techniques are described in dedicated chapters as they have evolved over time. A summary of the analysis techniques in its generic form is presented in the concluding chapter. Experimental techniques, which are used to validate some basic findings presented here are discussed in Chap. 11. As, some aspects of the numerical techniques were developed during the course of this work itself, it has been validated by using a comparison with the well established plane wave method (PWM). The underlying theory of the PWM has been discussed in Sec. 3.4.

3.1. Micromagnetic Simulation

Most analytical methods, like the PWM[51] or the dynamical matrix method,[245] often make simplifying assumptions of perfection (*e.g.* a perfect MC) or linearity (linear dynamics) to solve the magnetization dynamics. Simplifying boundary conditions[213] are also used sometimes to make the task easier. Nevertheless, analytical methods are used very widely to treat simple systems for obtaining qualitative results as they are considerably faster and more scalable with system geometry when compared to simulation based computational methods. In contrast, computer simulations can be performed for real world finite systems or infinite ideal MCs (by the use of periodic boundary conditions[243,244]). They also yield more accurate and experimentally realizable results. Both, analytical and computational methods solve the LLG Eq. (2.41) recalled below:

$$\frac{d\mathbf{M}}{dt} = -|\bar{\gamma}|\,\mathbf{M}\times\mathbf{H}_{\text{eff}} - \frac{\alpha\,|\bar{\gamma}|}{M_{\text{s}}}\mathbf{M}\times(\mathbf{M}\times\mathbf{H}_{\text{eff}})\,.$$

The advantage of writing the LLG equation as an ordinary differential equation (ODE) in time, while abstracting the spatial derivatives in the components of effective magnetic field $\mathbf{H}_{\text{eff}}$, is the ease with which standard ODE solving algorithm, such as one of the Runge–Kutta type algorithms, may now be used.

Table 3.1.: Micromagnetic simulators. Source: Ref. 5.

Name	**Developers**	**Open Source**	**Method**
LLG Simulator	M. R. Scheinfein	Paid	FDM
MAGPAR	W. Scholtz	Free	FEM
MicroMagus	D. V. Berkov and N. L. Gorn	Paid	FDM
Nmag	H. Fangohr and T. Fischbacher	Free	FEM
OOMMF	M. Donahue and D. Porter	Free	FDM

Micromagnetic simulators[246] solve Eq. (2.41) with the help of the finite difference method (FDM) or the finite element method (FEM). The later of the two yields more precise results at the cost of greater computational resources in most cases.[247] OOMMF and Nmag are open source and very widely used by different groups around the world. Table 3.1[5] lists popular

micromagnetic simulation (MS) platforms commonly used for the purpose of simulating SW dynamics.

3.2. FDM and OOMMF

While modelling the sample geometry FDM based solvers, such as OOMMF uses cuboidal discretization cells where the cuboids (or cells) have the same dimensions. This is shown in Fig. 3.1[248] for the case of a semi–circular disk. Some disagreement, in the form of steps, can be seen. This produces some errors while estimating the magnetization dynamics which can be reduced by using smaller cell sizes.

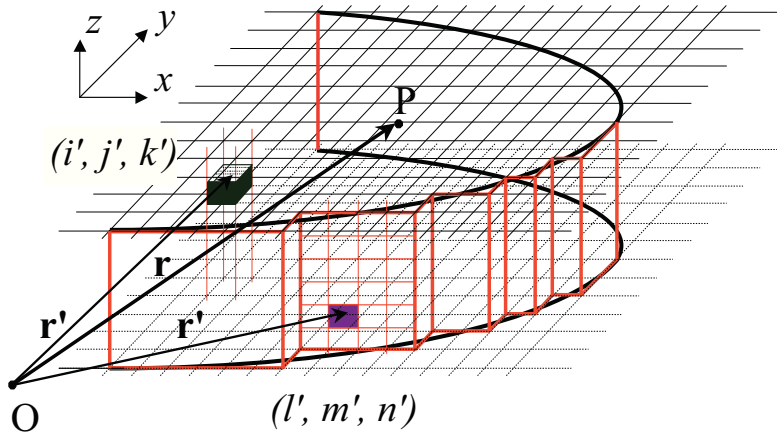

Figure 3.1.: A semi–circular disk modelled in terms of cuboidal regions. The straight red lines and the curved black lines mark the physical and numerical boundaries of the geometry. Source: Ref. 248.

Let us now recall Eq. (2.34):

$$\mathbf{H}_{\text{eff}} = \mathbf{H}_{\text{ext}} + \mathbf{H}_{\text{exch}} + \mathbf{H}_{\text{dem}} + \mathbf{H}_{\text{anis}}.$$

Thus, the effective field can be calculated as the sum of fields corresponding to different energies as described in Sec. 2.2. Alternatively, one can calculate the total energy first and find out the effective field as its functional derivative w.r.t. magnetization:[249]

$$\mathbf{H}_{\text{eff}} = -\frac{\delta e_{\text{tot}}}{\mu_0 \delta \mathbf{M}}. \tag{3.1}$$

Here e_{tot} is the total energy density. This energy based approach is used by OOMMF. Let us now discuss how different energy terms described in Sec. 2.2 can be approximated for a discretized sample.

3.2.1. Numerical Approximations of Magnetic Energies

Let a geometry be discretized into N cuboidal cells with $\mathbf{r}_i$ and V_i denoting the position (of centre) and volume of the i^{th} cell. Then, the Zeeman energy can be approximated as

$$E_Z \approx -\mu_0 \sum_{i=1}^{N} \mathbf{M}(\mathbf{r}_i) \cdot \mathbf{H}_{\text{ext}}(\mathbf{r}_i) V_i. \tag{3.2}$$

The maximum error with this approximation is of the order of[248] $\nabla^2 V$, where ∇ is the maximum cell dimension and V is the total volume of the geometry.

While computing the exchange energy numerically, one can approximate Eq. (2.18) in the following manner:[250]

$$E_{\text{exch}} \approx -\sum_{i=1}^{N} V_i \sum_{j \in \{N(i)\}} A_{ij} \frac{\mathbf{m}(\mathbf{r}_i) \cdot (\mathbf{m}(\mathbf{r}_j) - \mathbf{m}(\mathbf{r}_i))}{|\mathbf{r}_j - \mathbf{r}_i|^2}, \tag{3.3}$$

where $\{N(i)\}$ is the set of sites in the neighbourhood of site i. The corresponding exchange field may be approximated as

$$\mathbf{H}_{\text{exch}}(\mathbf{r}_i) = \lambda_{\text{ex}}^2(\mathbf{r}_i) \sum_{j \in \{N(i)\}} \frac{(\mathbf{m}(\mathbf{r}_j) - \mathbf{m}(\mathbf{r}_i))}{|\mathbf{r}_j - \mathbf{r}_i|^2}. \tag{3.4}$$

Here too, the error is $O\nabla^2 = O|\mathbf{r}_j - \mathbf{r}_i|^2$. Equation (3.3) can be simplified using the fact that $\mathbf{m}(\mathbf{r}_i) \cdot \mathbf{m}(\mathbf{r}_i) = 1$. However, that may degrade numerical precision if $\mathbf{m}(\mathbf{r}_i)$ is almost parallel to $\mathbf{m}(\mathbf{r}_j)$.[251] If the cell size is too big, larger angles between $\mathbf{m}(\mathbf{r}_i)$ and $\mathbf{m}(\mathbf{r}_j)$ may lead to issues like collapse of Néel walls[248,252] or artificial pinning hindering the motion of Bloch points.[253] As discussed in sub–Sec. 2.5.1, Bloch points play an important role in polarity switching. These issues can be overcome by reducing the size of cuboids used for discretization of the geometry.[248]

The anisotropy energy given by Eq. (2.28) can be approximated as following:[248]

$$E_K \approx \begin{cases} -\sum\limits_{i=1}^{N} K_1(\mathbf{r}_i)\left(\mathbf{m}(\mathbf{r}_i)\cdot\hat{\mathbf{u}}(\mathbf{r}_i)\right)^2 V_i & \text{(Uniaxial)} \\ \sum\limits_{i=1}^{N}[K_1(\mathbf{r}_i)\left(m_x^2(\mathbf{r}_i)\,m_y^2(\mathbf{r}_i)+m_y^2(\mathbf{r}_i)\,m_z^2(\mathbf{r}_i)+m_x^2(\mathbf{r}_i)\,m_z^2(\mathbf{r}_i)\right) & \\ \quad +K_2 m_x^2(\mathbf{r}_i)\,m_y^2(\mathbf{r}_i)\,m_z^2(\mathbf{r}_i)]V_i & \text{(Cubic)} \end{cases} . \quad (3.5)$$

If K_1 is positive, $\hat{\mathbf{u}}$ is an unit vector in the direction of easy axis. Otherwise, it is normal to the easy plane. In the case of cubic anisotropy, the crystal axes need to be oriented parallel to the coordinate axes. Here too, the error in numerical approximation is $O(\nabla^2)$. The corresponding field equations can be written as

$$\mathbf{H}_{\text{anis}}(\mathbf{r}_i) = \begin{cases} \left(\mathbf{m}(\mathbf{r}_i)\cdot\hat{\mathbf{u}}(\mathbf{r}_i)\right)\frac{2K_1}{\mu_0 M_{\text{s}}}\hat{\mathbf{u}}(\mathbf{r}_i) & \text{(Uniaxial)} \\ -\frac{2\overleftrightarrow{\mathbf{N}}^K(\mathbf{r}_i)\cdot\mathbf{m}(\mathbf{r}_i)}{\mu_0 M_{\text{s}}} & \text{(Cubic)} \end{cases} . \quad (3.6)$$

Here, $\overleftrightarrow{\mathbf{N}}^K$ is a tensor with diagonal entries only:

$$\overleftrightarrow{\mathbf{N}}^K(\mathbf{r}_i) = \begin{bmatrix} N_{11}^K(\mathbf{r}_i) & 0 & 0 \\ 0 & N_{22}^K(\mathbf{r}_i) & 0 \\ 0 & 0 & N_{33}^K(\mathbf{r}_i) \end{bmatrix}, \quad (3.7)$$

such that:

$$N_{11}^K(\mathbf{r}_i) = K_1(\mathbf{r}_i)\left(m_y^2(\mathbf{r}_i)+m_z^2(\mathbf{r}_i)\right)+K_2(\mathbf{r}_i)\,m_y^2(\mathbf{r}_i)\cdot m_z^2(\mathbf{r}_i), \quad (3.8)$$

$$N_{22}^K(\mathbf{r}_i) = K_1(\mathbf{r}_i)\left(m_x^2(\mathbf{r}_i)+m_z^2(\mathbf{r}_i)\right)+K_2(\mathbf{r}_i)\,m_x^2(\mathbf{r}_i)\cdot m_z^2(\mathbf{r}_i), \quad (3.9)$$

$$N_{33}^K(\mathbf{r}_i) = K_1(\mathbf{r}_i)\left(m_x^2(\mathbf{r}_i)+m_y^2(\mathbf{r}_i)\right)+K_2(\mathbf{r}_i)\,m_x^2(\mathbf{r}_i)\cdot m_y^2(\mathbf{r}_i). \quad (3.10)$$

The demagnetizing energy and the corresponding field terms can be approximated as

$$E_{\text{d}} \approx \frac{\mu_0}{2}\sum_{i=1}^{N} V_i\mathbf{M}(\mathbf{r}_i)\cdot\sum_{j=1}^{N}\overleftrightarrow{\mathbf{N}}(\mathbf{r}_i-\mathbf{r}_j)\cdot\mathbf{M}(\mathbf{r}_j), \text{ and} \quad (3.11)$$

$$\mathbf{H}_{\text{dem}}(\mathbf{r}_i) \approx \sum_{j=1}^{N}\overleftrightarrow{\mathbf{N}}(\mathbf{r}_i-\mathbf{r}_j)\cdot\mathbf{M}(\mathbf{r}_j), \quad (3.12)$$

respectively. Here $\overleftrightarrow{\mathbf{N}}$ is the discrete analogue of the demagnetizing tensor introduced in Eq. (2.49), whose components can be calculated using

$$4\pi dV N_{ij}(\mathbf{r}) = 8f(\mathbf{r}) - 4\sum_{\mathbf{s}\in\{A\}} f(\mathbf{s}) + 2\sum_{\mathbf{s}\in\{B\}} f(\mathbf{s}) - 2\sum_{\mathbf{s}\in\{B\}} f(\mathbf{s}). \tag{3.13}$$

Here $dV = dxdydz$ is the volume of the cuboid with its centroid at $(\mathbf{r}) = (x, y, z)$, and $i \in \{x, y, z\}$ and $j \in \{x, y, z\}$, and $\{A\}$, $\{B\}$ and $\{C\}$ are sets of position vectors in neighbourhood of $\mathbf{r}$, such that

$$\{A\} = \{(x \pm dx, y, z), (x, y \pm dy, z), (x, y, z \pm dz)\}, \tag{3.14}$$

$$\{B\} = \{(x \pm dx, y \pm dy, z), (x, y \pm dy, z \pm dz), (x \pm dx, y, z \pm dz)\}, \tag{3.15}$$

$$\{C\} = \{(x \pm dx, y \pm dy, z \pm dz)\}. \tag{3.16}$$

For diagonal (N_{ii}) and off-diagonal (N_{ij}) terms of $\overleftrightarrow{\mathbf{N}}$, the function $f(\mathbf{r}) = f(x, y, z)$ in Eq. (3.13) can be expressed as[248]

$$f(x,y,z) = \begin{cases} \frac{1}{2}y\left(z^2 - x^2\right)\sinh^{-1}\left(\frac{y}{\sqrt{x^2+z^2}}\right) \\ \quad +\frac{1}{2}z\left(y^2 - x^2\right)\sinh^{-1}\left(\frac{z}{\sqrt{x^2+y^2}}\right) \\ \quad -xyz\tan^{-1}\left(\frac{yz}{xr}\right) \\ \quad +\left(2x^2 - y^2 - z^2\right)r/6 & : i = j = x. \\ xyz\sinh^{-1}\left(\frac{z}{\sqrt{y^2+z^2}}\right) \\ \quad +\frac{1}{6}y\left(3z^2 - y^2\right)\sinh^{-1}\left(\frac{x}{\sqrt{y^2+z^2}}\right) \\ \quad +\frac{1}{6}x\left(3z^2 - x^2\right)\sinh^{-1}\left(\frac{y}{\sqrt{x^2+z^2}}\right) \\ \quad -\frac{1}{2}y^2z\tan^{-1}\left(\frac{xz}{yr}\right) - \frac{1}{2}x^2z\tan^{-1}\left(\frac{yz}{xr}\right) \\ \quad -\frac{1}{6}z^3\tan^{-1}\left(\frac{xy}{zr}\right) - xyr/3 & : i \neq j \neq z \neq i. \end{cases}$$

Here $\sinh^{-1}(l) = \log\left(l + \sqrt{1+l^2}\right)$.

Equation (3.12) essentially defines demagnetizing field $\mathbf{H}_{\text{dem}}$ as the discrete convolution of demagnetizing tensor $\overleftrightarrow{\mathbf{N}}$, with magnetization $\mathbf{M}$. This can allow for efficient computation

of the field using fast Fourier transform (FFT) techniques.[254]

Once energy or field terms are computed numerically w.r.t. to position $\mathbf{r}$, we can now find the $\mathbf{H}_{\text{eff}}$ as the sum of its constituents and proceed with solving the LLG ODE w.r.t. time while giving due considerations to initial and boundary conditions.

3.2.2. Boundary Conditions

Differential equation require some boundary and initial conditions to obtain a unique solution. In the case of the LLG equation, the initial condition is typically supplied in the problem design as $\mathbf{M}(\mathbf{r}, t = 0)$. This is a relaxed state of magnetization before a signal is provided to trigger the dynamics.

The general form of boundary conditions * (in addition to the Maxwell boundary conditions at external faces of the ferromagnetic plane of thickness u, proposed by Guslienko and Slavin[255] takes into account both dipolar pinning and pinning induced by uniaxial surface anisotropy:

$$\mathbf{M} \times \left(\lambda_{\text{ex}}^2 \frac{\partial \mathbf{M}}{\partial \hat{\mathbf{n}}} + \frac{2K_S}{\mu_0 M_{\text{s}}^2} (\mathbf{M} \cdot \hat{\mathbf{n}}_a) \hat{\mathbf{n}}_a + u\mathbf{H}_{\text{dem}} \right) = 0, \tag{3.17}$$

where $\frac{\partial \mathbf{M}}{\partial \hat{\mathbf{n}}}$ is the directional derivative of magnetization at the boundary. The uniaxial surface anisotropy is defined by its strength K_S and orientation $\hat{\mathbf{n}}_a$. $\mathbf{H}_{\text{dem}}$ depends on the thickness u and in–plane sizes R of the system (e.g., stripe width). It was shown[255] that for small systems($\sqrt{Ru} < \lambda_{\text{ex}}$) the magnetization pinning can be achieved only in the presence of strong surface anisotropy. Therefore, in the exchange limit the Rado–Weertman boundary condition,[256] which simply neglects the dipolar pinning, is sufficient.

Note that the surface anisotropy field (second term in the brackets in Eq. (3.17)) depends monotonously on K_S. As a result, the logarithmic derivative of the components of dynamical magnetization $\left(\frac{\partial m_i}{\partial \hat{\mathbf{n}}}\right)/m_i$ (i indicates the Cartesian components of $\mathbf{m}$) taken on the side faces of the waveguide also has monotonous dependence on K_S in the regime of linear dynamics[255] and approaches the values $\pm\infty$ – *pinned boundary conditions* – and 0 – *unpinned boundary conditions* – for high and low values of K_S, respectively. Once we have our boundary conditions in order, we can proceed to solve the LLG ODE.

*Parts of this sub–section is based on Kłos *et al.* Phys. Rev. B **86**, 184433 (2012).

Sometimes, a problem may require us to model geometries where one (*e.g.* a wave-guide) or two (*e.g.* a 2D MC) dimensions are infinite. If these systems posses translational symmetry, 1D or 2D periodic boundary condition (PBC) may be used. In OOMMF these boundary conditions are presently enabled by employing some publicly written extensions.[243,244] Under periodic boundary conditions the exchange and demagnetizing fields are calculated with the following in mind:

$$\mathbf{H}_{\text{exch}}(\mathbf{r}) = \begin{cases} \mathbf{H}_{\text{exch}}(\mathbf{r}+\mathbf{a}_1) & \text{(1D PBC)} \\ \mathbf{H}_{\text{exch}}(\mathbf{r}+\mathbf{a}_1+\mathbf{a}_2) & \text{(2D PBC)} \end{cases} \tag{3.18}$$

$$\mathbf{H}_{\text{dem}}(\mathbf{r}) = \begin{cases} \mathbf{H}_{\text{dem}}(\mathbf{r}+\mathbf{a}_1) & \text{(1D PBC)} \\ \mathbf{H}_{\text{dem}}(\mathbf{r}+\mathbf{a}_1+\mathbf{a}_2) & \text{(2D PBC)} \end{cases} \tag{3.19}$$

Here $\mathbf{a}_1$ and $\mathbf{a}_2$ represent the periodicity in mutually orthogonal directions.

3.2.3. Solving The LLG Equation in OOMMF

In this work, the $4th$ order Runge–Kutta method has been used to solve the LLG equation as an ODE in time.

$4th$ order Runge–Kutta method

Let magnetization be known at time t_1 as $\mathbf{M}(\mathbf{r}, t_1)$ or $\mathbf{M}_1(\mathbf{r})$. Since different magnetic energies, depend upon magnetization and the external field $\mathbf{H}_{\text{ext}}(\mathbf{r}, t_1)$, the effective magnetic field can be expressed as a function of magnetization, position and time as

$$\mathbf{H}_{\text{eff}}(\mathbf{r}, t) = \mathbf{h}(\mathbf{M}, \mathbf{r}, t). \tag{3.20}$$

Thus the LLG equation can be rewritten as

$$\begin{aligned} \frac{d\mathbf{M}}{dt} &= -|\bar{\gamma}|\,\mathbf{M}\times\mathbf{H}_{\text{eff}} - \frac{\alpha|\bar{\gamma}|}{M_{\text{s}}}\mathbf{M}\times(\mathbf{M}\times\mathbf{H}_{\text{eff}}) \\ &= -|\bar{\gamma}|\,\mathbf{M}\times\mathbf{h}(\mathbf{M},\mathbf{r},t) - \frac{\alpha|\bar{\gamma}|}{M_{\text{s}}}\mathbf{M}\times(\mathbf{M}\times\mathbf{h}(\mathbf{M},\mathbf{r},t)) \\ &= \mathbf{f}(\mathbf{M},\mathbf{r},t). \end{aligned} \tag{3.21}$$

So for i^{th} cuboid with centroid at $\mathbf{r}_i$, we can write

$$\left.\frac{d\mathbf{M}}{dt}\right|_{\mathbf{r}=\mathbf{r}_i} = \mathbf{f}\left(\mathbf{M}, \mathbf{r}=\mathbf{r}_i, t\right) = \mathbf{f}_i\left(\mathbf{M}, t\right). \tag{3.22}$$

Here, the rate of change of magnetization at site i is being described by a vector function $\mathbf{f}_i$. Let us now define $\mathbf{k}_{i1}$, $\mathbf{k}_{i2}$, $\mathbf{k}_{i3}$ and $\mathbf{k}_{i4}$ as following:

$$\mathbf{k}_{i1} = \mathbf{f}_i\left(\mathbf{M}_1, t_1\right), \tag{3.23a}$$

$$\mathbf{k}_{i2} = \mathbf{f}_i\left(\mathbf{M}_1 + \frac{h}{2}\mathbf{k}_{i1}, t_1 + \frac{h}{2}\right), \tag{3.23b}$$

$$\mathbf{k}_{i3} = \mathbf{f}_i\left(\mathbf{M}_1 + \frac{h}{2}\mathbf{k}_{i2}, t_1 + \frac{h}{2}\right), \text{ and} \tag{3.23c}$$

$$\mathbf{k}_{i4} = \mathbf{f}_i\left(\mathbf{M}_1 + h\mathbf{k}_{i3}, t_1 + h\right). \tag{3.23d}$$

Now, we can obtain $\mathbf{M}\left(\mathbf{r}, t_2\right) = \mathbf{M}_2$, where time step $h = t_2 - t_1$ as

$$\mathbf{M}\left(\mathbf{r}, t_2\right)\big|_{\mathbf{r}=\mathbf{r}_i} = \mathbf{M}\left(\mathbf{r}, t_1\right)\big|_{\mathbf{r}=\mathbf{r}_i} + \frac{h}{6}\left(\mathbf{k}_{i1} + 2\mathbf{k}_{i2} + 2\mathbf{k}_{i3} + \mathbf{k}_{i4}\right). \tag{3.24}$$

Thus we can find how magnetization changes as time goes from t_1 to t_2 in a time step h for each position $\mathbf{r}_i$. Now, let $\mathbf{M}'\left(\mathbf{r}, t_2\right)$ be calculated using Eqs. 3.23 and 3.24 with two equal time steps of $h' = h/2$. Thus the error $\epsilon\left(\mathbf{r}, t_2\right)$ going from t_1 to t_2 in one step can be defined as

$$\epsilon\left(\mathbf{r}, t_2\right) = \frac{h}{2}\left|\mathbf{f}\left(\mathbf{M}', \mathbf{r}, t_2\right) - \mathbf{f}\left(\mathbf{M}, \mathbf{r}, t_2\right)\right|. \tag{3.25}$$

For a step to be successful, $\max(\epsilon)$ should be less than a given value, which can be made smaller and smaller to get more and more accurate results. However this will cause simulations to run for longer periods of time. Thus, once a physical output parameter appears to converge, it is no longer necessary to further reduce these error limits. In simulations performed during this work convergence was tested based on the dimensions of cuboid. Limits of time steps h was decided based on the time–scale of underlying magnetization dynamics (*e.g.* 1 ps for SW dynamics and 10 ps for a vortex core's gyration). OOMMF allows the users to decide these limits for themselves.

3.3. FEM and Nmag

FEM based Nmag uses an adaptive tetrahedral mesh of varying edge lengths. Nmag yields more accurate results by sacrificing significant computational time and resources. Thus, OOMMF was the preferred platform of doing simulations in this work. Nmag has also been used on one occasion for the purpose of a comparative analysis where high accuracy was necessary. Most of the results produced here were validated against those yielded by the PWM.

3.3.1. FEM Meshing

In FDM a geometrical body is modelled as a set of packed cuboids. In the case of FEM tetrahedrons are used instead of cuboids. It makes the modelling much more accurate. In some cases it can also save computational resources by avoiding empty areas. Here we describe the *Delaunay triangulation algorithm*[257] which is popular due to its efficiency and robustness.

To start the mesh generation a set of distinct forming points $\{P\} = \{p_1, p_2, p_3, ..., p_N\}$ is randomly selected in the space of the geometry to be modelled. A *Voronoi region* $\{V(p_i)\}$ is defined as the set of points in space which are closer to p_i than any other point $p_j \in \{P\}$. Points which belong to two Voronoi regions $\{V(p_i)\}$ and $\{V(p_j)\}$ $(p_i, p_j \in \{P\})$ form the boundaries of the regions. Forming points whose Voronoi regions share a common boundary can be connected together to form the edges of a tetrahedral structure such that the circumsphere of any tetrahedron does not enclose any forming point. The edges of the tetrahedrons should be small enough to resolve magnetic domains such as a Bloch point. If that is not the case, or if the forming points do not approximate the finer features of the geometry, additional forming points need to be included in $\{P\}$ and the process of triangulation needs to be repeated. This algorithm is also presented in Fig. 3.2 for a planer system where tetrahedrons are replaced by triangles and circumspheres are replaced by circumcircles. Forming points and their respective Voronoi regions are seen in 2D space in Fig. 3.2 (a). A mesh of triangles is created using the forming points, such that their circumcircles do not include any forming points. If a new forming point has to be introduced

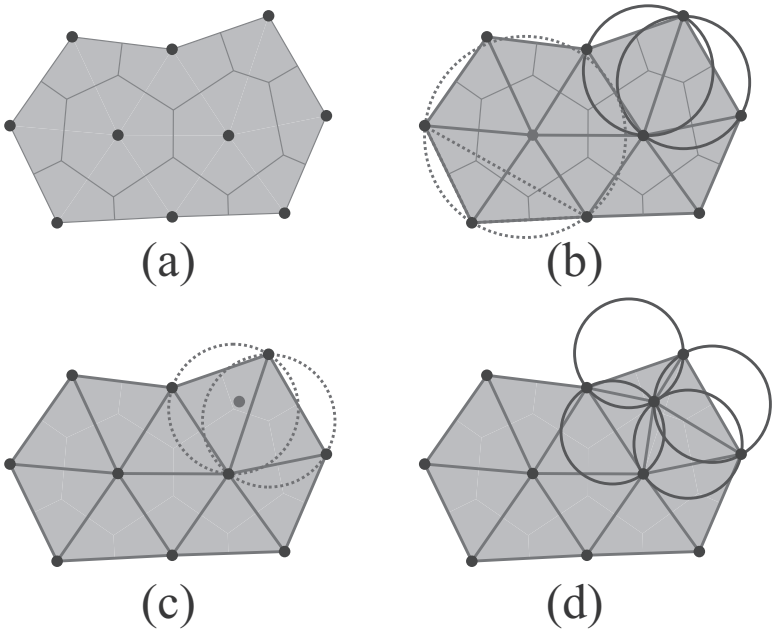

Figure 3.2.: (a) Forming points and their Voronoi regions. (b) A mesh of triangles using the forming points as vertices. Triangles whose circumcircle encompass any forming points are rejected. (c) A new forming point is introduced near an unacceptably long edge. This causes the rejection of two triangles whose circumcircles include the new forming point. (d) New smaller triangles are created whose circumcircles don't encompass any forming points. Source: Ref. 16.

to avoid an unacceptably long edge, new triangles are created to redefine the mesh.

3.3.2. Solving The LLG Equation using Nmag

Nmag can work with meshes produced by freewares such as Netgen. Once a mesh of tetrahedrons and their vertices are available, Galerkin discretization[258] is used to approximate the magnetization and effective magnetic fields. This is conceptually similar to the approximation process described in sub–Sec. 3.2.1. Following, this approximation of magnetization and effective field one can proceed to solve the LLG equation by implementing an algorithm of differential equation solution.

3.4. Plane Wave Method (PWM)

The PWM considers linear approximation of the LLG equation*. The magnetization dynamics is treated in the form of harmonic time precession of the magnetization with the angular frequency ω, expressed by the dynamical components of magnetization vector: $m_x(\mathbf{r},t) = m_x(\mathbf{r})e^{i\omega t}$ and $m_y(\mathbf{r},t) = m_y(\mathbf{r})e^{i\omega t}$. The dynamics of magnetization in the direction of bias field is neglected, i.e. we assume $M_z(\mathbf{r},t) \approx M_\mathrm{s}$. As a result the linearised LLG equations have a form of two linear differential equations for the precession amplitudes: $m_x(\mathbf{r})$ and $m_y(\mathbf{r})$. The amplitudes $m_x(\mathbf{r})$ and $m_y(\mathbf{r})$ can be transformed to the reciprocal space with the use of Bloch theorem. This allows to convert the linearized Landau-Lifshitz equations into the algebraic eigenvalue problem:

$$\begin{pmatrix} \{m_x(\mathbf{G})\} \\ \{m_y(\mathbf{G})\} \end{pmatrix} \hat{M} = \frac{i\omega}{\gamma\mu_0 H_0} \begin{pmatrix} \{m_x(\mathbf{G})\} \\ \{m_y(\mathbf{G})\} \end{pmatrix} \tag{3.26}$$

by Fourier transformation of material parameters (M_s, λ_ex) and the periodic factor of Bloch functions, where $\{m_x(\mathbf{G})\}$ and $\{m_y(\mathbf{G})\}$ denote the vectors with the set of Fourier coefficients for periodic parts of Bloch functions. The matrix $\hat{M}$ of the eigenvalue problem can be written in a block-matrix form:

$$\hat{M} = \begin{pmatrix} \hat{M}^{xx} & \hat{M}^{xy} \\ \hat{M}^{yx} & \hat{M}^{yy} \end{pmatrix}. \tag{3.27}$$

The submatrices in (3.27) are defined as follows:

$$\hat{M}^{xx}_{ij} = -\hat{M}^{yy}_{ij} = -i\frac{k_y + G_{y,j}}{H_0|\mathbf{k}+\mathbf{G}_j|} S(\mathbf{k}+\mathbf{G}_j) M_\mathrm{s}(\mathbf{G}_i - \mathbf{G}_j), \tag{3.28}$$

*This section is based on parts of Kłos *et al.* Phys. Rev. B **89**, 014406 (2014).

$$\begin{aligned}\hat{M}_{ij}^{xy} &= \delta_{ij} + \sum_l \frac{(\mathbf{k}+\mathbf{G}_j)\cdot(\mathbf{k}+\mathbf{G}_l)}{H_0}\lambda_{\mathrm{ex}}^2(\mathbf{G}_l-\mathbf{G}_j)M_{\mathrm{s}}(\mathbf{G}_i-\mathbf{G}_l) \\ &+ \frac{(k_y+G_{y,j})^2}{H_0|\mathbf{k}+\mathbf{G}_j|^2}(1-C(\mathbf{k}+\mathbf{G}_j))M_{\mathrm{s}}(\mathbf{G}_i-\mathbf{G}_j) \\ &- \frac{(G_{z,i}-G_{z,j})^2}{H_0|\mathbf{G}_i-\mathbf{G}_j|^2}M_{\mathrm{s}}(\mathbf{G}_i-\mathbf{G}_j)(1-C(\mathbf{G}_i-\mathbf{G}_j)), \end{aligned} \tag{3.29}$$

$$\begin{aligned}\hat{M}_{ij}^{yx} &= -\delta_{ij} - \sum_l \frac{(\mathbf{k}+\mathbf{G}_j)\cdot(\mathbf{k}+\mathbf{G}_l)}{H_0}\lambda_{\mathrm{ex}}^2(\mathbf{G}_l-\mathbf{G}_j)M_{\mathrm{s}}(\mathbf{G}_i-\mathbf{G}_l) \\ &- \frac{1}{H_0}C(\mathbf{k}+\mathbf{G}_j)M_{\mathrm{s}}(\mathbf{G}_i-\mathbf{G}_j) \\ &+ \frac{(G_{z,i}-G_{z,j})^2}{H_0|\mathbf{G}_i-\mathbf{G}_j|^2}M_{\mathrm{s}}(\mathbf{G}_i-\mathbf{G}_j)(1-C(\mathbf{G}_i-\mathbf{G}_j)), \end{aligned} \tag{3.30}$$

where indexes i, j, l of reciprocal lattice vectors $\mathbf{G}_i$ are integers. $M_{\mathrm{s}}(\mathbf{G}_i)$ and $\lambda_{\mathrm{ex}}^2(\mathbf{G}_i)$ are the Fourier coefficients associated with the saturation magnetization and exchange constant, respectively. The additional functions used in the equations above are defined as follows:

$$\begin{aligned} S(\mathbf{k}) &= \sinh\left(|\mathbf{k}|u/2\right)\mathrm{e}^{-|\mathbf{k}|u/2}; \\ C(\mathbf{k}) &= \cosh\left(|\mathbf{k}|u/2\right)\mathrm{e}^{-|\mathbf{k}|u/2}, \end{aligned} \tag{3.31}$$

where u denotes the thickness of the 1D or 2D magnonic crystal.

In order to use PWM for 1D structure one has to make the structure artificially periodic along the direction perpendicular to the waveguide axis. Here, the supercell method can be used, which exploits the fact that the properties of the confined system are equivalent to the properties of the set of its non–interacting copies. In Eqs. (3.28), (3.29), and (3.30) we have already used 2D wave vectors $\mathbf{k}$ and reciprocal lattice vectors $\mathbf{G}$ in the (x, y) space, which refers to the infinite sequence of parallel waveguides separated by an artificial material.[213] In 1D nanoscale waveguides, calculations are performed for y component of the wavevector equal 0, i.e. the direction of propagation of SWs is limited to the axis of the waveguide.

3.5. Fabrication Techniques

3.5.1. Thin–Film deposition

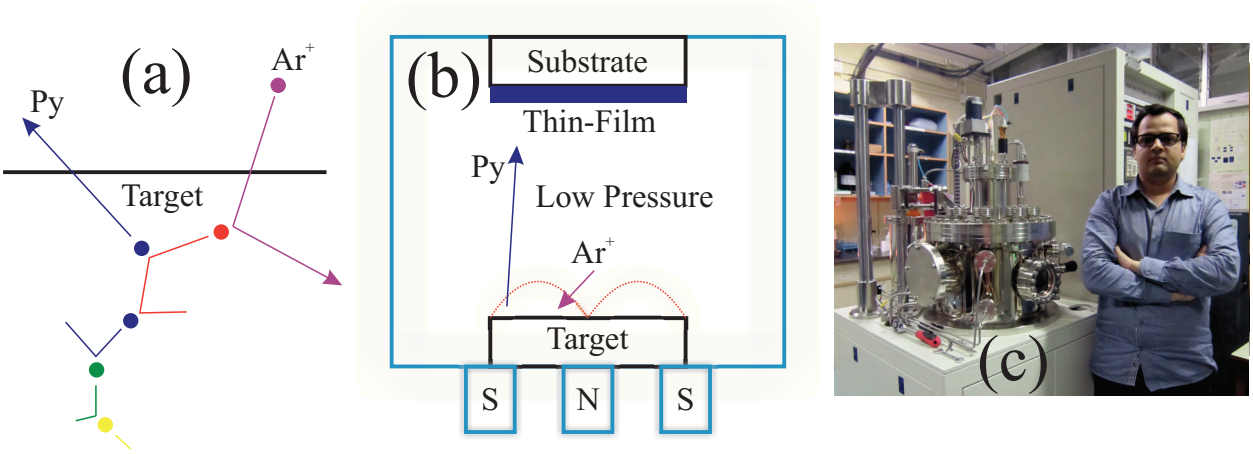

Figure 3.3.: (a) Incoming Ar^+ ion collides with atoms in the target. A sputtered atom is released upon a cascade of collisions. (b) A sketch of sputtering vacuum chamber showing dashed field lines. (c) My picture with a sputtering setup at the S. N. Bose National Centre for Basic Sciences, Kolkata.

The first step in fabrication is to deposit a thin layer of a magnetic material such as Py over a (typically silicon) substrate. This is accomplished by *sputter deposition*. *Sputtering* is a process where fast moving ions cause an ejection atoms from a *target*. These atoms from the target can be caught by the substrate allowing the thin–film to increase its thickness with time. The incoming Ar^+ ion triggers a cascade of collisions within the target as shown in Fig. 3.3 (a). Atoms are only able to leave the surface of the target if they have more energy than the surface binding energy. Dashed field lines in Fig. 3.3 (b) denote the electric and magnetic fields generated by a magnetron. This helps trap the argon plasma, which is sustained at a very low pressure of ≈ 10 mTorr, close to the target. The neutral atom leaving the surface is not affected by these fields. Atoms arriving to settle at the substrate increase the deposited film's thickness. A sputtering setup at the S. N. Bose National Centre for Basic Sciences is shown in Fig. 3.3 (c). Sometimes the use of multiple targets is considered desirable so that a thin dielectric layer may be placed over the magnetic thin–film. This will help prevent the oxidation of the thin film layer.

3.5.2. Lithography

Material can be removed from different locations in a deposited thin film using lithography techniques such as photolithography, e–beam lithography and focused ion beam (FIB) milling. The resolution of the lithography process depends upon the energy of the particles (or quasi–particles) being used. Both photolithography and e-beam lithography are used to define patterns on resist followed by deposition of materials and subsequent lift–off process, or dry or wet etching. On the other hand focused ion beam is used to directly mill out materials with high precision. Hence, photolithography and subsequent lift–off or etching may be used to create micrometer and sub–micrometer sized structures, while e–beam lithography and lift–off or etching or focused ion beam milling may be used for creating sub–100 nm structures. A schematic diagram showing optical and e–beam lithography is presented in Fig. 3.4.[6]

A photo–mask, which may be designed using computer aided design (CAD), containing a desired pattern. This facilitates the parallel growth of the micro–structures. In the case of e-beam or FIB lithography, the focus of etching needs to be controlled and moved from one spot to another during the lithography process.

The first step in optical lithography is cleaning of the Si(100) substrate by removing any organic or inorganic materials from its surface. This is done by submerging the substrate in an ultrasonic bath of acetone and water (20 mins each), respectively. The substrate is then dried with dry N_2 from a nitrogen gun. Then a spin coater is used to coat the surface of the substrate with a uniform layer of positive photoresist dissolved in an organic solvent. The thickness of the photoresist layer depends upon the its viscosity and the spinning speed of the spin coater. These parameters needs to calibrated to obtain a layer of desired thickness. A photo–mask containing the patterns to be fabricated is then placed on top of the substrate. A projection lens is used as shown in Fig. 3.4 to ensure a proper exposure of the coated substrate. This exposure causes the the polymer chains in the resist to break, which is then put into distilled water at room temperature, rinsed for 60 s and dried using dry the nitrogen gun. Next, the substrate is submerged into MIBK:IPA (1:3) (methyl isobutyl ketone : isopropyl alcohol) solution and rinsed for another 30 s. Finally, the substrate is submerged into acetone and rinsed (for 60 s) and dried again. This step causes the two dimensional

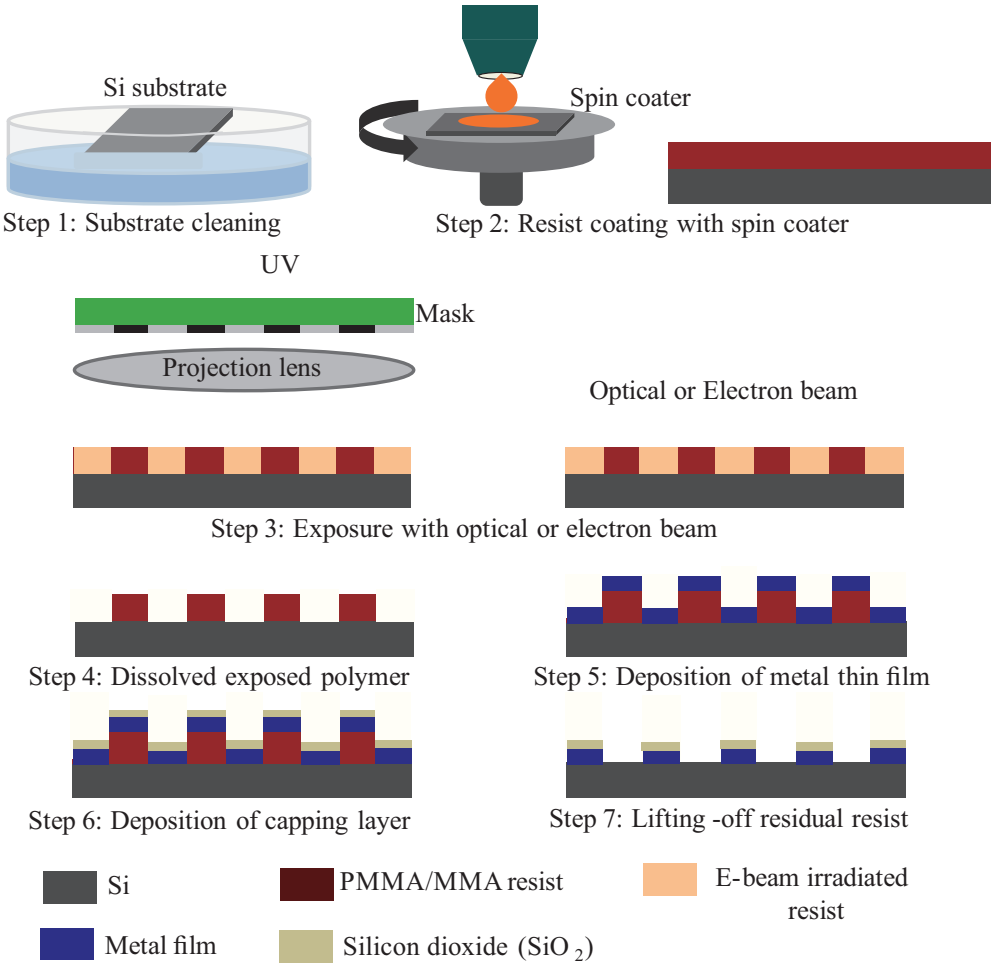

Figure 3.4.: Step–wise description of optical and e–beam lithography. Source: Ref. 6.

pattern of the photo–mask to appear as a three dimensional structure on the substrate. Now a film of Py can be deposited as described in sub–Sec. 3.5.1. Finally, the film deposited on the resist can be lifted–off using a stripper solution along with the resist leaving only the desired Py structure onto the Si surface.

High energy electrons are generated by accelerating a beam of electrons across a high voltage. The cleaning process is similar in optical and e–beam lithography. The spin coating is then done to produce a bilayer of polymethyl methacrylate (PMMA) and methyl methacrylate (MMA). The thickness of individual layers is controlled by calibration. As the PMMA layer develops faster than the MMA layer, the resulting overhung structure gives an undercut edge profile (of the resist) after development. A scanning electron microscope (SEM) can now be used to expose the resist with focused electrons. The pattern of this exposure can be controlled using a CAD software. The beam current and dose time are typically of the

order of 100 pA and 1μs, receptively. The exposed resist is then dissolved using developer solutions. A required 3D structure of the unexposed resists now survives on the substrate. A ferromagnetic layer can now be deposited as described in sub–Sec. 3.5.1. The lift–off to remove the unexposed resist (along with the film deposited over it) can now be done using stripper solutions. FIB milling, where heavier gallium ions are used instead of electrons can now be used to create even finer nanostructures after this point. The steps of cleaning, spin–coating, development and lift–off are similar to what is described before in the cases of optical and e–beam lithography techniques.

3.6. Sample Characterization

Even with all the recent advancements in nanofabrication, there are often numerous defects in the fabricated nanoscale samples. Any sample with serious systematic defects can not be used for experimentation. Due to the finite spot size of optical, electron or ion beams, deformations like rounded corners of the square dots or holes are always found. Inaccurate calibration of spin–coating, development of lift–off steps can also result in severe defects. A slow cooling of sputter deposited Py thin film can develop an inhomogeneous distribution of iron and nickel. During FIB milling gallium ion can get redeposited around the edges of the geometry which has just been removed. This can lead to pinning of magnetization dynamics at these edges.[213] Apart from these fabrication related defects, mechanical defects may also appear due to poor handling or storage of the samples. The oxidation and contamination of the magnetic sample is mitigated by coating the sample with a non–reactive dielectric substances like glass or Al_2O_3.

Once all the steps of fabrication are properly calibrated, and the sample is handled and stored carefully, even then one should examine the samples to verify that it is in good condition to start experimentation. SEM imaging was used in this work to observed the structure of the fabricated systems. A schematic of scanning electron microscope is presented in Fig. 3.5.[6] The sample is mounted on a small specimen stage by using a double–sided carbon tape. The sample's surface should be electrically conductive grounded to prevent any accumulation of electrostatic charge. A stream of electrons, or an electron beam, is

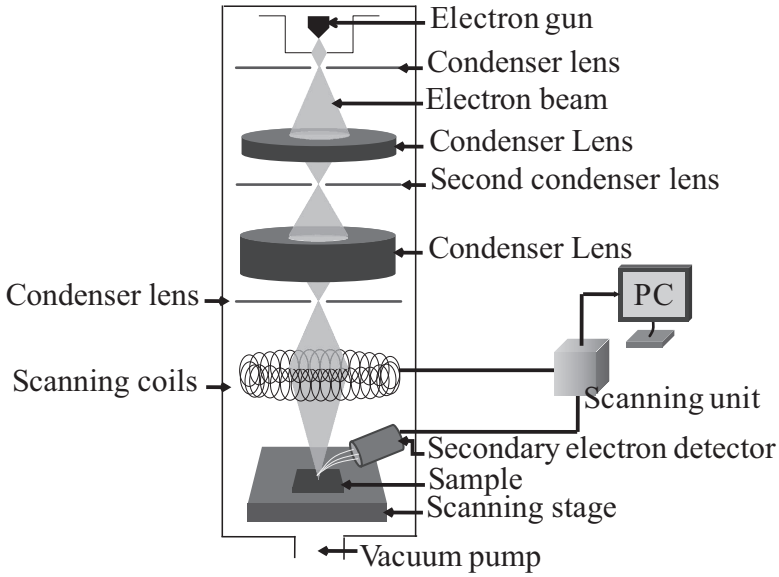

Figure 3.5.: Schematic of scanning electron microscope. Source: Ref. 6.

emitted either from an electron gun fitted with a tungsten filament cathode (thermionic) or from a field emission cathode. The later method produces narrower electron beam leading to a superior spatial resolution. The energy of the electrons in eV can typically vary from two to five orders of magnitude. After emission, the electrons are further accelerated by applying a voltage. The beam passes through a series of electromagnetic *condenser lenses* (see Fig. 3.5), which alter the spot size of the beam. An electromagnetic scanning coil, which can scan a rectangular region in a raster fashion, finally focuses the beam in the plane of the sample.[6] Upon an inelastic collision with the atoms in the sample, the energetic scanning electrons produce *secondary electrons*. The relative intensities of scanning and secondary electrons is then compared to generate the surface topography and morphology of samples.

4. Thin–Films, Waveguides and One–Dimensional Magnonic Crystals

*The spectrum of spin–waves (SWs) propagating in magnetic systems is important from both fundamental and applied points of view. Propagating SWs in spatially modulated magnetic systems, namely the magnonic crystals,[3,69] will form the building blocks for future microwave data communication. Recently, much effort has been made in understanding and tailoring the magnonic band structures (frequency versus wavevector) in various magnonic crystals with nanoscale features. The numerical simulation method is particularly important because this can be effectively used to design the desired magnonic band structures before starting the expensive nanofabrication methods. However, conventional micromagnetic simulators provide only the space–time data by solving the Landau-Lifshitz-Gilbert equation (LLG equation)[7,8] and meaningful conversion of that data to frequency and wavevector domains[259,260] poses several computational challenges. Object Oriented Micromagnetic Framework (OOMMF)[250] exploits the finite difference method to calculate magnetization dynamics.

The dispersion curves obtained by a 2D discrete Fourier transform (DFT)[261] of the space–time data obtained from micromagnetic simulations may contain artefacts. These mainly include lack of resolution in the frequency or wavevector domain, aliasing, spectral leakage and scalloping loss. These artefacts render the resultant dispersion diagram, unreadable. Discretization of continuous magnetic objects also leads to the appearance of an artificial period and as a result to the formation of an artificial band where the spectrum should

*This chapter is based upon Kumar *et al. J. Phys. D: Appl. Phys.* **45**, 015001 (2012).

be continuous.[259,260] The effect of most of these problems can be reduced by sampling the magnetization over a larger sample size or over a longer period of time. Range in frequency and wavevector domains can be increased by sampling the magnetization at a higher sampling rate in time and space domains, respectively. But, these measures will soon consume the available computational resources without providing much clarity to the obtained results. In this chapter we aim to document and standardize a sequence of steps that help in obtaining better results without compromising on the speed or extent of the numerical analysis. The improvement in quality, made by these methods, is established by a numerical comparison, which is further verified by the manual observation of the obtained dispersion diagrams. The presented method can also be used to compute the dispersion of SWs in different kinds of magnonic conductors,[5] which form a rich family of spatially modulated magnetic structures or artificial lattices designed to control the spectrum of SWs. Based on their geometry these magnonic conductors can be classified as one (1D), two (2D) or three dimensional (3D) and based on their continuity they can be either continuous waveguides or magnonic crystals (discrete arrays of dots or antidots). Magnonic crystals can also be made of more than one magnetic material, which allows us to classify them on the basis of homogeneity (as homogeneous and heterogeneous). While processing the results from a 3D magnonic crystal, the limited computational resources force us to use slower forms of computer memory.

In the following sections we explain how dispersion curves of SWs can be obtained by a 2D DFT of magnetization data which, in turn, is the output of a finite difference based ordinary differential equation (ODE) solver, such as OOMMF. We further discuss the shortcomings of this method and demonstrate how various techniques can be used to mitigate them. Material parameters of Py are used for the results shown here. Heavy damping is used to reach the state of saturated magnetization sooner under a constant bias. We have further applied the newly developed numerical technique to a range of magnonic media including magnetic nanostripes, magnetic nanowires and thin film elements. We have further calculated the dispersion curves for simple magnonic crystals with 1D and quasi-2D arrangements of periodic antidot arrays in permalloy thin films, which opens up allowed and forbidden magnonic bands.

4.1. Method

OOMMF produces the output data in several files where each file corresponds to a particular instance of simulation time and contains the information of magnetization distribution over the entire magnetic object. Being a finite difference method based ODE solver, OOMMF divides a magnetic object into an artificial periodic array of rectangular cuboids. The region of space, where no magnetic material is present, is assumed to have zero saturation magnetization. Subroutines were written to read the data into three four-dimensional matrices (one matrix for each component of magnetization), namely $M^i(t,x,y,z)$, $M^j(t,x,y,z)$ and $M^k(t,x,y,z)$. The variables t, x, y and z represent discrete equally spaced values of time and space. A dynamic component of magnetization (in our case orthogonal to the external bias field as we consider fully saturated samples) should be selected for the purpose of dispersion analysis. If $M^k(t,x,y,z)$ is one such component, we set $M^k_{x_m,y_n}(t,z) = M^k(t,x_m,y_n,z)$ to obtain a 2D matrix of the magnetization component, M^k at $x = x_m$, and $y = y_n$. The coordinate system should be appropriately rotated if the direction of propagation of spin–wave is neither of x, y or z. A 2D DFT can now be performed on this matrix to obtain the output $\tilde{M}^k_{x_m,y_n}(f,k_z) = F(M^k_{x_m,y_n}(t,z))$. The magnitude of this output corresponds to the magnitude of the corresponding Fourier components. If we take some particular frequency f, the corresponding wavevector k_z can be found by finding the high values of the Fourier component magnitudes for this particular frequency f. In order to visualize the dispersion curve we record a colour–weighted 3D plot (or a colour weighted scatter plot) of $P_{x_m,y_n}(f,k_z) \propto \log_{10}\left|\tilde{M}^k_{x_m,y_n}(f,k_z)\right|$ versus f and k_z. Thus, as seen in Fig. 4.1, when viewed from the top, the colour scale represents the Fourier power on a proportional decibel scale. Let the sum of $\left|\tilde{M}^k_{x_m,y_n}(f,k_z)\right|^2$ over all values of x_m and y_n be represented by $\left|\tilde{M}^k(f,k_z)\right|^2$ then $P(f,k_z) \propto \log_{10}\left|\tilde{M}^k(f,k_z)\right|$ will contain information of all the modes present in the magnetic medium for the chosen direction, namely z.

4.2. Results and Discussion

As evident from Fig. 4.1 (a), there are several issues with the results obtained by the method described above. Introducing the Hanning window function has clearly improved the contrast

as seen in Fig. 4.1 (b). Since using a window function already reduces the scalloping loss, zero padding, as shown in Fig. 4.1 (c), does not affect the end result significantly in this case. However, it is still useful in improving the computational performance as described later in this section. Sinc excitation signal controls aliasing. This is better demonstrated in the case of a nano–wire, as described later in this chapter, where the range of observation (in frequency and wavevector domains) is higher than that in Fig. 4.1 (d). We now enumerate the major issues and establish some techniques to overcome them. Figure 4.2 depicts this entire procedure schematically.

High resolving powers in both frequency and wavevector domains are often desirable for studying the fine structures of the dispersion curves. The difference between two consecutive values of frequency (resolution in frequency) equals $1/t$, where t is the duration of observation, and resolution in the wavevector domain equals $1/l$, where l is the length of the sample. If a dynamic phenomenon finishes too rapidly, possibly due to very high damping, it would be impossible to have a good frequency resolution. Similarly, if the size of the magnetic medium is very small then we will obtain bad resolution in the wavevector domain. Resolving power in frequency and wavevector domains can, respectively, be improved by running the dynamics for a longer duration and by using longer samples in the direction of SW propagation.

Since we deal with the LLG equation within a continuum micromagnetic framework, phenomena associated with time–scale faster than 1 ps and length scale below 1 nm are beyond the scope of this framework. This gives upper bounds (Nyquist frequency) of range in both frequency and wavevector domains as 500 GHz and 5×10^8 m^{-1} (or 3.141 rad/nm), respectively. Higher rates cost more memory for the same desired resolution. Unless necessary, these rates may be kept as low as possible. For exchange interaction to be effective, the size of the rectangular cuboid should be less than the exchange length of the magnetic material. The rate of sampling of magnetization in time should be high enough to capture the precessional motion correctly. Hence, it should not be less than one 'snapshot' per 10 ps in most cases. Fourier expansion for the N element sequence x_n may be written as

$$\tilde{X}_k = \sum_{n=0}^{N-1} x_n \mathrm{e}^{\frac{-2\pi i k n}{N}}. \tag{4.1}$$

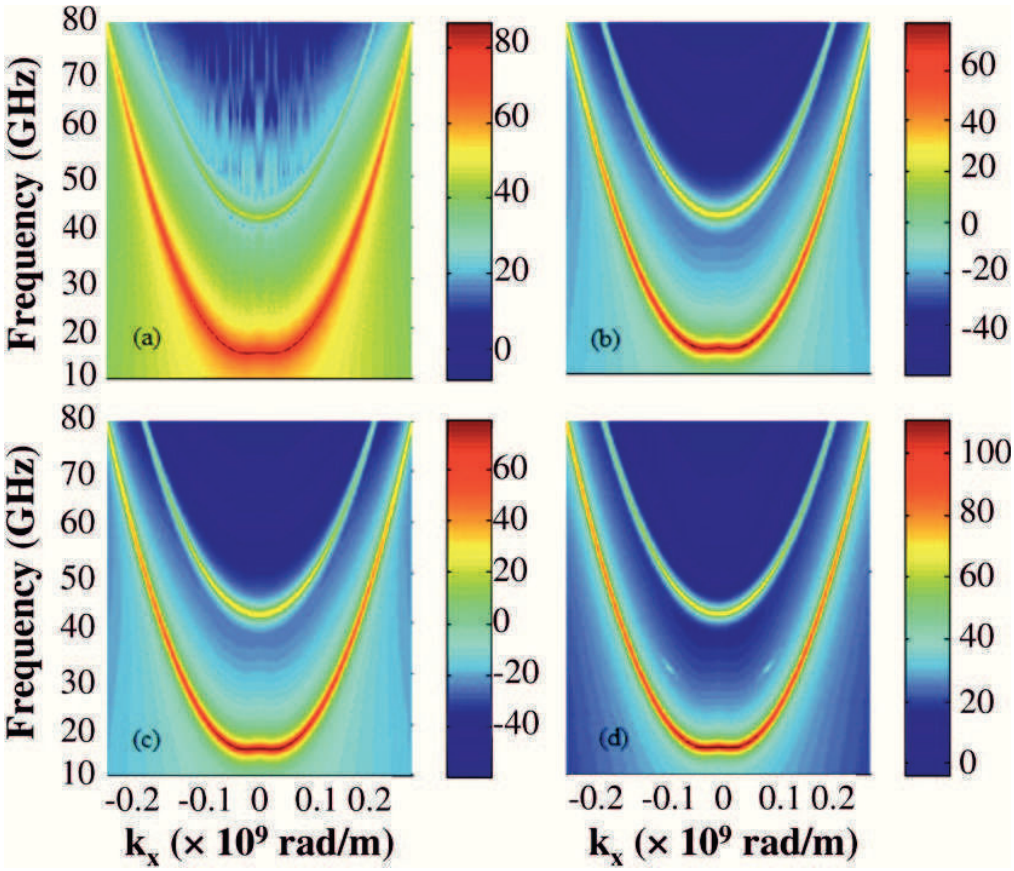

Figure 4.1.: Dispersion along a 5 μm long and 30 nm wide permalloy waveguide with thickness = 10 nm. Bias field $\mu_0 H_{\text{bias}} = 0.05$ T is applied along the length of the waveguide. The dispersion in (a) uses a rectangular window; (b) introduces a Hanning window; (c) adds zero padding and (d) uses a sinc excitation signal as opposed to a Gaussian excitation signal used in (a)-(c). Source: Ref. 262.

For a propagating wave $\tilde{X}_0$ may be ignored as it represents the amplitude of a wave with no frequency (or no wavevector depending upon the dimension used for the Fourier expansion). Ideally $\tilde{X}_0$ should be zero for a propagating wave, but often, in the case of a DFT, it has a finite value due to the lack of resolving power and aliasing. Moreover, the initial magnetization distribution of a magnetic medium may contain some demagnetized regions. High bias fields may be used to minimize these regions. Furthermore, for the purpose of dispersion analysis, the initial magnetization state should be subtracted from the entire time domain response. This subtraction makes it easier to visualize the propagation of spin waves but it will not affect the resultant dispersion curves.

Spectral leakage[263] is another issue associated with DFT, which needs to be taken care of. If power is being delivered at a certain frequency (and wavevector) and that frequency

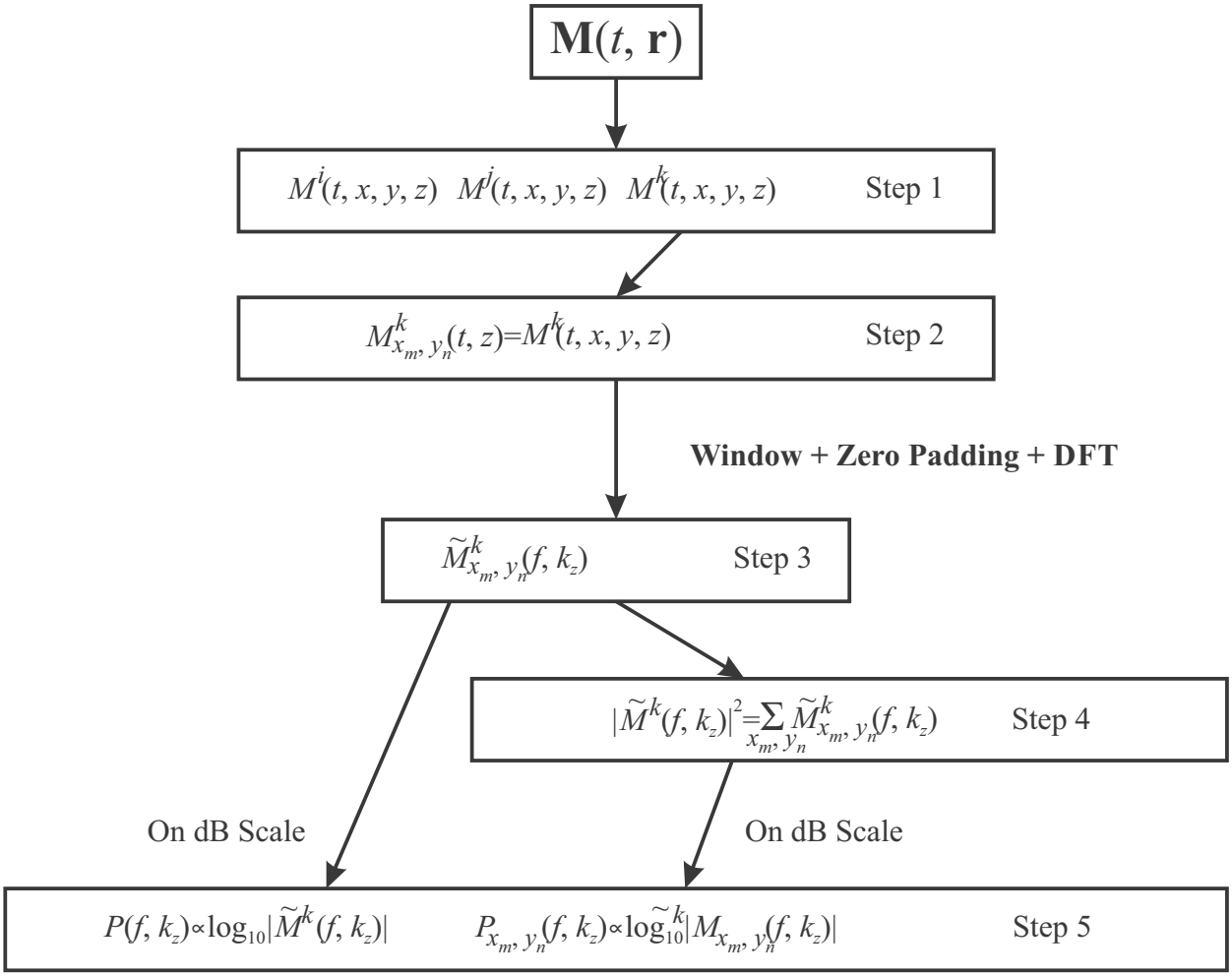

Figure 4.2.: Representation of steps involved in obtaining the dispersion curve for SWs in given magnetic objects. Source: Ref. 262.

(or wavevector) value is missing on the DFT output scale, that power is represented by amplitudes over the entire spectrum. These amplitudes are proportional to a sinc function, sinc(Dn) whose parameter Dn is the difference in number of cycles in time (or space) domain and number of sampling points (in the same dimension). The effect of spectral leakage becomes especially evident when power is represented on a proportional decibel scale. This can be controlled using a window function. Apart from controlling spectral leakage, most window functions help in mitigating aliasing. A 2D window function is needed for a 2D DFT. Two 1D window functions (one for each dimension) are multiplied for this purpose.

A common side effect of using a window function is the broadening of the central peak. Several window functions were compared based on this criterion. A 5 μm long 1D Py

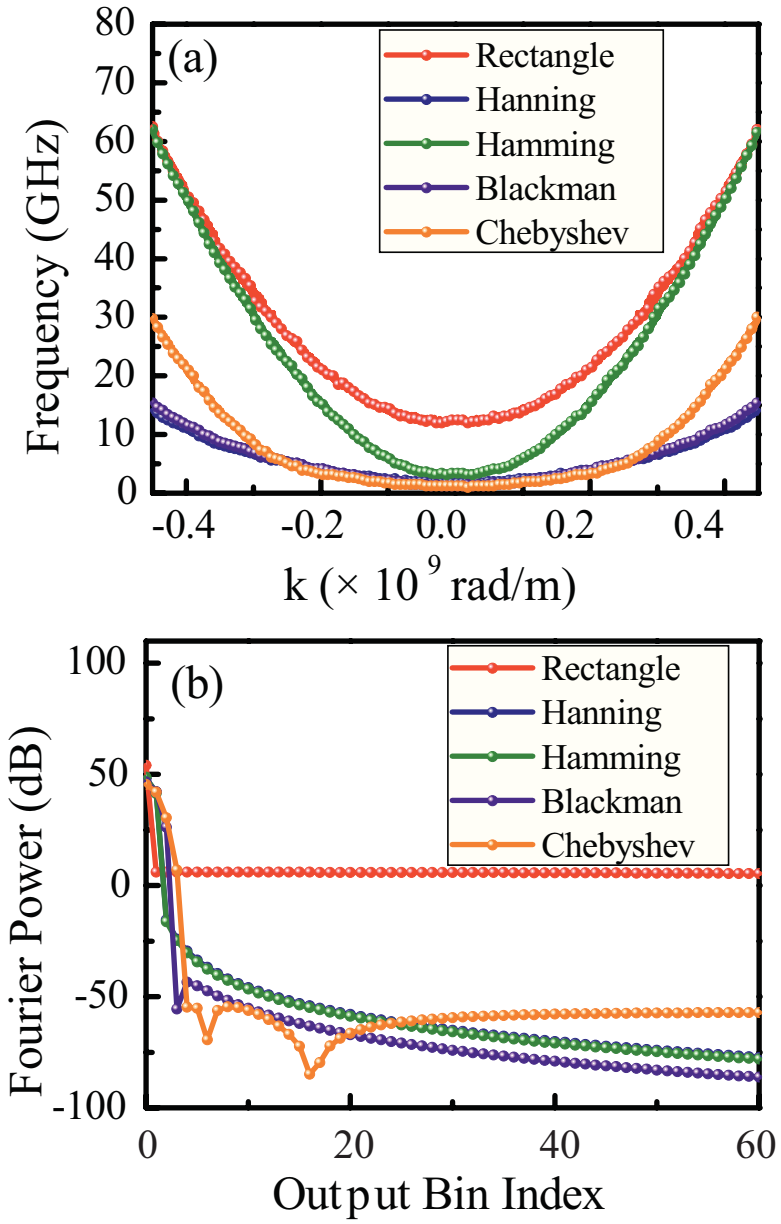

Figure 4.3.: (a) Comparison of mode widths for some window functions. A loss of power of 100 dB for a given value of wavevector was considered as mode cut-off limit. (b) Form of some window functions in frequency domain. As designed, the Chebyshev window maintains a main lobe to side lobe difference of 100 dB here. This is why a very high cut-off value of 100 dB is used in (a). This high cut-off value has led to high numerical mode widths. With good colour contrast visually discernable widths are much lower. Source: Ref. 262.

nanowire with a square cross section of side 9 nm was used for this purpose. Figure 4.3 (a) shows a plot of this width in frequency domain as a function of the wavevector for a few of these window functions. Another way of comparison between window functions is to

compare the difference between the main lobe and side lobes as a function of their position, as shown in Fig. 4.3 (b). For the Chebyshev window this difference can be better controlled. However, when this window is used, a higher difference results in further broadening of the central lobe. This broadening is especially pronounced for a low resolving power. Also, a higher assigned difference in frequency (or wavevector) domain causes a spike at both ends of this window.[264] This should not be a problem if the values of magnetization component under consideration at the beginning and end of simulation have near zero values. Hence, the Chebyshev window is found to be very useful when the numbers of sampling points in space and time domains are high and the duration of simulation has allowed damping to decrease the considered magnetization component to zero.

Due to the nature of DFT, amplitudes beyond the Nyquist frequency are represented at false frequency values. One of the ways these amplitudes can be identified is by sampling at different rates and checking whether they have changed their positions on the axis. Another way to avoid this problem is to ensure that the excitation signal does not supply any power beyond a certain frequency (which is lower than the Nyquist frequency). This can be done by using a signal which varies as a sinc function in both space and time domains (as Fourier transform of a sinc is a rectangle function). In the case of a magnonic crystal (e.g. a 2D array of dots), the sinc signal in space acts upon regions of finite and zero saturation magnetization. A sinc signal should still be considered if the effect of aliasing in the wavevector domain is too pronounced (for example, due to a low number of sampling points in space). A localized excitation signal may be used otherwise. This use can also be mandated by problem design. The resultant aliasing can then be controlled by sampling the magnetization at different spatial frequencies and identifying the amplitudes, which have moved on the wavevector axis.

Data sampled over a finite interval of space or time effectively uses a rectangular window function. This causes a drop in power from one frequency (or wavevector) value to the next. This is termed as scalloping loss. This loss can be reduced by the use of a non-rectangular window. For example, the scalloping loss, from lobe centre to half-way down the lobe centre, for a Hanning window is 1.45 dB, while that for a rectangular window is 4 dB. Scalloping loss can be further reduced by using zero padding[263] which effectively increases the number of

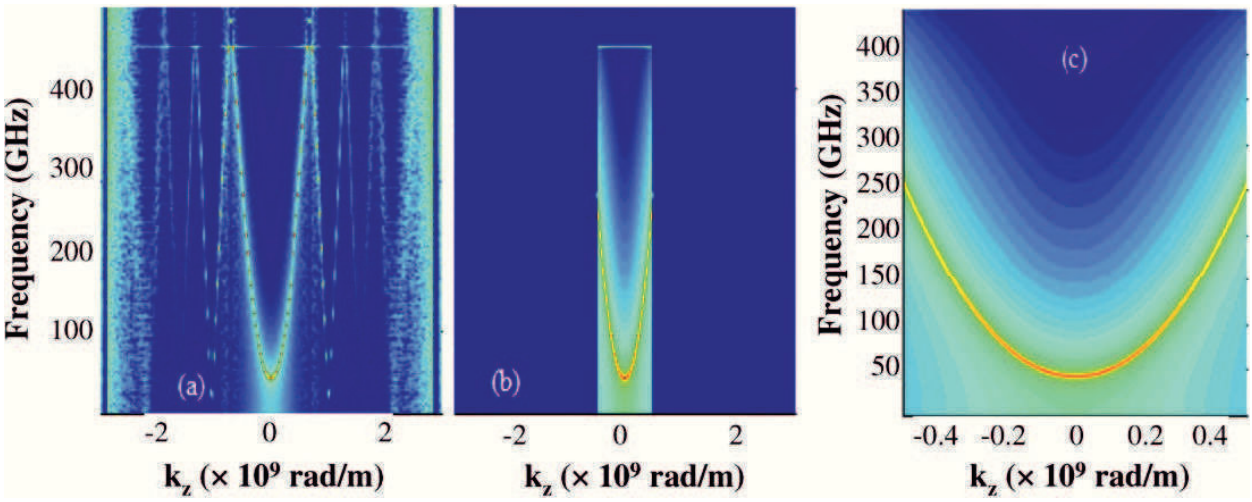

Figure 4.4.: Dispersion in a 1D nanowire of square cross section of side 9 nm with bias field, $\mu_0 H_{\text{bias}} = 1.01$ T: (a) $k_{\text{cut}} = 3$ rad/nm, (b) $k_{\text{cut}} = 0.5$ rad/nm and (c) 'powered' region of dispersion. A linear colour map is used to represent power from 400 to -200 dB. Source: Ref. 262.

output targets (or 'bins') on the frequency (or wavevector) axis. Zero padding can also take advantage of some fast Fourier transform (FFT) algorithms[261,265] by ensuring that the length of data is an integral power of a prime number for delivering better computational speed. The window function is applied before zero padding because doing the reverse gives incorrect result as a part of window function would be multiplied by padded zeros. Zero padding does not improve the resolving power in the sense that the width of the mode remains the same on the frequency or wavevector axis. It also consumes memory. Therefore, it may be preferable to wait till the magnetization values are damped naturally to zero, rather than to artificially pad the data with zeroes, as waiting would also increase the resolving power in the frequency domain without consuming any extra memory which is not already required for zero padding.

Figure 4.4 shows the dispersion of SWs in a 5 μm long 1D nanowire with a square cross section of edge 9 nm. Excitation signal is proportional to $\sin(2\pi f_{\text{cut}} t') / (2\pi f_{\text{cut}} t')$. Here t' represents time and f_{cut} is the parametric frequency of the signal, beyond which it carries no power. A similar cut-off value, say k_{cut}, can be set in the wavevector domain by making the signal proportional to $\sin(2\pi k_{\text{cut}} x) / (2\pi k_{\text{cut}} x)$. f_{cut} and k_{cut} cannot be more than the Nyquist frequency (or wavevector) values in their respective domains. For the purpose of simulation, material parameters of Py were used along with a cell size of 1 nm. Figure 4.4 (a) shows the dispersion when a signal with $f_{\text{cut}} = 450$ GHz and $k_{\text{cut}} = 3$ rad/nm was

used. Figure 4.4 (b) was produced with $k_{\text{cut}} = 0.5$ rad/nm. A sudden drop in power beyond the cut-off values may be noted. Figure 4.4 (c) shows this 'powered' region of dispersion, which has a much better clarity and sharper width as opposed to what is observed in Fig. 4.4 (a).

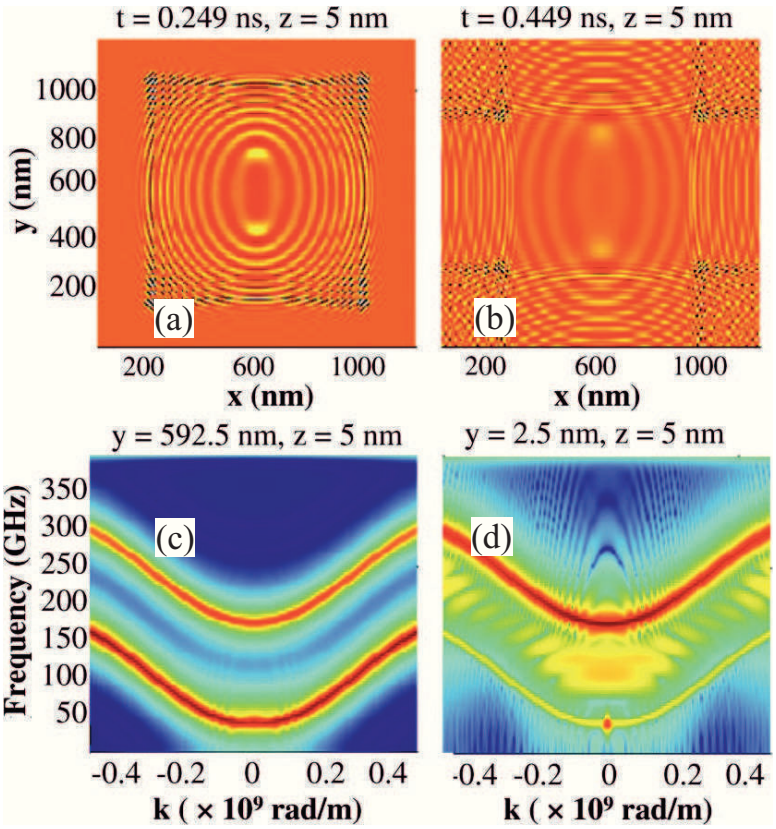

Figure 4.5.: Spin wave propagation in a confined Py thin film element of dimensions 1.2 μm × 1.2 μm × 10 nm at (a) $t = 249$ ps and (b) $t = 449$ ps for $\mu_0 H_{\text{bias}} = 1.01$ T applied along the horizontal edge of the Py element. Dispersion curves (c) along the horizontal edge ($y = 2.5$ nm) and (d) at the centre ($y = 592.5$ nm) of the Py element. Source: Ref. 262.

Figures 4.5 (a) and (b) show the snapshots of the SWs with time in a confined Py thin film element of dimensions 1.2 μm × 1.2 μm × 10 nm. A bias field $\mu_0 H_{\text{bias}} = 1.01$ T was applied parallel to the horizontal edge of the element to saturate the magnetization along the direction. Figures 4.5 (c) and (d), respectively, show the dispersion of SWs along the centre ($y = 592.5$ nm) and along the edge ($y = 2.5$ nm) of this element. The dynamics is excited by a sinc signal in the time domain, which is spatially localized at the centre of the element so that the SWs can propagate uniformly within the $x - y$ plane. Two prominent dispersion

curves are observed in the former case, while a single curve is prominent in the latter. The lowest branch corresponds to the uniform magnetization dynamics ($n = 0$) across the width of the magnetic element while the upper one corresponds to the quantization ($n = 1$ or half-wavelength) across the width of the element. Due to the dynamic boundary conditions[255] the lowest branch is barely excited when we consider the direction along the horizontal edge of the element as one can see from Fig. 4.5 (d). The spin wave wave-front takes an elliptical shape due to the dependence of group velocity on the angle between wavevector and the direction of static magnetization (bias magnetic field).

Propagating SWs in continuous magnetic media show continuous dispersion of frequency as a function of wavevector. Formation of periodic modulation of the magnetic medium results in opening of band gaps at the Brillouin zone (BZ) boundary. Magnetic antidot lattices serve the purpose due to the creation of discontinuity at the magnetic material and air interface or at a different magnetic material filling the antidots.[55,56,105,242,266,267] In the following, we apply the described numerical techniques to calculate the dispersion curves of magnonic crystals made up of 1D and 2D arrangements of magnetic antidots in permalloy thin films. Cuboidal cells of edge 3 nm are used during the simulation for magnonic crystals examined in this chapter. Figures 4.6 (a) and (b) show the static magnetic configurations of a 1D array of square antidots with edge and separation of 12 nm carved into a permalloy strip with width = 24 nm, length = 2.4 μm and thickness = 3 nm. A bias magnetic field ($\mu_0 H_{\text{bias}}$) of 1.01 T was applied (a) along the length and (b) across the width of the sample so that the dispersions of SWs in the backward volume magnetostatic spin-wave (BV) configuration[268] and magnetostatic surface wave or Damon–Eshbach (DE) configuration[269] are obtained. Figures 4.6 (c) through (d) show the computed dispersion curves of SWs with wavevector for this sample. The confinement along the width of the permalloy strip, on which the square antidots are imprinted, will cause a number of symmetric and anti-symmetric modes for all allowed values of the wavevectors. The spatial modulation of magnetic parameters due to the introduction of the square antidots introduces a band spectrum and we investigate the effect of that on the symmetric and anti-symmetric modes in the resultant dispersion curves.

In Fig. 4.6 (c), we show the excitation of only the symmetric modes in the 1D array of antidots, while in Fig. 4.6 (d) both symmetric and anti-symmetric modes are excited

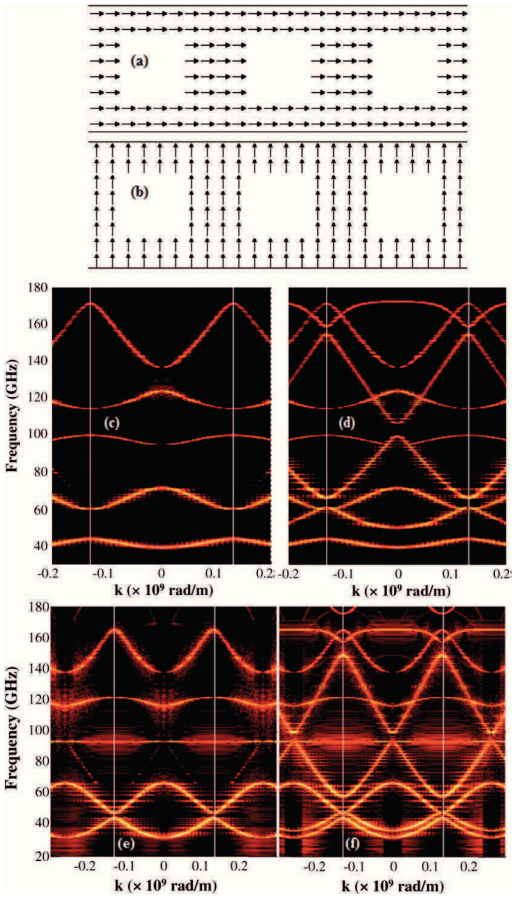

Figure 4.6.: Static magnetic configurations (in-plane) of the central portion of the simulated sample with the bias field, $\mu_0 H_{\text{bias}} = 1.01$ T, applied (a) along the length and (b) across the width of the sample. The sample is a permalloy strip with width = 24 nm, length = 2.4 μm, thickness = 3 nm and with 1D array of square antidots carved in it. The antidots are square in shape and have both width and separation of 12 nm. Simulation of SW dispersion of (b) symmetric mode only and (c) both symmetric and anti-symmetric modes for the BV configuration. (e) Symmetric only and (f) both symmetric and anti-symmetric modes in DE configuration are also shown. The vertical white lines mark the boundaries of the BZ which has a total width of 0.2618 rad/nm. Source: Ref. 262.

in the same sample. The anti-symmetric modes can be excited if the applied signal is anti-symmetric across the width of the crystal. The anti-symmetric modes do not interact with symmetric modes[270,271] and four new branches are created in the observed frequency range of dispersion curves. We have further calculated the dispersion of a bi-component medium to demonstrate the effects of variation of the periodic potential in the magnonic medium as a result of the inclusion of a second ferromagnetic medium within the antidot regions. Figure 4.7 (a) and (b) show the static magnetic configurations of a bi-component

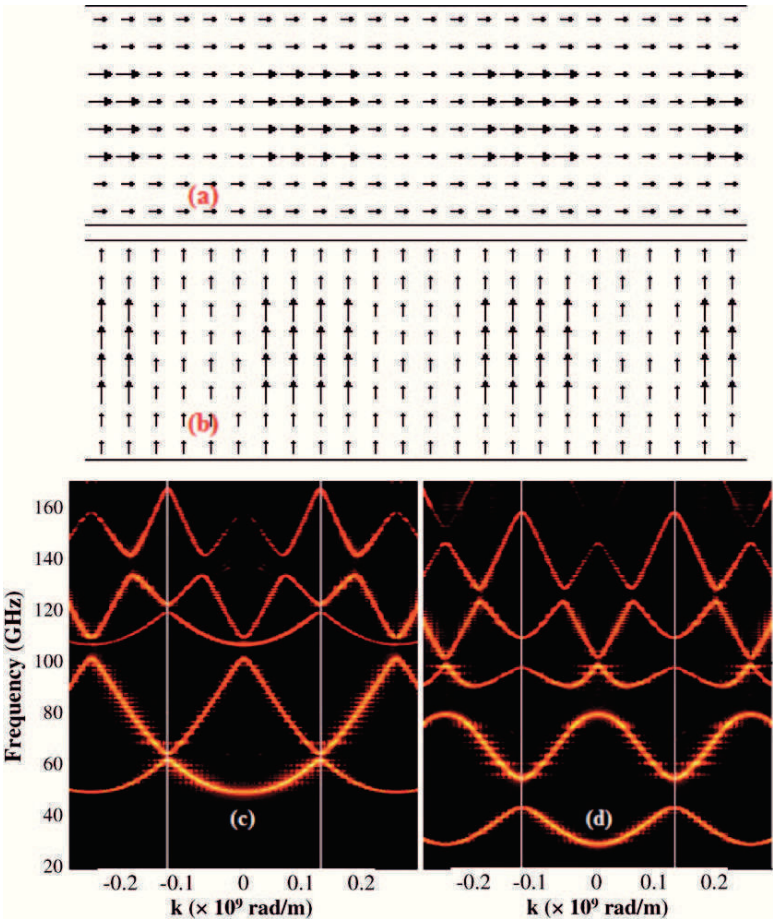

Figure 4.7.: Static magnetic configurations (in-plane) of the central portion of the simulated sample with the bias field, $\mu_0 H_{\text{bias}} = 1.01$ T, applied (a) along the length and (b) across the width of the sample. The sample is a bi-component medium with 1D array of square-shaped Co inclusions in a permalloy strip with width = 24 nm, length = 2.4 μm and thickness = 3 nm. The sides of Co squares are 12 nm and the edge-to-edge separations between the two squares is 12 nm. Simulated dispersion of symmetric modes in the above samples with the bias field applied (c) along the length and (d) across the width of the sample. The vertical white lines mark the boundaries of the BZ which has a total width of 0.2618 rad/nm. Source: Ref. 262.

medium with 1D array of square-shaped Co ($K = 520 \times 10^3$ J/m^3, $M_s = 1400 \times 10^3$ A/m, $A = 30 \times 10^{-12}$ J/m, $|\bar{\gamma}| = 2.21 \times 10^5$ rad s^{-1} T^{-1}) inclusions in a permalloy strip with width = 24 nm, length = 2.4 μm and thickness = 3 nm. The edge and separation of Co squares are 12 nm. The static magnetic field $\mu_0 H_{\text{bias}} = 1.01$ T is applied (a) along the length and (b) across the width of the simulated samples. Figures 4.7 (c) and (d) show the dispersion of symmetric modes in this medium for the bias field geometries of (a) and (b), respectively.

The band gaps in Fig. 4.7 (c) are considerably reduced as compared with those in Fig. 4.6 (c) due to the reduction in the difference between the values of the magnetic parameters in the bi-component medium as compared with the unfilled antidots. Similarly, with the exception of first band gap the others are significantly smaller in Fig. 4.7 (d) when compared with the modes in Fig. 4.6 (e). For the long permalloy strip the shape anisotropy is along the length of the sample and hence the application of bias field across the width causes a reduction in the effective field and consequently a downward shift in the overall frequencies in the dispersion curves is observed. In the DE (Fig. 4.7 (d)) geometry the curvature of dispersion (and the corresponding group velocities) and band gaps are significantly different from that in the BV geometry (Fig. 4.7 (c)) due to the difference in the initial magnetization state as a result of the competition between the Zeeman, demagnetization and magnetocrystalline anisotropy energies in two different materials in the bi-component magnonic crystal.

We now extend our calculation of dispersion curves to three rows of 1D arrays of antidots (quasi-2D antidot arrays). The introduction of quasi-periodicity across the width of the magnonic crystal and the dipolar interactions between the different rows of antidot arrays cause significant modifications in the dispersion curves. In Fig. 4.8, we show the dispersion curves of the quasi-2D antidot arrays with length = 2.4 μm, width = 72 nm and thickness = 3 nm. The bias field $\mu_0 H_{\text{bias}} = 1.01$ T was applied along the (a) length and (b) across the width of the magnonic crystal. A comparison of Figs. 4.6 (c) and (e) with Figs. 4.8(c) and (d) reveals that the latter show band intersection and very rich dispersion patterns. The two lowest frequency branches of dispersion in Fig. 4.8 (c) have the same curvatures, signifying the same group velocity but different phase velocities. However, the group velocities of the two lowest dispersion branches in Fig. 4.8 (d) are different. The higher frequency branch also has a lower spectral power.

Figures. 4.9 (b) and (c) show the spatial distribution of the power and phase of magnetization for specific frequency values on different branches of the dispersion curves for the 1D array of antidots as shown by the white dotted lines in Fig. 4.9 (a). The power and phase distribution information are obtained by fixing one of the spatial co-ordinates in $M^k(t, x, y, z)$ and performing a DFT with respect to time domain. The bias field was applied along the length of the 1D antidot array. The mode corresponding to $f = 39.99$

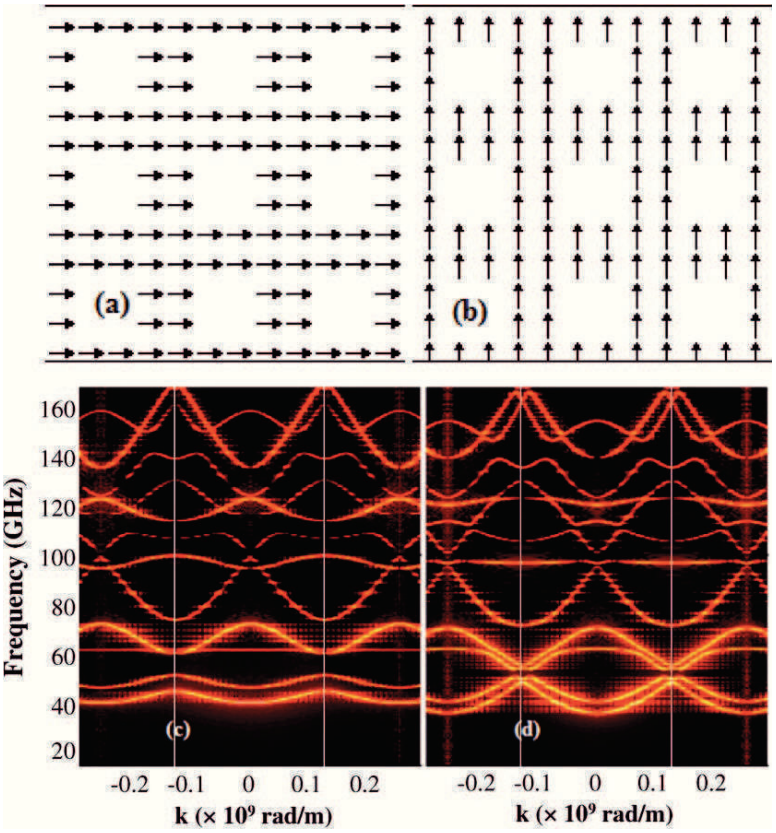

Figure 4.8.: Static magnetic configurations (in-plane) of the central portion of the simulated sample with the bias field, $\mu_0 H_{\text{bias}} = 1.01$ T, applied (a) along the length and (b) across the width of the sample. The sample is a permalloy strip with width = 72 nm, length = 2.4 μm, thickness = 3 nm and with three rows of 1D array of square antidots imprinted in it. The antidots are square in shape and have both width and separation of 12 nm. Simulated dispersion of symmetric modes in the above samples with the bias field applied (c) along the length and (d) across the width of the sample. Source: Ref. 262.

GHz (Fig. 4.9 (b)) belongs to the lowest band (band index $n = 1$) and propagates with uniform phase along the length of the array. The mode at $f = 60.84$ GHz (Fig. 4.9 (c)) belongs to the band with $n = 2$ and propagates with regions around alternating antidots oscillating out-of-phase. Figure 4.10 shows the spatial distribution of power and phase of the quasi-2D array of antidots. The four branches of dispersion are highlighted in Fig. 4.10 (a). The power and phase distributions of the lowest ($n = 1$) and highest branches ($n = 4$) of the quasi-2D array are similar to the $n = 1$ and $n = 2$ bands, respectively, for the 1D case, as shown in Figs. 4.10 (b) and (e). The power and phase distributions for the two middle branches ($n = 2$ and 3) are shown near the BZ boundary where dispersion becomes flat

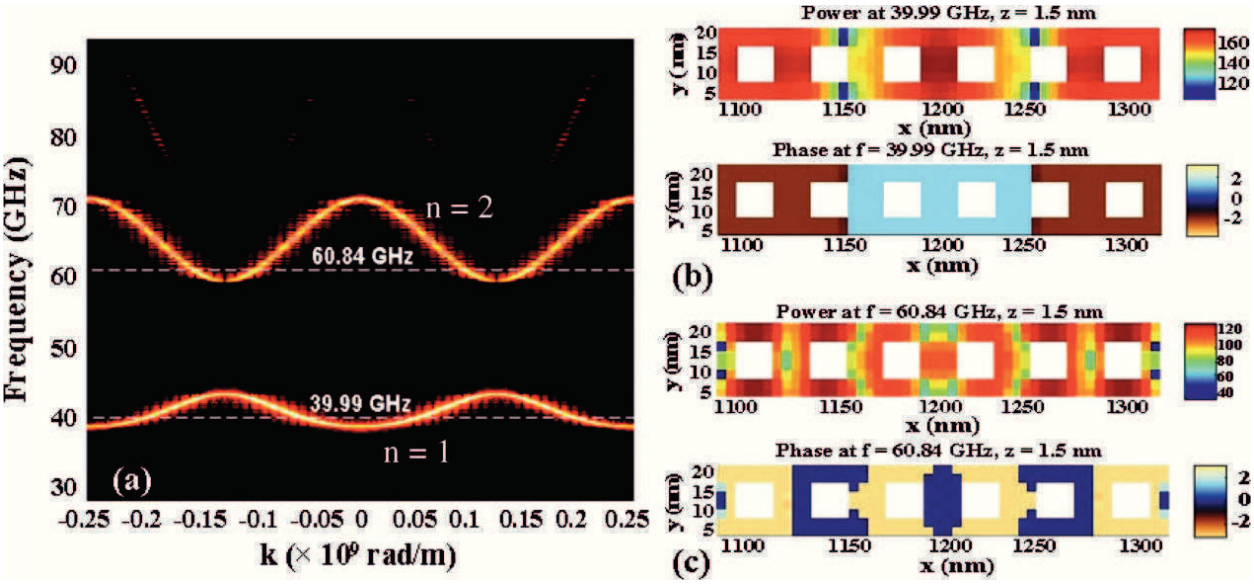

Figure 4.9.: (a) Selected part of the dispersion image, as shown in Fig. 4.6 (c), showing the frequencies at which the spatial distribution of power and phase of SWs is shown. The power and phase corresponding to modes at (b) $f = 39.99$ GHz and (c) $f = 60.84$ GHz. The excitation was done at the centre of the array ($x = 1200$ nm) and only a small part of the array is shown for visual clarity. A bias field of 1.01 T is applied along the length of the array. Source: Ref. 262.

and the group velocity close to zero. The power and amplitude distributions are distinctly different from the propagating modes, as shown in Figs. 4.10 (b) and (e).

4.3. Conclusion

In this chapter, we have reported a technique, which can be employed to obtain dispersion of SWs in different kinds of magnetic micro- and nanostructures with high numerical contrast and clarity. The use of DFT windows and sinc functions to control the spectral leakage and aliasing is highlighted. The examples of dispersion calculations for magnetic nanostripes, magnetic nanowires and confined thin film elements are shown to validate the method. We then employed the described technique to calculate the dispersion curves on 1D and quasi-2D magnonic crystals based upon magnetic antidot arrays in BV and DE configurations. The effect of inclusion of a second magnetic component in 1D arrays of antidot lattice on the dispersion curves is also demonstrated. The dispersion curves obtained using this technique can be used in conjunction with analytical modelling to form guiding principles

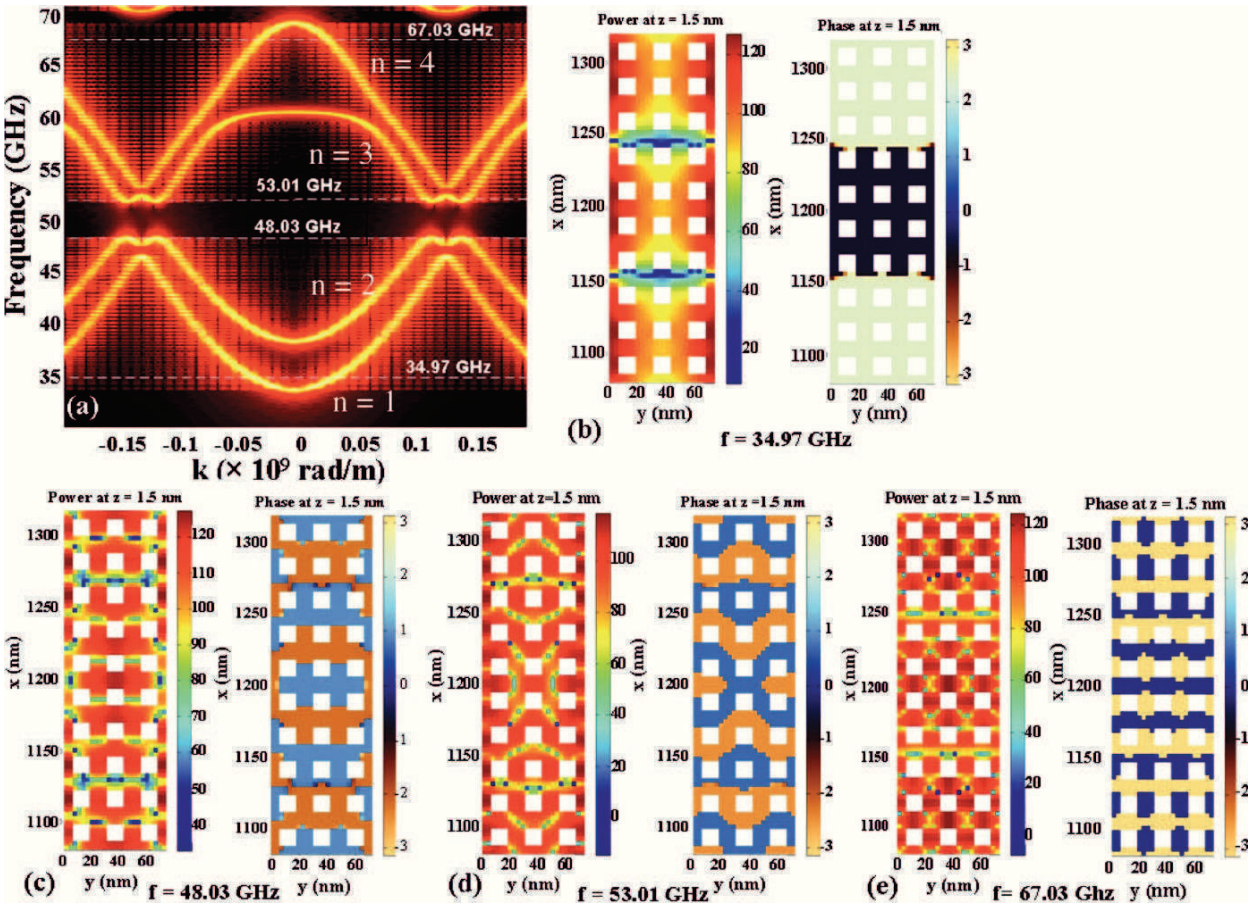

Figure 4.10.: (a) Selected part of the dispersion image, as shown in Fig. 4.8 (d), showing the frequencies at which the spatial distribution of power and phase of SWs is shown. The power and phase corresponding to modes at (b) $f = 34.97$ GHz, (c) $f = 48.03$ GHz, (d) $f = 53.01$ GHz and (e) $f = 67.03$ GHz. The excitation was done at the centre of the array ($x = 1200$ nm) and only a small part of the array is shown for visual clarity. A bias field of 1.01 T is applied along the width of the array. Source: Ref. 262.

in investigating and controlling the details of magnonic band structures in different kinds of magnonic crystals.

5. Free and Pinned Boundary Condition in a Magnonic Antidot Waveguide

*In this chapter we focus on the boundary conditions imposed on the dynamic components of the magnetization vector and their effect on the spectrum of SWs in magnonic waveguides. These boundary conditions are additional to the electromagnetic ones, which describe the degree of freedom of the magnetization vector at the edges of the ferromagnetic material. The effect of the boundary conditions on the spectrum of SWs in uniform thin films has been investigated broadly.[215,272,273] However, no such research has been conducted so far in antidot lattices, in which the interfaces with air play an important role in the formation of magnonic bands.[274,275] Only free boundary conditions are assumed in the vast majority of papers dealing with periodic waveguides. Thus, there is a gap in the research, which we attempt to fill in with this study.

In this chapter we study the magnonic band structure in waveguides, a basic element of any magnonic device.[93,95] Waveguides for exchange SWs have been recently investigated theoretically with the use of micromagnetic simulations;[84,259,267] periodic waveguides have been demonstrated to have filter properties due to the folding effect and the opening of magnonic gaps in the SW spectrum.[5,94] Here we investigate a periodically modulated waveguide with a series of antidots in the centre. Aware of the fact that the periodicity of the waveguide can be realized in many different ways—by width or shape corrugation, or by applying a specific magnetic field[5,94,267] — we are confident that the fundamental features of this quasi-1D pe-

*This chapter is based upon Kłos *et al. Phys. Rev. B* **86**, 184433 (2012).

riodic system are conserved and the conclusions drawn for the model considered will be of general nature.

We show that a magnetization pinning introduced at the edges of the waveguide can significantly change its SW spectrum. To cross–check our results we perform calculations based on different methods: micromagnetic simulations and the plane wave method (PWM). These techniques have already been successfully used for the interpretation of experimental data obtained for systems of various geometry in the formulation used here.

We show that the pinning is intrinsic for PWM at the interface of magnetic/nonmagnetic material. For micromagnetic calculations the magnetic moments are not forced to be pinned by default.We introduce pinning by placing on the interface a thin layer for which the dynamics of magnetization is frozen (with the amplitude of precession set to zero).

The chapter is organized as follows. In Sec. 5.1 we describe the structure under investigation and the calculation methods used. In Sec. 5.2 we explain the effects that the boundary conditions imposed on the dynamic magnetization components at the edges of the ferromagnetic material have on the magnonic spectrum. Our results are summarized in the closing Sec. 5.3.

5.1. Waveguide Structure and the Calculation Methods

The magnonic waveguide under consideration is shown in Fig. 5.1. It has the form of a thin and infinitely long permalloy stripe with a single row of square holes disposed periodically along the central line. A bias magnetic field is applied along the stripe and assumed to be strong enough ($H_{\text{bias}} = 1$ T) to saturate the sample. The material parameters of Py were used in all calculations.

We use three methods of calculating the dispersion of SWs in the permalloy MAW: the finite difference method, the finite element method and the PWM, with OOMMF,[250] Nmag[276] and a home-developed Fortran code, respectively.

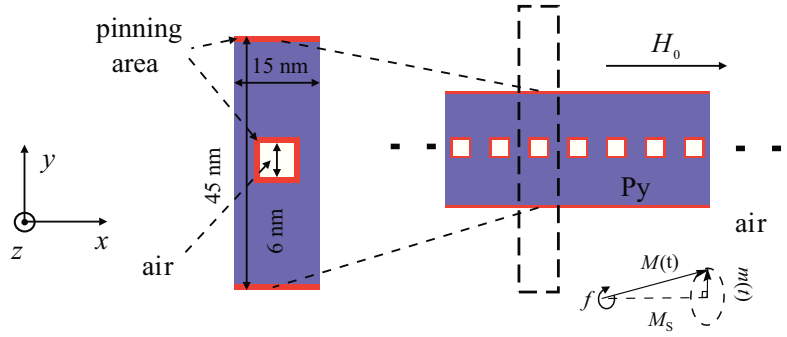

Figure 5.1.: Magnonic antidot waveguide under investigation: a 3 nm thick and 45 nm wide infinite Py stripe with a periodic series of 6 nm × 6 nm square antidots disposed centrally along the x-axis with a period of $a = 15$ nm. Bias magnetic field $\mu_0 H_{\text{bias}} = 1.01$ T is oriented along the $x-$ axis. The 1.5 nm wide red lines at the Py/air interfaces mark the regions in which pinning is assumed in the OOMMF calculations. The dashed box shows the supercell size used in PWM calculations. Source: Ref. 213.

5.1.1. Micromagnetic Simulation

The micromagnetic simulations (OOMMF, Nmag) are performed in two steps. The magnetic ground state is obtained first. We let the magnetization evolve in the presence of damping to reach the static equilibrium orientation. In the next step, with damping neglected ($\alpha = 0$), a small pulse of magnetic field was applied as given by Eq. (5.1) with a small amplitude (which guarantees the linear regime of spin dynamics). After recording the magnetization in each mesh point for each time step, Fourier transformation is performed in the time and space domains to obtain the SW dispersion, i.e., the wave-vector dependence of the SW frequency.[260,262]

The excitation signal used to study the dynamics is of the form

$$h_z(t,x,y) = h_z^0 \operatorname{sinc}\left\{2\pi f_{\text{cut}}(t-t_0)\right\} \times \operatorname{sinc}\left\{k_{\text{cut}}\left(x - \frac{1}{2}x_{\max}\right)\right\} \times \sum_{n=1}^{N} \sin\left(n\pi \frac{y}{y_{\max}}\right), \quad (5.1)$$

where the sinc function is taken in the form $\operatorname{sinc}(\theta) = \sin(\theta)/\theta$. The strength of the signal is defined by $\mu_0 h_z^0 = 5$ mT. The parameter $f_{\text{cut}} = 490$ GHz sets the upper limit of frequencies of SWs excited by the sinc like pulse. An offset $t_0 = 50$ ps was given to avoid the high spikes close to the f_{cut} in the frequency domain of the signal. The k_{cut} is a wave number cut–off defined later. The symbols $x_{\max} = 3$ μm and $y_{\max} = 15$ nm denote the sizes of the sample.

The summation in Eq. (5.1) was done for $N = 30$ subdivisions.

The benefits for using such a signal and the procedure to obtain the desired dispersion relation are described in Sec. 4.2. In the case of an antidot lattice the effect of convolution of the periodic array of holes will be observed in the wave-vector domain. A wavevector cut–off k_{cut}, which is an odd multiple of half the Brillouin zone (BZ) length (here $3\pi/a$), may be used to mitigate this effect. Also, in order to generate both symmetric and antisymmetric wave fronts a suitable dependence (which, here, is a sum of symmetric and antisymmetric excitations along the width) on y has been applied to the signal.

The OOMMF simulations are performed with 1D periodic boundary conditions[243] applied along the $x-$ axis. A 1.5 nm mesh is used in these simulations. The correctness of the assumed discretization was verified by comparing the results with those of simulations using a 0.5 nm mesh.

The micromagnetic simulations do not assume by default any torque acting on the external interfaces (numerical calculations are limited to the magnetic medium only). Therefore, the spins are precessing freely on the systems boundaries with dipolar effects taken fully into account.

We can force the pinning in all mesh cells located on the interfaces between magnetic and non-magnetic materials (see the red-coloured pinning area in Fig. 5.1). It can be done by freezing the magnetization dynamics $\frac{\partial}{\partial t}\mathbf{M}(\mathbf{r}, t) = 0$ with initial conditions $M_z(\mathbf{r}, t = 0) = 0$ and $M_y(r, t = 0) = 0$ at the beginning of the second stage of calculation when the system managed to reach the ground state. From the LLG equation, it follows that the initial condition for z and y components of magnetization will be sustained, if the conditions $M_y(r, t = 0) = 0$ and $M_z(r, t = 0) = 0$ are set in the pinned layer. We checked that for the strong external field that we used ($\mu_0 H_{\mathrm{bias}} = 1.01$ T) the magnetization in the ground state is uniform and parallel to the direction of $\mathbf{H}_{\mathrm{bias}}$ even in the vicinity of the interfaces.

Because of the use of the finite difference method in OOMMF simulations, space is discretized into small cuboids. Nmag uses the finite element method, in which, in contrast, the modelled object is discretized on a tetrahedral mesh. In general, this allows for better modelling of arbitrarily shaped objects, but for the considered antidot waveguide, this does not provide an advantage because our simulating object consists basically of orthogonal

walls. For the mesh creation, we use the open source generator "NETGEN". When creating the unstructured mesh, care must be taken in providing the software with a proper value of the maximum-mesh size parameter. Only when this value is small enough is it possible to calculate the exchange and magnetostatic fields with reasonable accuracy. Unfortunately, as the maximum mesh- size parameter decreases, the number of tetrahedral elements increases, making the computing time and memory demands increase as well. One way to partially overcome this problem is to use an adaptive mesh with the smaller cell sizes in the vicinity of antidot edges. We must select a value below the exchange length, which in the case of permalloy is 5.1 nm. Therefore, we selected a maximum size of 4.5 nm for the edge length of all tetrahedra to achieve accurate results. However, the average edge length was about 2.5 nm with standard deviation equal to 0.6 nm. It was decided not to use periodic boundary conditions in Nmag simulations but instead use a finite segment of this waveguide of length 1.8 micrometer, containing 120 repetitions of the unit cell. The waveguide is surrounded by non–magnetic material, which does not have to be discretized. This is because Nmag used a hybrid finite elements/boundary elements method to calculate the magnetostatic contribution.

The steps to obtain the dispersion relation are the same as in OOMMF. As a first step, a high value of the Gilbert damping parameter is chosen and the system is evolved under the external field to find the energy-minimizing configuration of the system. This state is used as the starting point during the second part. Now damping is neglected and the system is excited with a pulse containing a broad frequency range. Using the Fourier transform, the resonating values of (k, ω) are obtained as local maxima. These values constitute the dispersion diagram.

5.1.2. Plane Wave Method for a Magnonic Antidot Waveguide

PWM has been discussed in some detail in Sec. 3.4. Here we revisit the method while elaborating its application in the case of a 1D MAW. In the PWM, periodic Bloch conditions are applied both along the MAW axis and in the direction perpendicular to this axis. An artificial periodicity in the y direction creates a periodic series of non–interacting copies of the original waveguide — this is the supercell approach.[277] We used the supercell marked

in Fig. 5.1 by dashed line. The assumed periods are 15 nm (antidot period) and 100 nm (artificial supercell) along the x and y axes, respectively.

The antidots and spacer areas were filled with artificial material characterized by a high value of volume anisotropy field and an extremely low value of magnetization saturation that squeezed the magnetization dynamics in this region (effect of the low magnetization saturation) and shifted the frequencies of spurious modes appearing in the results into a very high-frequency range (impact of the high volume anisotropy field). Note that according to the Landau-Lifshitz equation the increase of the effective field in the artificial material (as a result of big volume anisotropy) will also decrease the amplitudes of dynamical magnetization if one wants to keep the SW frequency constant.We have made sure that the assumed 65 nm waveguide spacing is sufficient to neglect the interactions between adjacent copies. We plotted the dispersion relation in the $\Gamma - Y$ direction (i.e., for a propagation direction perpendicular to the waveguide's axis). The branches that we obtained were flat which confirmed the localization of SWs in the Y direction and the lack of crosstalks between adjacent copies of waveguides.We also checked the amplitude of SWs in the spacers separating waveguides, which occurred to be cancelled. The cancelling of spin dynamics in the air gaps (spacers and antidot areas) results in magnetization pinning at the interface with magnetic material. In order to simulate the system of planar geometry with partially pinned magnetization on the interfaces with non–magnetic material one can artificially change the in-plane sizes of the system from R to effective R_{eff} to achieve a non–zero value of dynamical magnetization when the position r coincides with R.[215] We used this procedure to perform PWM calculations in the dipolar-exchange regime for 2D antidot lattices.[57]

We are considering the magnetization dynamics without damping in the linear approximation only. We are assuming that the magnetization precesses around X-axis in a cone with small angle (as it is presented in Fig. 5.1). Under this assumption we can write:

$$\begin{aligned} M_x(\mathbf{r}) &\approx M_s, \\ M_y(\mathbf{r},t) &= m_y(\mathbf{r})e^{i\omega t}, \\ M_z(\mathbf{r},t) &= m_z(\mathbf{r})e^{i\omega t}. \end{aligned} \tag{5.2}$$

The exchange term can be expressed as:[27]

$$\mathbf{H}_{\text{exch}} = \nabla\lambda_{\text{ex}}^2\nabla\mathbf{M}(\mathbf{r},t), \tag{5.3}$$

which directly deviates from the Heisenberg model.[278]

To describe demagnetizing field for periodic slab of finite thickness we used the ideas proposed by Kaczér and Murtinová[279] and then developed in Ref. 280 where each component of (static $\mathbf{H}_{\text{dem}}(\mathbf{r})$ and dynamic $\mathbf{h}_{dm}(\mathbf{r},t)$) demagnetizing field is depending, in general, on the spatial distribution of all component of magnetization. The components of the static and dynamic demagnetizing fields within the linear approximation taken into account are

$$H_{dm,x}(\mathbf{r}) = -\sum_{\mathbf{G}} M_{\text{s}}(\mathbf{G})\left(\frac{G_x}{G}\right)^2(1-C(z,G))\,e^{-i(\mathbf{G}\cdot\mathbf{r}_\parallel)}, \tag{5.4}$$

$$\begin{aligned} h_{dm,z}(\mathbf{r},t) &= \sum_{\mathbf{G}}\Big[-m_z(\mathbf{G})C(z,|\mathbf{G}+\mathbf{k}|) \\ &+ i\,m_y(\mathbf{G})\frac{|k_y+G_y|}{|\mathbf{G}+\mathbf{k}|}S(z,|\mathbf{G}+\mathbf{k}|)\Big]e^{i\omega t}e^{-i((\mathbf{G}+\mathbf{k})\cdot\mathbf{r}_\parallel)}, \end{aligned} \tag{5.5}$$

$$\begin{aligned} h_{dm,x}(\mathbf{r},t) &= \sum_{\mathbf{G}}\Big[-m_y(\mathbf{G})\frac{(k_y+G_y)^2}{|\mathbf{G}+\mathbf{k}|^2}(1-C(z,|\mathbf{G}+\mathbf{k}|)) \\ &+ i\,m_z(\mathbf{G})\frac{|k_y+G_y|}{|\mathbf{G}+\mathbf{k}|}S(z,|\mathbf{G}+\mathbf{k}|)\Big]e^{i\omega t}e^{-i((\mathbf{G}+\mathbf{k})\cdot\mathbf{r}_\parallel)}, \end{aligned} \tag{5.6}$$

where $\mathbf{G}=[G_x,G_y]$ and $\mathbf{r}_\parallel=[x,y]$ are 2D reciprocal lattice vector and position vector in real space. The symbols: $M_{\text{s}}(\mathbf{G})$ and $m_\alpha(\mathbf{G})$ denote the coefficient of Fourier expansion for magnetization saturation $M_{\text{s}}(\mathbf{r}_\parallel)=\sum_{\mathbf{G}}\mathbf{M}(\mathbf{G})e^{-i(\mathbf{G}\cdot\mathbf{r}_\parallel)}$ and periodic part of Bloch functions: $m_\alpha(\mathbf{r}_\parallel)=m_\alpha(\mathbf{G})\sum_{\mathbf{G}}\mathbf{M}(\mathbf{G})e^{-i((\mathbf{G}+\mathbf{k})\cdot\mathbf{r}_\parallel)}$, where $\alpha=y,z$ and $\mathbf{k}$ is a wavevector. The functions $C(z,\kappa)$ and $S(z,\kappa)$ are defined as:

$$C(z,\kappa)=\frac{\sinh(z\kappa)}{\sinh(c\kappa)+\sinh(c\kappa)}, \tag{5.7}$$

$$S(z,\kappa)=\frac{\cosh(z\kappa)}{\sinh(c\kappa)+\sinh(c\kappa)}, \tag{5.8}$$

where $2c$ is the thickness of MAW (in z-direction). The demagnetizing fields do not change a lot across the slab accept the regions in the close vicinity of the external surfaces (note that the structure is uniform in z-direction). Therefore we assumed that all fields: $\mathbf{H}_{\text{dem}}(\mathbf{r}_\parallel)$

and $\mathbf{h}_{dm}(\mathbf{r}_{\parallel}, t)$ are independent on z-coordinate by taking its values form the centre of the slab. This simplification allowed us to consider the system as 2D one.

In the linearisation procedure we took advantage from the assumption: $m_\alpha(\mathbf{r}) \ll M_s, \alpha = y, z$ and dropped all small terms with precession frequency higher than ω. Then after applying the Fourier transformation we were able to convert the linearised differential equations for $m_y(\mathbf{r}), m_z(\mathbf{r})$ into the set of algebraic equation in the form of eigenproblem with $m_y(\mathbf{G}), m_z(\mathbf{G})$ as eigenvectors and ω playing the role of eigenfrequency.

We checked that the sufficient convergence for the presented dispersion plots (Fig. 5.3) is achieved for 11×91 plane waves propagating in x and y direction, respectively (described by different x and y components of reciprocal vectors $\mathbf{G}$). The details of the PWM, its supercell formulation, and the application of this technique are available in the literature.[51,57,277,280]

5.2. The effect of pinning on the magnonic spectrum

Figure 5.2 (a) shows the magnonic band structure obtained in the OOMMF simulations. The SW spectrum is very rich, with a clear evidence of periodicity and folding effects. Three repetitions of the Brillouin zone (BZ), delimited by vertical solid lines, are considered. Free boundary conditions for the dynamic components of the magnetization vector (unpinned magnetization) at the edges of Py were used in these calculations. The lack of pinning is confirmed by the mods profiles (bottom of Fig. 5.2) computed with OOMMF (not shown) and Nmag where the non–zero values of $|m_z|^2$ at the air/Py interfaces are observed. Very similar SW dispersion (Fig. 5.2 (b)) were obtained also in the Nmag simulations. Surprisingly, the results obtained by the PWM are different. The PWM spectra are shown in Fig. 5.3 (red dashed lines). The bands are seen to be shifted up in the frequency scale, and the modes seem less numerous.

In search of explanation of this discrepancy we calculated the profiles of the dynamic components of the magnetization vector in the PWM. The coloured maps in Fig. 5.3, bottom, represent the modulus $|m_z|^2$ of the z component for a number of lowest-frequency modes; blue and red correspond to low and high values of $|m_z|^2$, respectively. In all the modes in question the magnetization is pinned at the Py/air interfaces (thin white lines). Therefore,

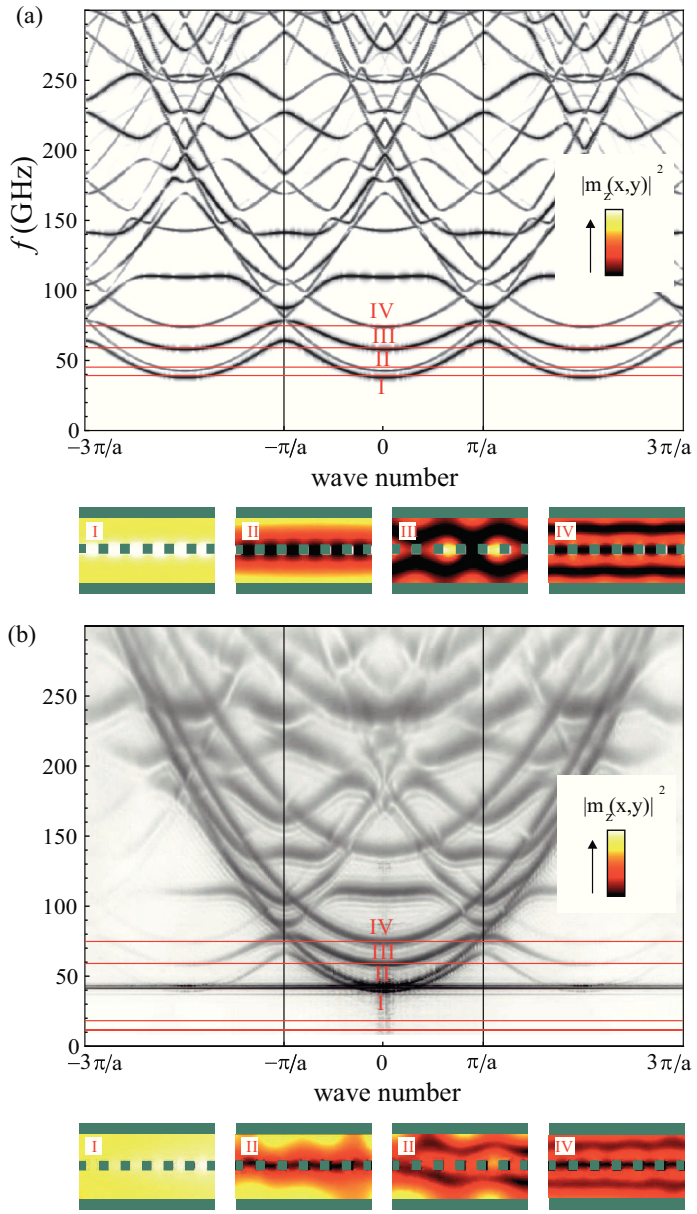

Figure 5.2.: Dispersion of SWs in the MAW presented in Fig. 5.1, as calculated with (a) OOMMF and (b) Nmag. The vertical lines delimit the first Brillouin zone. The magnetization is assumed to precess freely at the Py/air interface, i.e., unpinned magnetization. Bottom in (a) and (b): maps of $|m_z(x, y)|^2$ for the different values of frequency (I to IV) calculated with (a) OOMMF and (b) Nmag. Note that each distribution of $|m_z(x, y)|^2$ obtained by micromagnetic calculations contains contributions of the eigenmodes differing in the wave numbers. Source: Ref. 213.

we suspect that the main reason for the discrepancy between the results of PWM and the micromagnetic simulation are the different boundary conditions applied in this two methods.

Unfortunately, no extension of the PWM method has been developed yet to allow for unpinned magnetization at the interfaces with non–magnetic material. We can extend the micromagnetic simulations, though, imposing various boundary conditions on the dynamic components of the magnetization vector **M**. The procedure described in the previous section allows one to achieve $\mathbf{m} = 0$ (i.e., pinning of the magnetization **M**) at the interfaces with nonmagnetic material. Figure 5.3, top panel, shows the results of the OOMMF simulations (grey lines) and, superimposed, the PWM data. The agreement between the OOMMF and PWM results is satisfactory now, and the effect of the pinning on the magnonic spectrum of the MAW can be explained in detail.

The changes in the SW spectrum resulting from the introduction of pinning are relatively simple in uniform thin films. The main difference is the occurrence of an extra mode, uniform across the film thickness, in the case of unpinned surfaces; surface-localized modes (surface SWs) can occur, too.[273,281] The frequencies of the higher modes for pinned and unpinned surfaces are quite similar. As we have shown already, the changes in a MAW are more significant and complex. Many additional modes are seen to occur in the MAW spectrum calculated for unpinned magnetization (see Fig. 5.2) compared to those obtained in the pinned case (see Fig. 5.3). Due to the pinning in the row of antidots some modes existing in an unpinned system (the modes with high amplitude of $|m_z|^2$ in the centre of the MAW — see modes I and III in Fig. 5.2) can appear in a pinned system. The pinning in the centre of the MAW reduces the degrees of freedom of the SWs and practically divides the waveguide into two parallel sub–waveguides weakly coupled through the barrier formed by the antidot series. This is due to the small edge-to-edge distance between neighbouring antidots, which results in a minor crosstalk between the SWs propagating in the two sub–waveguides. The confinement of the modes increases their separation on the frequency scale in the case of an MAW with pinned magnetization. Moreover, due to the minor interaction between the sub–waveguides, the eigenstates are almost degenerate for frequencies up to 200 GHz in a wide wave number range.

In the absence of pinning, SWs spread freely over the whole width of the waveguide. This is

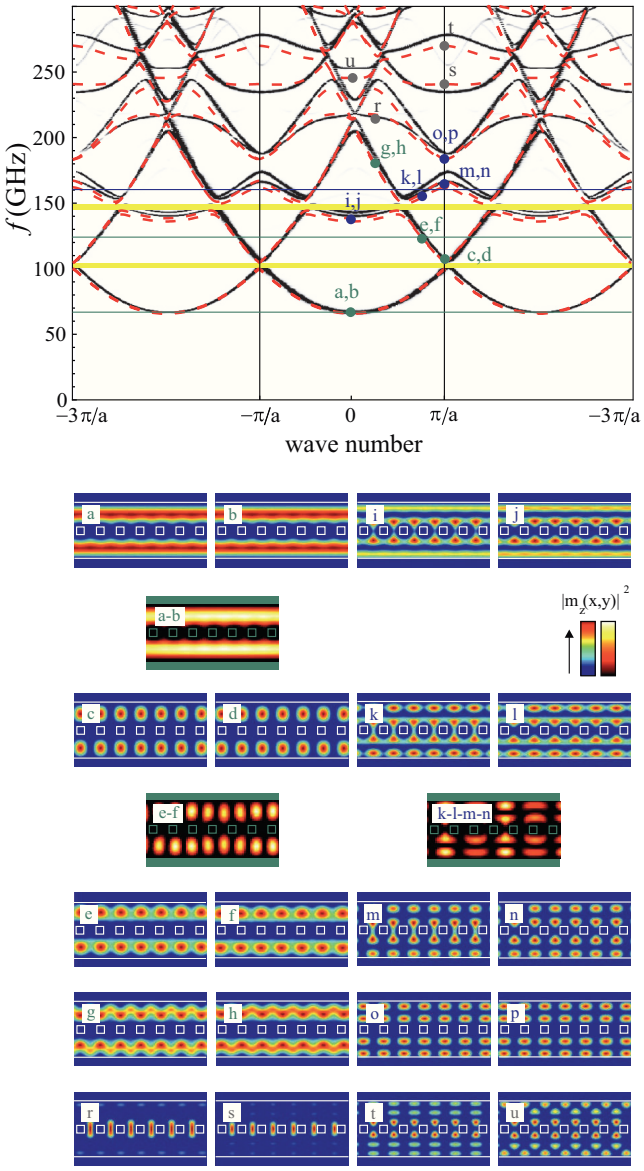

Figure 5.3.: Dispersion of SWs in the MAW presented in Fig. 5.1, as calculated with OOMMF with dynamic magnetization pinned at the Py/air interfaces (grey lines). PWM results are plotted with red dashed lines. Yellow bars represent the magnonic bandgaps (in OOMMF calculations). Bottom: maps of $|m_z|^2$ at points (a) to (u) in the plot above. Green (a–h) and blue (i–p) labels refer to modes originating from the first and second dispersion parabolas, respectively, of each isolated sub–waveguide at the right and left of the central row of antidots. Brown labels denote high-frequency modes localized in the row of antidots. The maps plotted in full colours scale and hot colours scale present the results calculated with OOMMF and Nmag, respectively. The horizontal colour lines in the dispersion plot mark the contributions from different Bloch bands to the OOMMF profiles. Source: Ref. 213.

why the unpinned modes are distributed more densely on the frequency scale. The dispersion branches of some unpinned modes are reminiscent of the continuous parabolas in Fig. 5.2. In the low-frequency range this behaviour is seen in every alternative band, i.e., the 2nd, 4th, and 6th bands from the BZ centre, where a nodal line should appear in the centre of the MAW. The lower amplitude of the SWs in the centre of the MAW results in a negligible impact of the antidot series on the spin dynamics. The effect of the antidot series on the spin dynamics is similarly small in (1) the dispersion branches of unpinned modes with a nodal line in the centre of the MAW [see Fig. 5.2 (c)] and (2) all the dispersion branches of pinned modes. In spite of this, their frequencies are not equal due to the different boundary conditions at the external edges of the MAW. Therefore, no frequency agreement can be expected between the unpinned and pinned modes in wires of the same width.

Another important property of the magnonic band structure of MAWs found in our study is that the magnetization pinning at the edges of the MAW results in the opening of magnonic gaps (yellow bars in Fig. 5.3). This means that even MAWs with as little as 5% air can be used as filters with stop and pass bands. As the first magnonic gap occurs at the border of the BZ, its opening is clearly related to the periodicity of the MAW. However, the second gap (between the 4th and 5th bands) is seen to open inside the BZ. This indicates a different origin of this gap.

The second gap results from the anticrossing between two pairs of modes: modes with no nodal line within each sub–waveguide and modes with a nodal line in each half of the MAW. In other words, the anticrossing occurs between two parabolas (connected with the lower and higher harmonics across the MAW width) of the SW dispersion crossing due to folding to the first BZ.

It is worth noting that the closing of the gaps in the system with unpinned magnetization is due to the presence of additional bands (1st, 3rd, 5th, ...) corresponding to modes with a significant magnetization amplitude in the centre of the MAW [see Figs. 5.3 (a) and 5.3 (b), first and third mode]. These modes are, in fact, more affected by antidots and more separated from each other than the modes with a nodal line in the centre of the MAW, but their presence makes the spectrum of the unpinned system denser and results in more effective bands overlapping.

The relatively small width of the gaps in the system with pinned magnetization is due to the less effective impact of antidots on modes with low value of dynamical magnetization in the centre of the MAW.

The above discussion applies to the low-frequency range, in which the mode quantization is related to the confinement of SWs between one edge of the waveguide and the central row of antidots. In the high-energy range the following effects can interfere with this simple mechanism: (1) SWs can be localized between antidots in the central region of the MAW; (2) the crosstalk can be much more efficient in the case of short SWs, which can easily "leak out" from one sub–waveguide to the other.

Let us discuss in detail the profiles of the dynamic magnetization component $|m_z|^2$ presented in the bottom panel of Fig. 5.3. Three types of modes can be distinguished by profile: (1) modes (a—h) originating from the first mode of each sub–waveguide (no nodal line inside each sub–waveguide); (2) modes (i—p) related to the second mode in the completely isolated sub–waveguides (one nodal line in the MAW); (3) modes (r—u), which are high-frequency excitations localized mostly between antidots in the centre of the MAW. The modes are plotted for different BZ points, indicated in the top panel of Fig. 5.3. The modes in the centre of the BZ have no nodal line perpendicular to the MAW axis, while the modes at the edge of the BZ only have one such line in each BZ. At intermediate points the non–zero amplitude oscillates more smoothly along the MAW axis.

In the low-frequency range the SW modes show the following characteristics: (1) modes occur in pairs with in phase and out-of-phase correlation between excitations in the two sub–waveguides; (2) the frequency difference between the modes in each pair increases with growing frequency; (3) the mode splitting can be suppressed (even for relatively high frequencies) in every second pair of modes at the edge of the BZ, where the nodal line between antidots blocks the crosstalk between sub–waveguides (cf. modes o, p to m, n).

In order to verify the mode profiles calculated using PWM we plotted also some profiles with the aid of micromagnetic simulation (OOMMF). They are presented in Fig. 5.3 in a hot colours scale and their frequencies are marked by horizontal lines to show from which bands they collect the contributions. The labels a, b, e, f, and k, l, m, n present what kind of mixture of Bloch states (calculated using PWM) exist in the profiles calculated with the

aid of OOMMF.

Helpful for practical realizations of MAWs is the insensitivity of the magnonic gaps to the shape of the antidots until its filling fraction and mirror symmetry of MAW is unchanged. On such a small scale, with a feature size of a few nanometres, the shape can be expected to play a minor role. The situation will be different in the magnetostatic regime, *i.e.*, for smaller wave vectors and larger antidot periods where the demagnetizing field is strongly shape dependent and can affect the SW spectrum in the low–frequency regime.[63]

5.3. Conclusions

We have shown that the boundary conditions for the dynamic components of the magnetization vector at ferromagnetic material/air interfaces are of much importance for the SW spectra in nanoscale magnonic antidot waveguides. Our results demonstrate that the magnetization pinning facilitates the opening of magnonic gaps in magnonic antidot waveguides with air filling fraction even as low as 5%. This indicates an additional functionality of these types of waveguides as filters with tunable stop and pass bands. Also, our results show that the pinning will be an important factor to be considered in the interpretation of experimental data obtained for antidot lattices or designing new devices in which the antidot arrangement is periodic in nanoscale. The pinning or unpinning at the interfaces is usually related to the surface magnetic anisotropy, determined by the shape of the atomic orbitals modified at the interfaces by the surrounding material and the reconstruction or relaxation processes. Thus the surface anisotropy can depend on many factors, such as the interface structure on the atomic or nanometre scale, the strain, the crystallographic structure, or the chemical composition.[282] In two-dimensional systems the investigation of these effects can be regarded as an extension of the research in magnetic bilayers and multilayers, which were in focus at the time of the discovery of the giant magneto–resistance effect. We have also shown that peculiar properties of computational methods often used in the calculations are related to specific boundary conditions for dynamical components of magnetization implicitly assumed in each method.

6. Manipulation of Intrinsic and Extrinsic Mirror Symmetry in a Magnonic Antidot Waveguide

*Recently, micromagnetic simulations (MSs) were used to show that periodic waveguides have filter properties due to the opening of magnonic gaps in the SW spectrum at high frequencies.[5,84,267] In this chapter we investigate the influence of the fundamental property of symmetry on the magnonic band structure. We study how loss of mirror symmetry within an one-dimensional nanoscale magnonic antidot waveguide (MAW) may affect the magnonic bandgap. When this symmetry exists then based on their profiles with respect to the central longitudinal axis, the SW spectra can be separated into two groups: symmetric modes and anti-symmetric modes. The breaking of the mirror symmetry will automatically make the classification impossible. We will study two types of the symmetry breaking mechanisms: categorizing them as intrinsic and extrinsic. To demonstrate the generality of the methods discussed here, we have considered two intrinsic factors and two different kinds of field profiles: stepped or ramped (extrinsic factors). The intrinsic factors discussed here are the shape of the antidots and their positions within the MAW. The question is: how do these changes influence the magnonic spectra and the existing bandgaps? Also, how "big" the symmetry breaking needs to be in order to close the gaps? The answers to these questions are very important for the applications of nanoscale SW waveguides in magnonic signal processing and also from the point of view of the basic research, as it concerns fundamental properties of a diverse group of systems. We address these questions

*This chapter is based upon Kłos *et al. Sci. Rep.* **3**, 02444 (2013).

in this article and go even further in terms of magnonic band engineering. We will study the possibility of compensating the changes introduced by the structural modifications in the magnonic spectra by modifying the bias magnetic field. We will demonstrate how collapsed bandgaps in asymmetric waveguides can be restored by the application of the asymmetric bias magnetic field. The extent of this restoration is also studied.

6.1. Methods

The calculations of the magnonic band structure are performed with the finite difference method MS and the PWM, with OOMMF[250] and a Fortran code developed by us, respectively. Both methods solve the Landau-Lifshitz-Gilbert (LLG) equation. The damping is neglected in PWM calculations and included in MS ($\alpha = 10^{-4}$). The effective magnetic field $\mathbf{H}_{\text{eff}}$ here consists of the bias magnetic field $\mathbf{H}_{\text{bias}} = (H_0, 0, 0)$, demagnetizing field and exchange field. The pinned dynamical components of the magnetization vector were assumed at Py/air interfaces in calculations with both methods. The pinning in OOMMF was introduced by fixing magnetization vector in all cells of the discretization mesh, which border the antidots, *i.e.*, for the width 0.5 nm along y axis. (In MS the discrete mesh size of $1.5 \times 0.5 \times 3$ nm along x, y and z axis, respectively, were used. The MS were performed for 4 ns. In the PWM we use 961 plane waves.) Further details on obtaining the SW dispersion relations by analysing the results of MSs are discussed in Sec. 4.1. In the PWM the pinning is applied exactly at the edges of Py. Due to small thickness of the MAW, uniform SW profile across the thickness is assumed. Both methods were already used in the calculations of the SW dynamics and proved to give correct results.[57,58,213,262]

6.2. Results

6.2.1. Magnonic Band Structure in Symmetric and Asymmetric MAW

We study the symmetric and asymmetric magnonic waveguides based on the antidot lattice structure shown in Fig. 6.1. It has the form of a thin (thickness $u = 3$ nm) and infinitely long

permalloy ($Ni_{80}Fe_{20}$) stripe with a single row of square holes ($s = 6$ nm antidots) disposed periodically along the central line. The stripe width and the lattice constant are fixed at $2 \times w + s = 45$ nm and $a = 15$ nm, respectively. The row of holes is placed at the distance $w = 19.5$ nm from the top (and bottom) edge of the stripe in the case of the symmetric MAW. A bias magnetic field, strong enough to saturate the sample ($\mu_0 H_0 = 1$ T), is applied along the length of the stripe. The material parameters of Py were assumed in calculations.

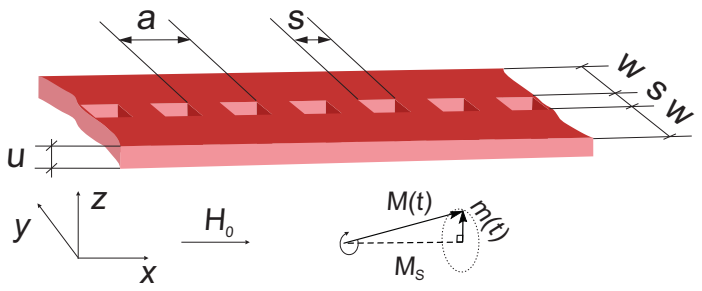

Figure 6.1.: Antidot lattice waveguide under investigation: $u = 3$ nm thick and $2w + s = 45$ nm wide (infinitely long) Py stripe with a periodic series of square antidots (of edge $s = 6$ nm) disposed along the waveguide with a period of $a = 15$ nm. The row of antidots divides the waveguide into two sub-waveguides of width $w = 19.5$ nm each. Bias magnetic field $\mu_0 H_0 = 1$ T is oriented along the waveguide, ($x-$axis). Source: Ref. 4.

We start our investigation with the symmetric MAW (Fig. 6.1).[213] The dispersion relations of SWs in the symmetric MAW is shown in Fig. 6.2. The results of the OOMMF simulations are shown in Fig. 6.2 (a) and of the PWM in Fig. 6.2c (black solid lines). The agreement between results from these two methods is satisfactory. The presence of two magnonic bandgaps (of about 4 GHz each) is evident and they are marked in yellow. The origins of these two bandgaps were found to be different. The first one opens at the BZ boundary due to the Bragg reflection of SWs, while the second gap opens up within the BZ.[213] It was shown that this splitting of the bands within the BZ is due to the anti-crossing between two families of modes,[84] those with and without a nodal line in the upper and lower parts of the MAW (see the first row of profiles in the bottom panel of Fig. 6.2). We showed in Sec. 5.2[213] that the pinning at the edges of Py (at the waveguide edges and at edges of antidots) is crucial for the existence of these magnonic gaps.

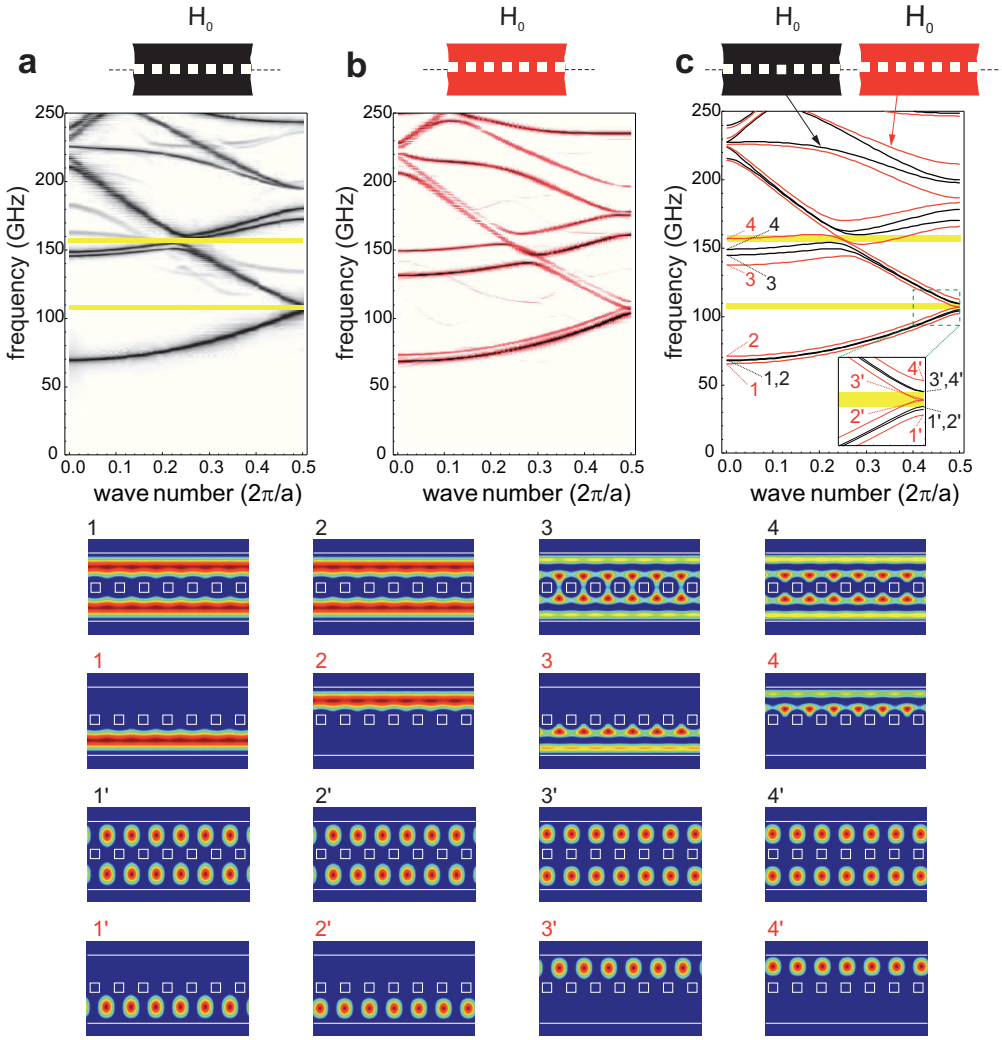

Figure 6.2.: Magnonic band structures of MAWs (shown in insets above the main figures where the thin dashed lines mark the middle of the MAW) calculated with OOMMF in (a) and (b), and with PWM in (c). The band structures for the symmetric MAW are shown in a) and in c) with black solid lines. The results for MAW with upward shifted antidots row are shown in (b) and (c) with red lines calculated with OOMMF ($\Delta w = 1$ nm) and PWM ($\Delta w = 0.9$ nm), respectively. In the bottom panel, the squared amplitudes of the dynamical magnetization $|m_z|^2$ for first four modes in the center (first and second row) and boundary (third and fourth row) of the BZ is calculated with PWM–cf. (c) are shown for symmetric (first and third row) and asymmetric (second and fourth row) MAW. Source: Ref. 4.

The structure investigated above has a mirror symmetry with respect to the central axis of the MAW. Thus, the 1$^{\text{st}}$ and the 3$^{\text{rd}}$ modes are symmetric while the 2$^{\text{nd}}$ and the 4$^{\text{th}}$ are antisymmetric. The frequencies of first two modes (symmetric and antisymmetric one) are

degenerate in the entire wavevector regime and their maps of square of the amplitude of these modes are identical (see the first and third rows of profiles for BZ center and border in the bottom panel of Fig. 6.2). The degeneracy of symmetric and antisymmetric oscillations in the waveguide points at very weak coupling of oscillations localized in the upper and the lower parts of the MAW (in the two equivalent sub-waveguides, Fig. 6.1). The shift of the row of antidots from the central line will break the mirror symmetry of the MAW. If this shift is in $+y$ direction, the upper and lower sub-waveguides will become narrower and wider, respectively. Frequencies of modes localized in the two sub-waveguides will split, with one mode shifted up and the other shifted down on the frequency scale. The dispersion relations of SWs in asymmetric MAWs, obtained by shifting the row of antidots by $\Delta w = 1$ nm and 0.9 nm upward, calculated using OOMMF and PWM, are presented in Figs. 6.2 (b) and (c) (red lines), respectively. (In OOMMF slightly larger value of Δw were used because of the limitations of the discretization mesh and time needed for simulations.)

We see that a shift of the antidots row (along the width of MAW) by only 2% of $2w + s$ is enough to close both magnonic gaps. At the BZ center, the first (second) mode center has an amplitude concentrated in the wider (narrower) part of the MAW of width $w + \Delta w$ ($w - \Delta w$) (see profiles in the second row in Fig. 6.2 at the bottom). The modes 3' and 4' at the BZ boundary originate from modes 1' and 2', respectively due to the folding from the neighboring BZ. Therefore, their profiles of amplitudes are quite similar. Typically, lower frequency modes are concentrated in wider regions of space. It means that two lower (higher) modes must be concentrated in wider (narrower) MAW. Note that, the oscillations of the magnetization amplitude for the modes at the BZ boundary are related to the shifting of the phase of the Bloch waves with the period of the lattice. When $\Delta w = 0$, modes 1' and 2' are concentrated in relatively larger regions (between the antidots) in the two sub-waveguides when compared to the coverage of modes 3' and 4' (directly above or below the antidots). However, when the mirror symmetry is lost ($\Delta w \neq 0$), 1' and 3' cover the larger regions between the antidots while 2' and 4' are limited to the smaller regions directly above or below the antidots in the two sub-waveguides. Further, 3' and 4' are on a narrower sub-waveguide as compared to 1' and 2'. This makes the spatial distribution of 2' and 3' comparable in shape and expanse. Thus these two modes have similar frequencies at the BZ

boundary which, in turn, leads to the collapse of the first magnonic bandgap. A very similar mechanism is responsible for the closing of the second gap as well; even though the origin of this gap is different and the respective changes of frequencies of the third and the fourth bands are larger. As we mentioned before, the second gap appears at the anti-crossing of the modes with different quantization across the width of MAW. The modes 3' and 4' have no horizontal nodal line inside of each sub-waveguides whereas the modes 3 and 4 have one for each part of the MAW.

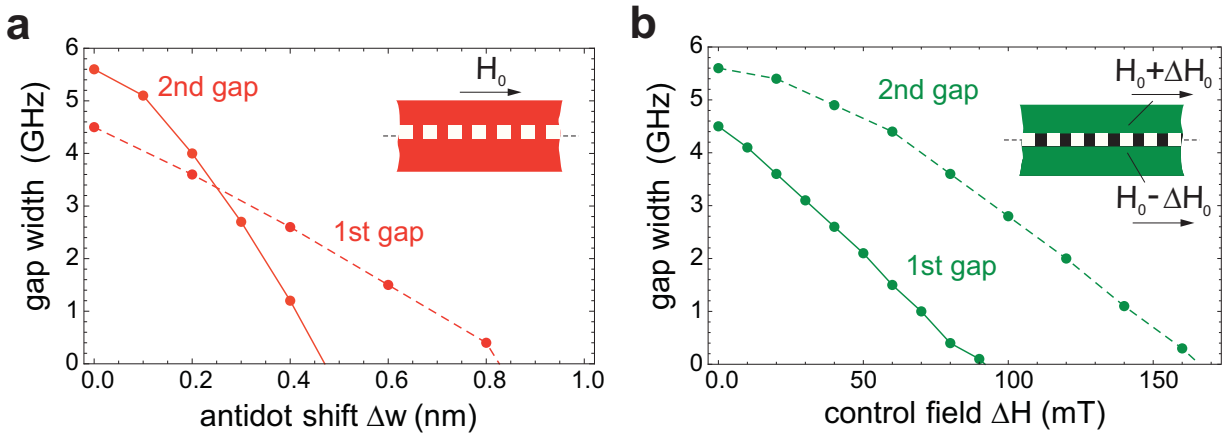

Figure 6.3.: Width of magnonic gaps in the considered MAW as a function of (a) the shift of the antidots row Δw, and (b) an additional asymmetric bias magnetic field ΔH_0 in the symmetric MAW. The ΔH_0 increases the bias magnetic field in the upper half of the MAW (to $H_0 + \Delta H_0$) and decreases the bias magnetic field in the lower half of the MAW (to $H_0 - \Delta H_0$). Source: Ref. 4.

The bandgap widths as a function of Δw are shown in Fig. 6.3 (a). The width decreases monotonously with increasing Δw. The slope for the second gap is larger leading to its complete collapse at $\Delta w = 0.45$ nm, while the first gap exists up to 0.8 nm. We note that the shift of the antidots row does not change the translational periodicity in the structure. Thus the observation of magnonic bandgap closing shown in Fig. 6.3 (a) is purely related to the loss of the mirror symmetry of MAW and associated movement of different modes.

We now demonstrate that breaking the mirror symmetry by extrinsic means can also lead to splitting of the bands and closing of magnonic gaps. In Fig. 6.4 we show PWM results (dashed green lines) with the additional magnetic field ΔH_0 ($\mu_0 \Delta H_0 = 180$ mT) applied (a) parallel and (b) antiparallel to the original bias H_0, in the upper part of the symmetric MAW. The black solid lines mark the magnonic band structure for the homogeneous magnetic field,

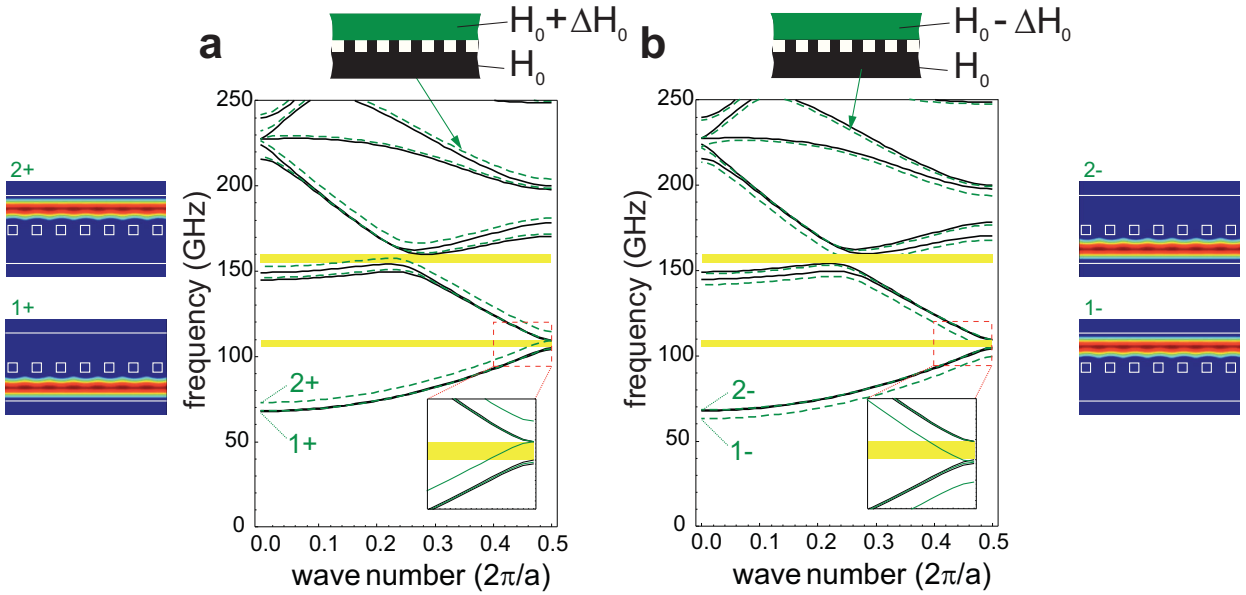

Figure 6.4.: Magnonic band structure of the MAW (presented in Fig. 6.1) calculated with PWM for asymmetric bias magnetic field (green dashed lines). The additional magnetic field of $\mu_0 \Delta H_0 = 180$ mT is applied in the upper part of the MAW (a) parallel and (b) antiparallel to the direction of the bias field H_0. The magnonic band structure for the symmetric MAW with homogeneous bias magnetic field is shown in black solid lines in (a) and (b). The squared amplitudes $|m_z|^2$ for the first and second modes in the BZ center are presented on both sides of the figures for the MAW with asymmetric bias magnetic fields. Source: Ref. 4.

i.e., the same as in Fig. 6.2 c). The parts of the MAW where the increased or reduced bias magnetic fields were applied were 18 nm wide from the closest MAW edge. Similar results were also obtained from simulations (not shown). The parts of the MAW with changed (increased or decreased) bias magnetic field are marked with green colour in the insets of Fig. 6.4. From Fig. 6.4, we can see that the (a) increase or (b) decrease of the bias magnetic field splits frequency bands by shifting the position of some modes up or down, while other frequency modes remain unchanged. The squared amplitudes of the SWs pertaining to the first two modes (1 and 2) are calculated at the BZ centre and are shown at the left and right of Fig. 6.4. A selective population distribution, predicated upon the changed external field, is clearly evident amongst these modes. The increase (decrease) of the bias magnetic field in the upper half of the MAW increase (decrease) the frequency of the modes localized in this sub-waveguide. It is worth noting that an uniform change of the magnetic field will shift the whole spectra but preserve the bandgaps in the structure.

6.2.2. Compensation of the Effect of an Intrinsic Symmetry breaking

We have just shown that the magnonic spectra, especially the magnonic bandgaps for the considered MAW are sensitive towards loss of its (intrinsic or extrinsic) mirror symmetry. We now investigate if it is possible to compensate the effect of an intrinsic symmetry breaking in a MAW by an extrinsic factor. In our case it will be a compensation of the effect of the structural asymmetry on the magnonic band structure (and magnonic bandgaps) by asymmetric bias magnetic field. The answer will begin from the development of an analytical model.

We showed that the amplitudes of modes from the first four magnonic bands in asymmetric MAW concentrate mainly at the top or bottom part of the structure (see the square of the amplitude in Figs. 6.2 and 6.4). This allows for a qualitative explanation of the observed changes in magnonic band structure by a model of two sub-waveguides (in the upper and lower parts of the waveguide), which are weakly coupled through a row of antidots. This observation lets us also to make the estimation of a compensation of the symmetry breaking mechanisms. We will discus first the effect of the changes of the width and bias magnetic field in a single waveguide on the dispersion relation of SWs.

In the homogeneous waveguide the solutions of the linearised LLG equation (with damping neglected) can be written in the following form: $\mathbf{m}(x,y) = \mathbf{m}(y)\mathrm{e}^{ik_x x}$, where k_x is the wave-vector of the SW along the waveguide and $\mathbf{m}(y)$ describes the dependence of the amplitude of dynamical components of the magnetization $\mathbf{m}$ across the waveguide width (we assume the uniform magnetization across the waveguide thickness, which is much less than the width). The solutions can be estimated as: $\mathbf{m}(y) \approx \sin(\kappa y)$, $\cos(\kappa y)$ where the transversal component of the wave-vector $\kappa = (n+1)\pi/w_{\mathrm{eff}}$ is quantized ($n = 0, 1, 2, \ldots$ counts the number of nodal lines across the waveguide width). For strong but not ideal pinning the effective width $w_{\mathrm{eff}} = wd/(d-2)$ depends on the pinning parameter d, which determines the boundary conditions for magnetization and gives also a possibility to include the dipolar effects into the model.[255] It varies in general from 0 to ∞ for the transition from unpinned to fully pinned boundary conditions. The pinning parameter $d = 2\pi(1-\frac{K_{\mathrm{s}}}{\pi M_{\mathrm{s}}^2 u})/[\frac{u}{w}(1-2\ln(\frac{u}{w})+(\frac{\lambda_{\mathrm{ex}}}{u})^2)]$ depends both on the material and structural parameters

(K_s denotes the surface anisotropy). It accounts for both the exchange and the dipolar interactions. For $d \approx \infty$, as in our numerical calculations, $n = 0$ means no nodal line in the upper or lower part of the MAW (see, Fig. 6.2; modes 1 and 2), $n = 1$ denotes a single nodal line (see, Fig. 6.2; modes 3 and 4), etc. The dispersion relation of SWs in the waveguide can be written in the form:[28,255]

$$\omega = \sqrt{(\omega_0 + \omega_\mathrm{ex})\,(\omega_0 + \omega_\mathrm{ex} + \omega_\mathrm{dip})}, \tag{6.1}$$

where ω is the angular frequency of SWs. $\omega_0 = \gamma\mu_0 H_0$, $\omega_\mathrm{ex} = \gamma\mu_0 M_\mathrm{s}\frac{\lambda_\mathrm{ex}^2}{w^2}(n^2\pi^2 + k_x^2 w^2)$, $\omega_\mathrm{dip} = \gamma\mu_0 M_\mathrm{s}\frac{1-\exp(-k_x u)}{k_x u}$ denote the contributions from external, exchange and dipolar fields, respectively.

The estimations of changes in SW dispersion relation resulting from the changes of w or H_0 can be done by calculation of the full differential of the function $\omega = \omega(w, H_0)$. It will allow one to derive the relation between small changes of ΔH_0 and Δw, for which the desired compensation between intrinsic and extrinsic symmetry breaking is obtained, *i.e.*, when $\mathrm{d}\omega(w, H_0) = 0$:

$$\frac{\mu_0 \Delta H_0}{\Delta w} \approx \frac{2\pi^2 \mu_0 M_\mathrm{s} \lambda_\mathrm{ex}^2 (n+1)^2}{w^3} \times f\!\left(\frac{K_\mathrm{s}}{\pi u \mu_0 M_\mathrm{s}^2} - 1, \frac{\lambda_\mathrm{ex}}{w}, \frac{u}{w}\right). \tag{6.2}$$

This ratio, having units of T/m, describes how much extra asymmetric magnetic field needs to be added to compensate for the shift in the row of the antidots. The function: $f(s, l, r) = [s + \frac{1}{\pi}(2\frac{l^2}{r} - 4r\ln(r))][s + \frac{1}{\pi}(r + \frac{l^2}{r} - 2r\ln(r) - s)]s^{-2}$ depends on three dimensionless parameters: s–the relative strength of the surface anisotropy, l–ratio between exchange length and the width of the waveguide and r–the aspect ratio of the waveguide. The values of $f(s, l, r)$ with big absolute value of K_s, refer to the regime of strong pinning. Note that Eq. (6.2) does not depend on k_x, which means that it should be fulfilled for any wave-vector.

In our MAW, we have two sub-waveguides separated by the antidots row. When we shift the row of the antidots by Δw along positive y direction, the width of the upper sub-waveguide decreases by Δw and the width of the lower sub-waveguide increases by the same amount. This causes the higher and lower frequency modes to become concentrated in the narrower and wider sub-waveguide, respectively. To compensate for these changes in

the dispersion relation by a bias magnetic field we need to do the opposite. According to Eq. (6.2) we need to apply different bias magnetic fields to upper and lower sub-waveguides. The dependence of the magnonic gap width under asymmetric bias magnetic field of the step-like shape applied to the MAW; *i.e.*, in the upper part of the MAW bias magnetic field is $H_0 + \Delta H_0$, while in the lower part of MAW is $H_0 - \Delta H_0$, calculated with PWM is shown in Fig. 6.3 (b). We can see decrease in the gap widths with increasing ΔH_0, similar to the changes observed with increasing Δw.

After these estimations we perform the PWM calculations. The results are presented in Fig. 6.5 (b) and (c) for ΔH_0 to recover the first and the second magnonic gaps in the asymmetric MAW (*i.e.*, when $\Delta w = 0.9$ nm and 0.5 nm), respectively (see Fig.6.3 (a)). It is interesting that we found it possible to recover the first and the second magnonic gaps but with different values of the ratio $\frac{\mu_0 \Delta H_0}{\Delta w}$. The analytical values of this ratio (calculated from the Eq. (6.2)) with $w = 18.5$ nm, *i.e.*, the distance between pinned layers used in MS) for the ideal pinning ($f(s, l, r) = 1$) for the first gap (when $n = 0$) and the second one ($n = 1$) are 101 mT/nm and 406 mT/nm, respectively. To validate our predictions we performed MSs for $\mu_0 \Delta H_0 = 105$ mT and $\Delta w = 1$ nm. The simulation results are shown in Fig. 6.5 (a) with the first frequency gap opened and in good agreement with the PWM calculations shown in Fig. 6.5 (b). Although, the second bandgap is formed due to the anti-crossing of the $n = 0$ and $n = 1$ modes, at $\Delta w = 0.5$ nm the splitting of the $n = 1$ dominates (see Figs. 6.2 (b) and (c)). Hence, in order to open the second gap we have to target the shifts for the bands with a single nodal line ($n = 1$) by applying the field for which $\frac{\mu_0 \Delta H_0}{\Delta w}$ is about 4 times bigger than that for the first gap (410 mT/nm). This confirms the applicability of Eq. (6.2) with a square dependence on $n + 1$. The profiles of SWs (compare bottom panels of Fig. 6.2 and Fig. 6.5) further establish the restoration of amplitude distribution by extrinsic compensation. The presented results proved that the asymmetric bias magnetic field can reduce the effect of the intrinsic symmetry breaking introduced by the shifting of the position of antidots on magnonic spectra. Small differences in the extent of bandgap recovery obtained from numerical calculations and the analytical model, show that the pinning in the middle of MAW is not perfect.

Our predictions should also be applicable to MAWs where the loss of the mirror symmetry

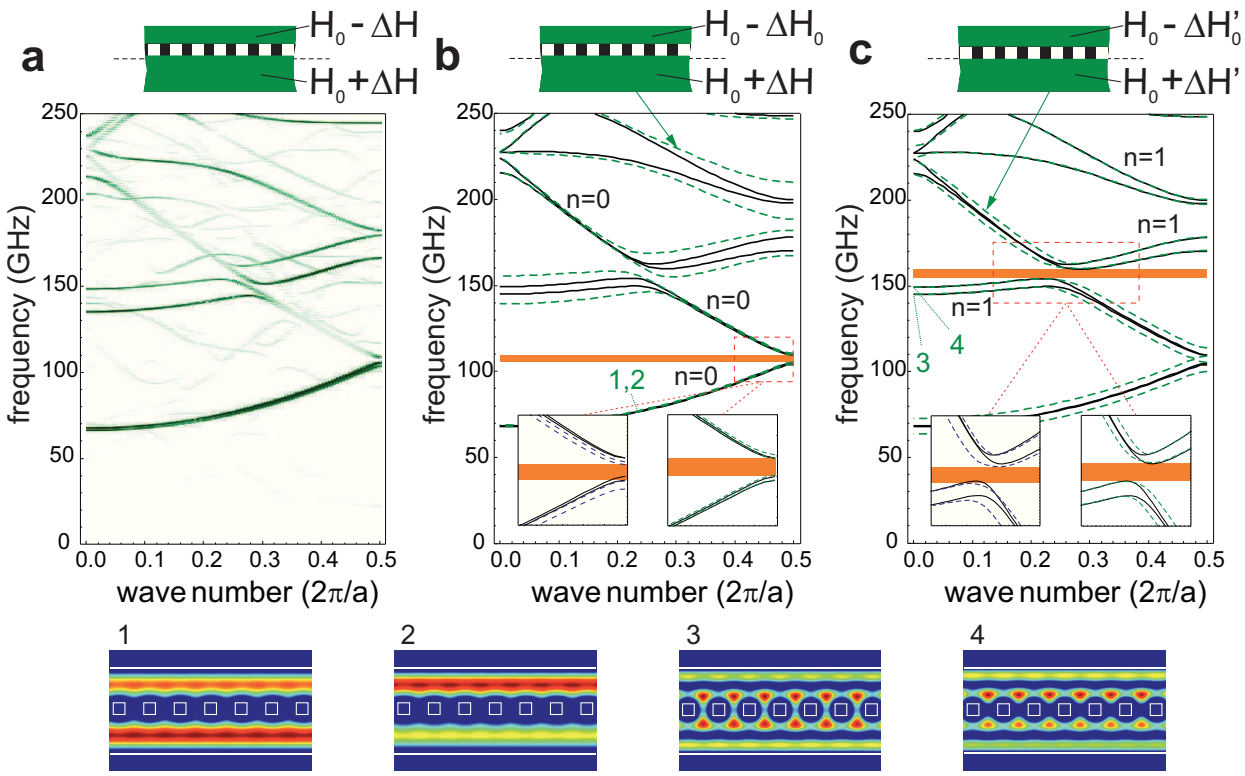

Figure 6.5.: Magnonic band structure of the MAW showing the compensation effect of an intrinsic asymmetry by an asymmetric extrinsic field. In (a) and (b) (green lines) the first gap (for the modes $n = 0$) is reopened. The calculations with OOMMF (a) and PWM (b) were performed for $\Delta w = 1$ nm and 0.9 nm, respectively, with $\mu_0 \Delta H_0 = 105$ mT ($\mu_0 H_0 = 1$ T). The reopening of the second gap (opened in the anti-crossing of the mode $n = 0$ with $n = 1$) is presented in (c). Calculations in (c) were done with PWM for $\mu_0 \Delta H_0 = 205$ mT and $\Delta w = 0.5$ nm. The left insets in (b) and (c) show enlarged results for the step-like field profile of the bias magnetic field; and the right ones show the outcomes for linear change of the magnetic field profile (ramp-like profile) across the MAW. At the bottom, profiles of SW calculated with PWM are shown. Profiles for modes 1 and 2 are calculated for the band structure in (b) and modes 3 and 4 for the band structure in (c) at the BZ centre. Source: Ref. 4.

has occurred due to a change in a different intrinsic parameter. In order to establish the same, we now perform calculations for MAW with rectangular antidots. The new MAW structure is shown at the top row of Fig. 6.6. The MAW consists of the rectangular antidot row with dimensions 6 nm × 4.5 nm, along the waveguide and across its width, respectively. The sub-waveguides formed on both sides of the antidots have now different width of w =19.5 and $w + \Delta w = 21$ nm. Study of this kind of asymmetry can be of practical importance,

because such unintended defects can occur during the design or fabrication stages. The magnonic band structures calculated with PWM and OOMMF for this MAW are shown in the Fig. 6.6 (a). We can see that the mirror symmetry breaking by the decrease of antidots size across the waveguide width results in the splitting of magnonic bands and consequently the collapse of bandgaps in a manner similar to the results presented in Fig. 6.2 (b). The analytical formula Eq. (6.2) still can be used to estimate the bias magnetic field necessary to reopen magnonic bandgap in the spectra. According to Fig. 6.6 (a) we need to increase the frequency of the first and third modes without affecting the second and forth modes. According to our models, we should be able to achieve this simply by increasing the magnetic field in the wider (21 nm wide) part of the MAW by $\mu_0 \Delta H_0 = 0.02$ T. The result of the calculations for the step-like magnetic field is shown in Fig. 6.6 (b). The first magnonic bandgap has almost the same width as for the symmetric waveguide. The results of the PWM calculations are confirmed by MSs, which are shown in Fig. 6.6 (a) and (b) as colour maps. The good agreement is found.

6.3. Discussion

We have shown that a small mirror symmetry breaking in MAW by the shift of the row of antidots from the waveguide axis or by an asymmetric change of their shape (*i.e.*, by changes, which leave the discrete translational symmetry of the lattice intact) can result in closing of magnonic bandgaps in the range of the spectra determined mainly by exchange interactions. We observed that the loss of symmetry causes a redistribution of the amplitude associated with different SW modes in the physical space of the MAW. This results in the movement of modes in the SW spectrum. Although, the two bandgaps observed and discussed here have different origins, their collapse is demonstrably a direct result of the loss of the mirror symmetry and the associated redistribution of SW amplitude.

Moreover, we have shown that the magnonic bandgap in the asymmetric MAW can be reopened by an asymmetric bias magnetic field of a step-like profile across the MAW width. With the help of an analytical model we were able to extract the main parameters responsible for closing the gap and its reopening by the external magnetic field. It was presented that

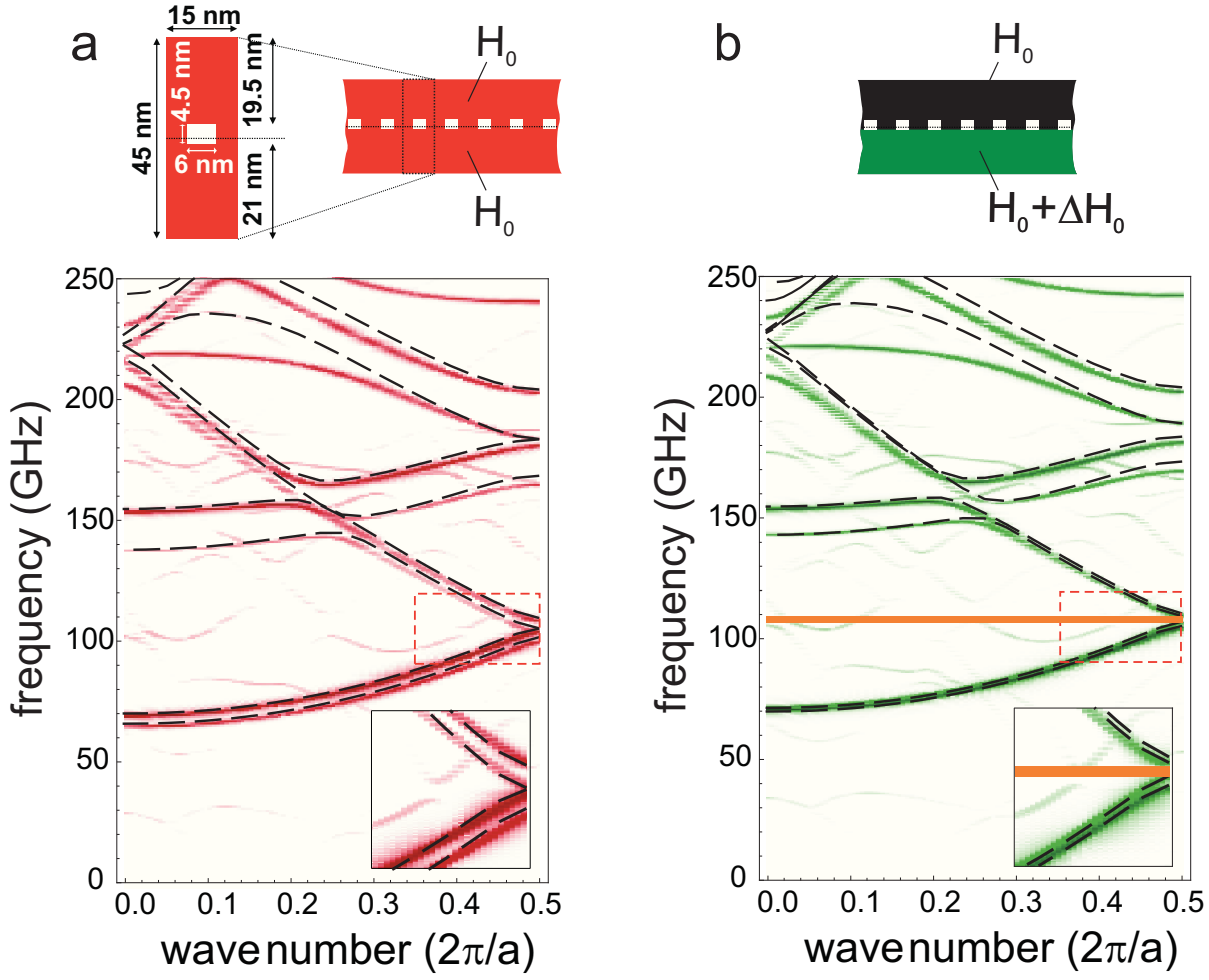

Figure 6.6.: Magnonic band structure of the MAW with rectangular antidots of dimensions 6 nm × 4.5 nm (shown at the top). The antidots row separate two sub-waveguides of different widths, 19.5 nm and 21 nm. The uniform bias magnetic field $\mu_0 H_0 =$ 1.0 T is applied parallel to the MAW axis. The dashed lines and the colour maps show the results from PWM calculations and MSs, respectively. (b) The magnonic band structure for the same MAW as in (a) but with step-like bias magnetic field with the value of $\mu_0 H_0 = 1.0$ T in the narrower waveguide and $\mu_0(H_0 + \Delta H_0) = 1.2$ T in the wider waveguide. The first magnonic gap marked by the coloured rectangle has reopened. Source: Ref. 4.

two magnonic bandgaps of different origins can be selectively reopened in the asymmetric waveguides by this way. It was shown here with an analytical model and also in some papers,[68,213,242] that the detailed shape of antidots and random defects do not play significant roles in effects studied in the manuscript. Our results can be crucial for practical realization of SW waveguides for magnonic applications in high frequencies, because precise mirror

symmetry is difficult to achieve on such small scales, leading to deviations form the ideal structure. The intrinsic and extrinsic symmetry breaking or its compensation can also be exploited to tailor the magnonic band structure or manipulate active and inactive waveguide modes, which couple to the external fields[83,283] in a similar way as was predicted for plasmonic metamaterials.[284]

The experimental proof of the compensation effect proposed here with the step-like profile of the bias magnetic field is challenging. More feasible for experimental realization will be a continuous change of the bias magnetic field. We propose to use a ramp-like profile of the magnetic field:[285] $H = H_0 + 2\Delta H_0(2y + \Delta w)$, where $y = 0$ corresponds to the MAW center. The values of Δw and ΔH_0 can take the same values as for the step-like profile of magnetic field considered above. The results of PWM calculations for the ΔH_0 and Δw taken in the calculations presented above are shown in Fig. 6.5 in right insets. These results were also confirmed by MSs. We have found, that this kind of field acts similar to the field with step-like profile, when its value is normalized to the same average value as the step–like field for corresponding sub-waveguides (the aforementioned formula for ramp-like field meets this criteria).

The development of the analytical model presented here was made possible solely by dint of the fundamental properties of discrete translational and mirror symmetries of a crystal lattice. Thus, the main conclusions should not be limited to the particular cases investigated here and it should be possible to extend this idea to other SW waveguides, including those with larger dimensions, or to other types of waves. In the former case the inhomogeneous demagnetizing field, anisotropy of magnetostatic SW dispersion relation,[286] and multi–mode character of waveguides[201] have to be taken into account. Thus, further investigation is necessary. The compensation effects proposed here should find applications also in other systems, like electrons propagating in a periodically patterned graphene nano–ribbon by the external electric field,[287–289] or in photonic, plasmonic and phononic waveguides although with tailored electric and elasticity fields, respectively.

7. Effect of Antidot Shape on Spin–Wave dispersion in a Magnonic Antidot Waveguide

*This chapter aims to help fill that gap in research by numerically simulating the magnonic dispersion in 1D MAW lattices with different geometric shapes of the antidots. We also study the spatial magnetization distribution for different frequencies and wavevectors of the observed dispersion modes. We further plot exchange and demagnetization fields to examine how they change with differing antidot shapes. We have used antidots, which are n sided regular convex polygons inscribed within a circumcircle of radius,

$$r_n = \sqrt{\frac{2fA}{n}\text{cosec}(\frac{2\pi}{n})}; \tag{7.1}$$

such that, the filling fraction f, the ratio of area of the hole to the area A of the unit cell, remains a constant. Micromagnetic simulations were performed for $n = 3$ (triangular), 4 (square), 5 (pentagonal) and 6 (hexagonal antidots) in Object-Oriented Micromagnetic Framework (OOMMF).[250] The case of $n = \infty$ (circular antidots) was simulated using Nmag.[276] This chapter is organized as follows. The geometrical structure of the waveguide and method used for calculating dispersion are described in greater detail in Sec. 7.1. Section 7.2 presents the results and analysis linking the ground state field distribution with changes in the observed SW dispersion modes. Section 7.3 contains the concluding remarks.

*This chapter is based upon Kumar *et al. J. Appl. Phys.* **114**, 023910 (2013).

7.1. MAW and The Numerical Method

7.1.1. MAW Structural and Material Parameters

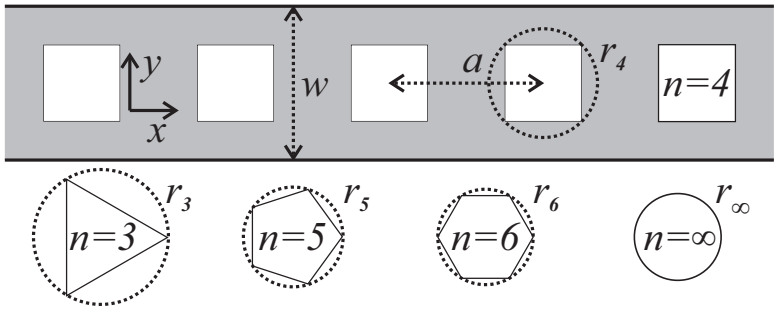

Figure 7.1.: (Top panel) A part of the 1D MAW structure showing square antidots (white holes in grey magnetic region) disposed along the central axis of the waveguide of width, $w = 24$ nm and lattice constant, $a = 24$ nm. The square antidots are inscribed within a circle of radius, r_4. (Bottom panel) Other examined antidot shapes inscribed within their respective imaginary circumcircles. For $n \in \{3, 4, 5, 6, \infty\}$, r_n is given by Eq. (7.1), where filling fraction $f = 0.25$ and unit cell area $A = wa$. Source: Ref. 68.

Figure 7.1 depicts the MAW structures under investigations. The MAWs had both width, w and lattice constant, a set to 24 nm and a length, l and thickness, s of 2.4 μm and 3 nm in all cases. For $f = 0.25$, $A = wa$ and $n \in \{3, 4, 5, 6, \infty\}$, Eq. (7.1) dictates r_n as 21.06, 16.97, 15.56, 14.89 and 13.54 nm, respectively. The material parameters similar to that of permalloy (Py: $Ni_{80}Fe_{20}$) were used during simulations (exchange constant, $A = 13{\times}10^{-12}$ J/m, saturation magnetization, $M_s = 0.8{\times}10^6$ A/m, gyromagnetic ratio, $\bar{\gamma} = 2.21{\times}10^5$ m/As and no magnetocrystalline anisotropy).

7.1.2. Micromagnetic Simulations

Micromagnetic simulations[246] are done with the help of the finite difference method (FDM) based OOMMF (for $n = 3, 4, 5$ and 6) or the finite element method (FEM) based Nmag (for $n = \infty$). For the cell size used here, Nmag reproduces the circular shape much better than that obtained in OOMMF. The use of two different simulation packages also ensures that the established results are independent of the spatial discretization. Both these open source platforms solve the Landau-Lifshitz-Gilbert (LLG) equation.

In order to obtain the SW dispersion relations, a 2D discrete Fourier transform (DFT) was performed on the obtained results.[262] Before simulating the SW dynamics, a magnetic steady state was achieved by subjecting the MAWs to an external bias of 1.01 T (along the length of the waveguide) under a Gilbert damping constant, $\alpha = 0.95$. This high external field saturates the magnetization of MAWs. To observe sharper dispersion peaks α was artificially reduced to 10^{-4} during simulation of the dynamics. For simulations done in OOMMF, cuboidal cells of dimensions $dx = dy = d = 1$ nm and $dz = s = 3$ nm were used to span the MAWs. The resultant gridding of antidot edges which are not aligned with X or Y axes may cause the entire hole geometry to move towards one of the edges of the MAW. How this intrinsic mirror symmetry breaking affects the SW dispersion relations was described in Chap. 6.[4] Nmag, being FEM based, uses adaptive meshing and hence, its outputs do not suffer from this issue. However, spatial interpolation needs to be done in order to obtain magnetization values at every 1 nm interval before performing the DFT. Data was collected every $dt = 1$ ps for both OOMMF and Nmag for a total duration of 4 ns. This gives us a sampling frequency, $f_s = 1000$ GHz. The excitation signal, H_z is normal to the plane of the MAWs and is given by:

$$H_z = H_0 \left(\frac{\sin(2\pi f_c(t - t_0)}{2\pi f_c(t - t_0)} \right) \times \left(\frac{\sin(2\pi k_c(x - x_0)}{2\pi k_c(x - x_0)} \right) \times \left(\sum_{i=1}^{w/dy} \sin(i\pi y/w) \right). \tag{7.2}$$

Here $\mu_0 H_0 = 6$ mT, $f_c = 490$ GHz, $t_0 = 1/(f_s - 2f_c) = 50$ ps, $k_c = \pi/a$ and $x_0 = l/2 = 1$ μm. This form of excitation signal will excite both symmetric and antisymmetric modes of the dispersion relations in a width confined MAW. The aliasing associated with DFT is mitigated by the fact that the signal given by Eq. (7.2) carries no power beyond f_c in the frequency domain. Similarly, power in the wavevector domain is limited to the first Brillouin zone (BZ) from $-k_c$ to k_c.

We also calculated the SW power and phase distribution profiles (PPDPs) for a given $(k,\, f)$ pair of any dispersion relation. It was done by masking the obtained relation with a suitable mask in wavevector domain followed by doing an inverse Fourier transform in the same domain to yield data in physical space. For example, in order to obtain these results for $(k,\, f) = (K,\, F)$ a mask, D_{m} was created to span the entire k vs. f space such that:

$$D_{\mathrm{m}}(k,f)=\begin{cases}1 & \text{if } k=\frac{2}{a}c\pi\pm K\text{: } c \text{ is an integer}\\ 0 & \text{elsewhere.}\end{cases} \tag{7.3}$$

After multiplying D_{m} with the obtained dispersion relations we then take an inverse Fourier transform in k-space to arrive at the desired PPDPs. This mask is designed to include power only from $k = K$ and nullify the power present in the rest of the wavevector domain. Simply performing the inverse transform in k-space without using such a mask will allow power from the entire wavevector range to distort the results.

7.2. Results and Observations

The calculated dispersion relations are tabulated in Fig. 7.2. Frequency ranges from 0 to 120 GHz and wavevector k ranges from 0 to the first BZ boundary (π/a) are displayed. As the bias field is kept constant at 1.01 T, a forbidden region is observed in all the cases up to the ferromagnetic resonance mode of about 39 GHz. SW of any k is not allowed in this region. Bandgap I is also present in all the cases. For triangular, square, pentagonal, hexagonal and circular antidots, its respective values are 4.3 GHz (43 GHz to 47.3 GHz), 5.6 GHz (44.1 GHz to 49.7 GHz), 4.4 GHz (44.5 GHz to 48.9 GHz), 4.4 GHz (44.8 GHz to 49.2 GHz) and 3.5 GHz (44.9 GHz to 48.4 GHz). In the case where the square antidots were tilted by 45° (diamond shaped antidots), bandgaps I & II were observed; and their respective values were 3.6 GHz (44.2 GHz to 47.8 GHz) and 3.5 GHz (57.8 GHz to 61.3 GHz). An additional bandgap (III) of 6.6 GHz (94 GHz to 100.6 GHz) was observed in the case of triangular antidots. Bandgaps II & III are direct but bandgap I is indirect suggesting a difference in their origin which can be studied by looking at the spatial PPDPs for the modes between which they exist.

Figure 7.3 shows the spatial SW PPDPs for the marked (k, f) values in the Fig. 7.2. Only a part of the entire MAW structures have been shown for convenience. Mode ⓐ appears to describe the uniform mode showing insignificant power or phase variation in the medium. The power distribution profile (PoDP) of mode ⓑ, being at the BZ boundary,

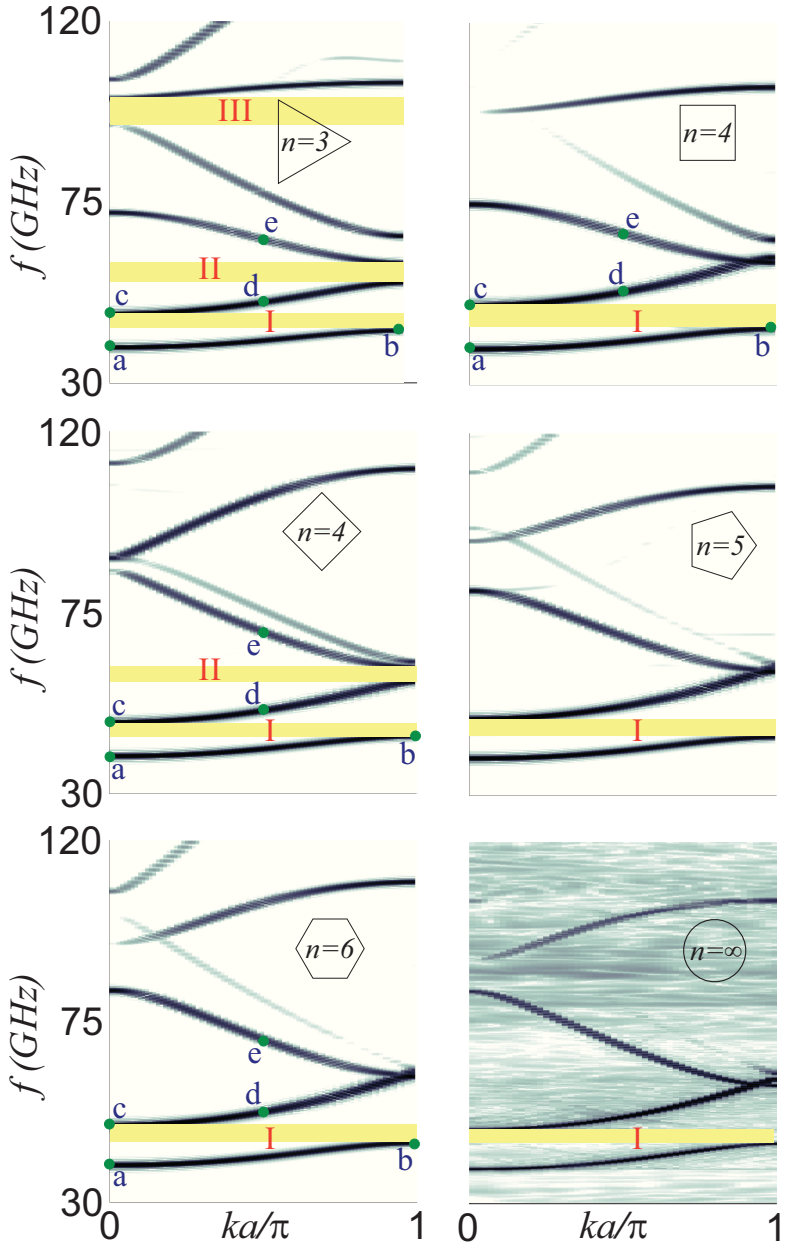

Figure 7.2.: SW dispersion results of MAW structures marked with their respective anti-dot shapes as insets. Indexed band gaps are highlighted with horizontal bars. Source: Ref. 68.

features narrow vertical nodal lines at $x = x_0 \pm (c + 1/2)a$; where c is an integer. The regions joining these nodal lines are π radians out of phase with each other. This suggests that the positions of the phase boundaries in the phase distribution profiles (PhDP) depend on the location of the signal x_0 used in Eq. (7.2). Power distribution profiles for mode © contains a horizontal nodal line right down the centre of the MAWs in all cases. The upper and lower

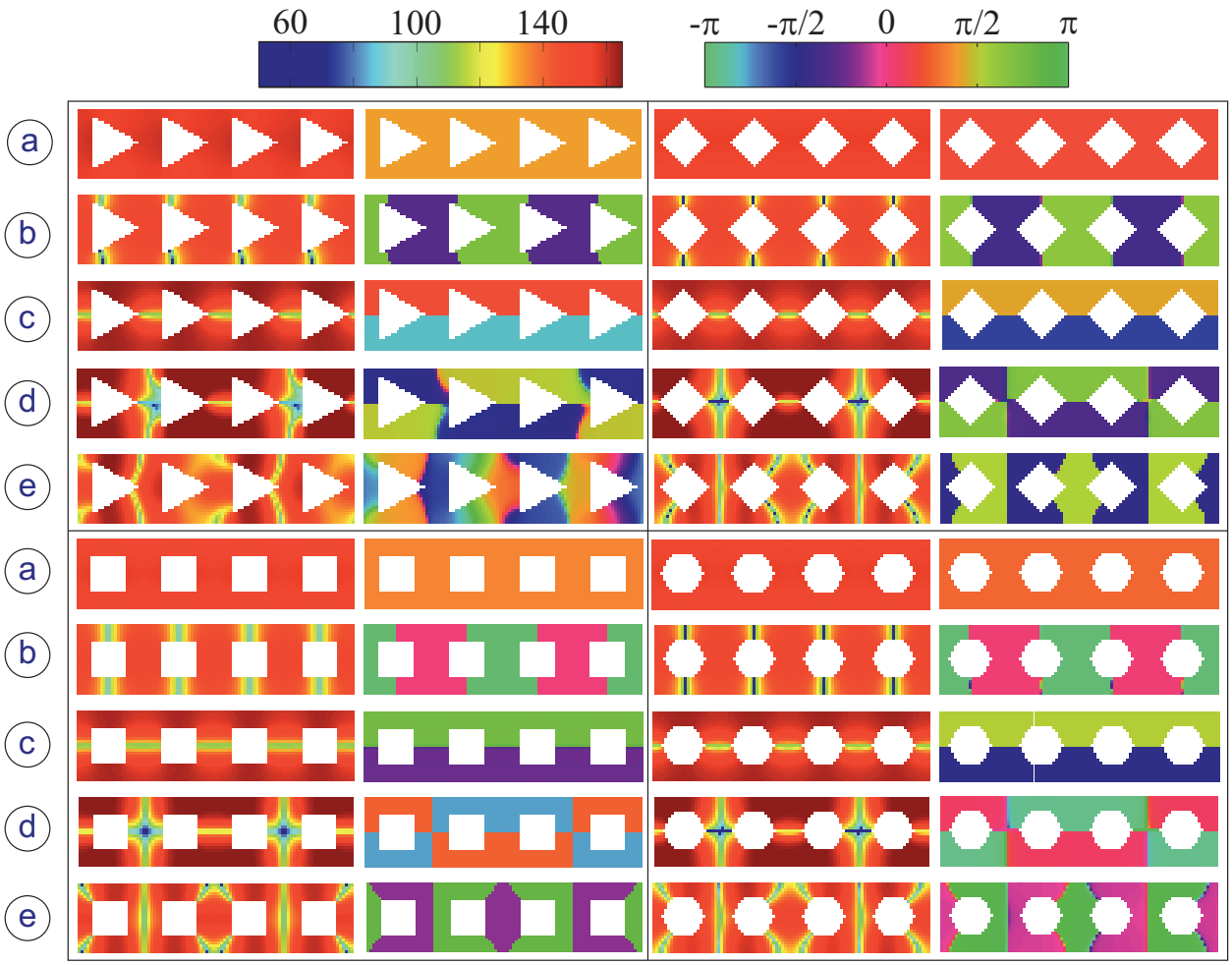

Figure 7.3.: Power (first and third column) and phase (second and fourth column) distribution profiles corresponding to marked (k, f) locations (ⓐ to ⓔ) in Fig. 7.2 for MAWs with triangular, diamond, square and hexagonal shaped antidots. Power is presented on an arbitrary logarithmic colour map while the phase profile representations use a cyclic colour map. Source: Ref. 68.

parts of the waveguide are again π radians out of phase with each other. This hints at the fact that modes ⓐ and ⓒ correspond to zero and first order modes along the width due to the lateral confinement of the waveguide.[215] Modes ⓓ and ⓔ are calculated at $k = \pi/2a$ as they become nearly degenerate at the BZ boundary for square and hexagonal antidots. This degeneracy can lead one of the modes to affect the results of the other. Vertical nodal lines for both these modes are now located at $x = x_0 \pm (2c + 1)a$. Yet again, the position of the phase boundaries appear to be controlled by the location of the signal at x_0. The periodicity of these nodal lines $2a$ is understandable given the location of modes (half way from BZ boundary). Slight curvature is observed in all the nodal lines for triangular

antidots. We attribute this to the lack of mirror symmetry within the hole geometry along a vertical axis. Similar curvature of nodal lines was detected for the MAW with pentagonal antidots (not shown) which also lacked such a symmetry. Belonging to the same dispersive branch of the spectrum, modes ⓒ and ⓓ share a horizontal nodal line which stems from the aforementioned lateral confinement. The observed effects of such confinement and the shape of dispersion curve to which modes ⓐ through ⓓ belong reminds us of the first two (nearly) parabolic dispersion curves observed in the case of a uniform waveguide.[79] In contrast, mode ⓔ belongs to dispersive branch in the spectrum, which curves downwards. This branch is formed by the anti-crossing of lowest energy modes originating in the two neighbours of a BZ; and as such mode ⓔ unlike modes ⓐ and ⓑ does not show any horizontal nodal lines. Since the first two lowest energy branches share the same upward curvature, only indirect bandgap originating in the same BZ is possible. The third lowest energy branch of a BZ which originates in its two neighbouring BZs (aided by zone folding) has downward curvature. Thus, only a direct bandgap can be supported between this and the second lowest energy curve at the BZ boundary.

A quick visual comparison of different dispersion relations displayed in Fig. 7.2 reveals a qualitative convergence of dispersion modes starting as early as $n = 4$ (square antidots). No new band gaps open or close. Section 5.2 discussed such similarities between results from different antidot based MAWs and how this convergence, or insensitivity towards the shape of the hole is desirable for the functioning of MAWs. However, note that when the square antidots are tilted by 45° (diamond shaped antidots) (see Fig. 7.2, left column middle row), one of the band gaps from $n = 3$ case is partially restored. The computations of the exchange and the dipole field profiles (EFPs and DFPs) are done to help understand the cause for this observation. These profiles are shown in Fig. 7.4. It may be noted how the EFP around the square antidots matches to that around the hexagonal antidots. They have similar field orientations and cover similar regions in space. Maximum value of the this field is of the order of 20% of M_s. However, their demagnetizing field profiles do not match well. On the other hand, the demagnetizing field profile around the tilted square antidots matches better with the same around the hexagonal antidots (similar field orientations and elongated coverage in space and comparable maxima of the order of 50% of M_s). Hence, the demagnetizing field or

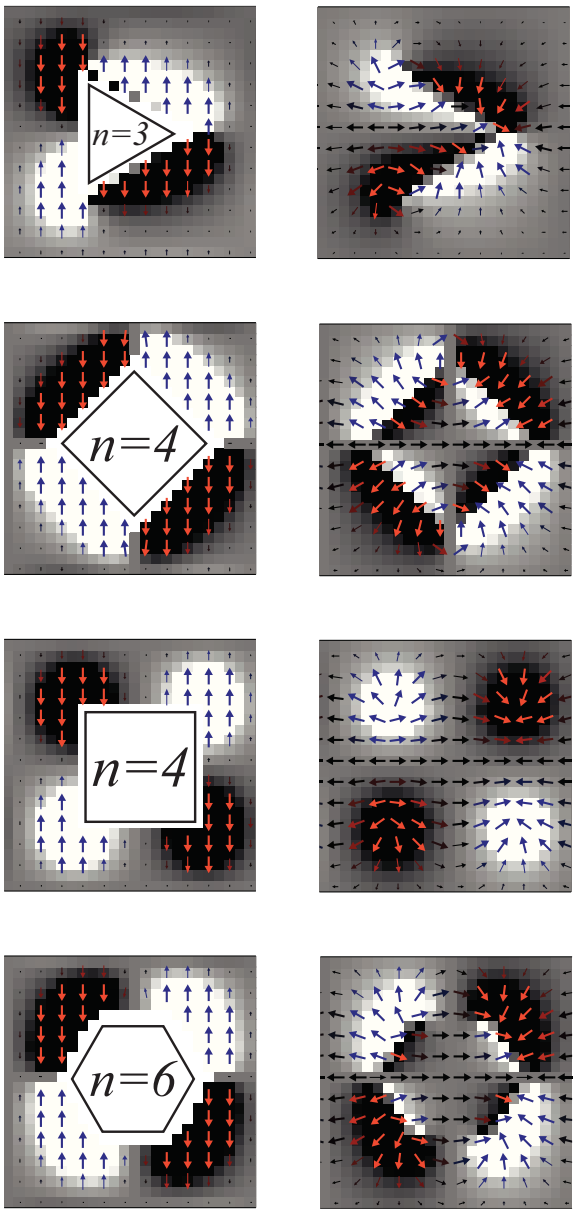

Figure 7.4.: Exchange (left column) and demagnetizing (right column) field profiles at $t = 0$ for $n = 3, 4$ & 6 (marked by insets).

its corresponding potential distribution, may not be the cause of the observed changes in the band structure. Dipole dominated SWs, which occur in much larger structural dimensions are more likely to be affected by the demagnetizing field distribution. To further test the postulate, that the dispersion in considered MAWs is largely dependent upon the exchange field distribution, the case of diamond shaped antidots was considered. It was anticipated that these antidots will produce elongated regions of inhomogeneous exchange fields (similar

to what is observed along the slanting edges of the triangular antidots) as opposed to chiefly circular ones (which is seen in the case of square antidots). Surly enough, the exchange field profiles of triangular, diamond shaped and square antidots were remarkably different from each other (as one of the edges of triangular antidot is vertical). This establishes a correlation of observed SW dispersion on their exchange instead of their demagnetizing field distribution.

Exchange energy density, $E_{\text{exch}}(\mathbf{r_i})$, which contributes to the total energy $\mathbf{M} \cdot \mathbf{H}_{\text{eff}}$, is isotropic in a homogeneous magnetic medium with uniform exchange coefficient A. This field is calculated in OOMMF[250] as given below:

$$E_{\text{exch}}(\mathbf{r}_i) = A\mathbf{m}(\mathbf{r}_i) \cdot \sum_{\mathbf{r}_j} \frac{\mathbf{m}(\mathbf{r}_i) - \mathbf{m}(\mathbf{r}_j)}{|\mathbf{r}_i - \mathbf{r}_j|^2}. \tag{7.4}$$

Where $\mathbf{r}_j$ enumerates the region in the immediate neighbourhood of $\mathbf{r}_i$. In the absence of SW dynamics $\mathbf{m}(\mathbf{r}_i) - \mathbf{m}(\mathbf{r}_j) \simeq 0$ except where $\mathbf{r}_j$ lies close to antidot boundary. Therefore, by changing its geometrical boundary, the exchange field distribution around an antidot can be changed. This can conceivably scatter exchange dominated SWs differently and alter their resultant dispersion relation.

It also needs to be considered if the simulations represent the physical reality. Particularly, how can FDM or FEM based ordinary differential equation solvers like OOMMF or Nmag, which necessarily discretize the continuous sample, calculate the isotropic exchange energy and the demagnetization energy[247] with good accuracy? Reference 253 concludes that the discrete representations should yield accurate results for $\pi d/a = \pi/24 \ll 1$. This was further confirmed by the fact that using $d = 0.5$ nm for the MAW with tilted square antidots did not alter the exchange field distribution significantly.

7.3. Conclusions

We have discussed the dispersion of spin-waves in nanoscale one–dimensional magnonic antidot waveguides. In particular we have observed how an antidot's geometry can affect the said dispersion. By dint of power and phase distribution profiles of different spin-wave modes,

we have explored the origin of direct and indirect bandgaps that were encountered in the obtained dispersion relations. This understanding can be used, for example, to more readily design for the direct bandgaps and avoid the indirect ones. We have also studied the degree and nature of the inhomogeneity in the exchange field distribution around the edges of an antidot. Apart from offering a way to control the band structure of the exchange dominated spin-waves, we have also demonstrated their dependence on the exchange field profile around the antidots. We demonstrated that useful direct bandgaps can be opened at the same filling fraction without removing additional material during fabrication. Demagnetizing field profile, whose intensity here reached over $0.5M_\mathrm{s}$, is expected to affect the dispersion relations on (thousand times) greater length scales. Without considering the changes in the exchange field distribution, the same has been established by Ref. 63 in two-dimensional magnonic crystals where the hole is filled up by another magnetic material. However, forbiddingly vast computational resources will be required to obtain those results with good frequency and wavevector domain resolutions without compromising the accuracy of the dynamics.

8. Effects of Other Structural Parameters

*The periodic waveguide gives the possibility to design the selective leads which possess the filtering properties for transmitted SWs due to the presence of magnonic gaps. The position and the width of those gaps can be controlled by the structural parameters of the waveguides or by the bias magnetic field. It is also possible to design frequency dependent delay lines by exploiting the significant reduction of SW group velocity in the vicinity of magnonic gaps. The subject of periodic waveguides for SWs was extensively studied for few kinds of geometries: (i) comb-like structures and loop structures, where the SWs interference at the junctions in those brunched structures is crucial for magnonic band gap opening,[290] (ii) the waveguides with periodically corrugated edges where the periodic change of the width is the main factor responsible for the generation of the magnonic band structure,[5] (iii) the ferromagnetic stripe with periodicity of the magnetization introduced by ion implantation[291] or (iv) periodic bias magnetic field,[94] and (v) SWs waveguides with periodicity introduced by a regular repetition of the bent sections where the bending induces periodic anisotropy field.[292] The other class of the periodic waveguides are the systems with periodically placed antidots (holes),[213] which is not to be challenging for fabrication even with a resolution in the range of few nanometres.[50]

In this chapter we numerically investigate magnonic antidot waveguide (MAW) made of permalloy (Py) with air holes (i.e., antidots) placed equidistantly along the wire in its center. The considered antidot waveguide having the width and period in nanoscale will then operate in the frequency range of few tens of GHz. Here, we use two different computational

*This chapter is based upon Kłos *et al. Phys. Rev. B* **89**, 014406 (2014).

techniques, relatively fast plane wave method[58,62] (PWM) to perform systematic studies and extensive micromagnetic simulation[5,84,94,267,293] (MSs) (with the aid of OOMMF software)[250] to verify the obtained results. Similar MAW structures were already investigated in the previous papers showing that MAWs have interesting properties, which are relevant for technological applications.[4,68,213]

In Chap. 5[213] it was shown, that pinning of the magnetization at the edges of MAW can be an important factor which helps to open magnonic band gaps. Moreover, it was shown, that antidots occupying as small as 5% of the MAW surface area, are sufficient to open magnonic band gaps. In the Chap. 6[4] the influence of the intrinsic and extrinsic mirror symmetry breaking on the magnonic band gaps in MAW with pinned magnetization at edges was investigated. It was shown that small deficiencies in the symmetry of the MAW structure can result in closing magnonic band gaps but it was also demonstrated that these band gaps can be reopened by asymmetric external magnetic field. In Chap. 7[68] MAWs with comparable lattice periods and waveguide width were considered (25% of the area occupied by the antidots). The influence of the static demagnetizing field and non–uniformity of the exchange field on magnonic band structure in MAWs with various shapes of antidots were considered. Nevertheless, the influence of thorough and systematic structural changes in MAW on magnonic band structure have not yet been considered towards the optimization of MAW design. Thus, there is a need of the comprehensive studies which will thoroughly explain the impact of different structural parameters on the SW spectrum of MAW and reveal interesting properties of the magnonic band structures. Such studies are also of crucial importance for experimental realizations of MAWs with magnonic band gaps and their practical applications. In this chapter we study the influence of antidots size, lattice period, antidots shape and size factor on the dispersion of SWs and magnonic band gaps in nanoscale MAW.

This chapter is organized as follows. In Sec. 8.1 we describe the structure of the MAW and calculation methods in brief. Subsequently, we explain the magnonic band structure in MAW and the influence of the structural changes i.e., antidots size, lattice period, antidots shape and size factor in Sec. 8.2. Finally, we summarize our results and discuss the prospects of practical realizations.

8.1. The Waveguide Structure and the Calculation Methods

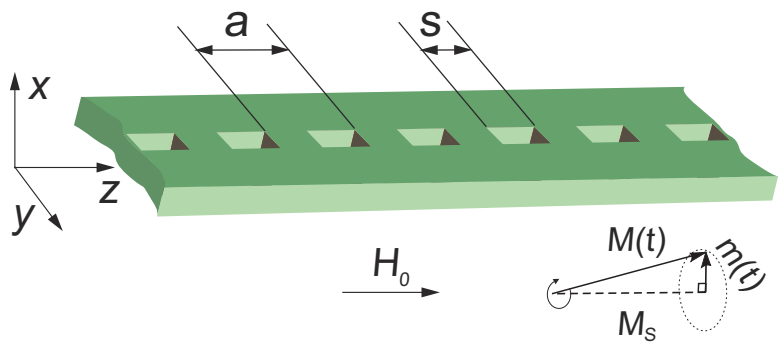

Figure 8.1.: The structure of the antidot waveguide, where the row of the equidistant square holes was placed in its center. The size s and the distance between antidots (i.e., the period of the structure a) are 6 and 15 nm, respectively. The thickness of the waveguide is 1 nm. The sketch below the waveguide structure depicts the precession of magnetization around the direction of external magnetic field H_0. Source: Ref. 66.

We study here the symmetric magnonic waveguides based on a one-dimensional (1D) antidot lattice structure shown in Fig. 8.1. It has the form of a thin (thickness 1 nm) and infinitely long permalloy ($Ni_{80}Fe_{20}$) stripe with a single row of square holes of side $s = 6$ nm disposed periodically along the central line. The stripe width and the lattice constant are fixed at 45 nm and $a = 15$ nm, respectively. The row of holes is placed at a distance of 19.5 nm from both top and bottom edges of the stripe. Thus, the waveguide possesses an axis of mirror symmetry down the middle of the waveguide. A bias magnetic field is applied along the stripe and it is strong enough to saturate the sample ($\mu_0 H_0 = 1$ T) and make the magnetization collinear and equal to its saturation value even in the regions close to the sides of the waveguide and antidot edges. The material parameters of Py are assumed in calculations.

The calculations of the magnonic band structure are performed with the PWM and the finite difference method based OOMMF. Damping is neglected in PWM calculations and included in MS ($\alpha = 0.0001$). The effective magnetic field $\mathbf{H}_{\text{eff}}$ here consists of the bias magnetic field H_0, exchange field $\mathbf{H}_{\text{exch}} = \nabla\lambda_{\text{ex}}^2\nabla\mathbf{M}$ and demagnetizing field $\mathbf{H}_{\text{dem}}$. For OOMMF calculations the standard formula for dipole-dipole interaction in the lattice of

magnetic moments was used. In our PWM implementation we use Kaczer formula[279] for demagnetising field in planar periodic structures. The pinned dynamical components of the magnetization vector were assumed at Py/air interfaces in calculations with both methods.[213] The pinning in OOMMF was introduced by fixing magnetization vector in all cells bordering the Py/air interfaces *. The boundary conditions for dynamical component of magnetization do not result from Landau-Lifshitz equation. They can results from the presence of surface anisotropy (which depends on the physical and chemical states of the surface) or from so called dipolar pinning.[255,256] Although we have limited our investigation to the case of pinned magnetization, the conclusions we draw will be still valid in systems with partially free magnetic moments on the external interfaces.[4]

The pinning at the edges of antidots forces the decay of the magnetization dynamics in the center of the MAW for small values of lattice constants a and relatively large antidot sizes s. By varying these parameters we can observe the gradual transition from the case of two weakly coupled periodic sub-waveguides (formed by each of the two semi-isolated 19.5 nm wide halves of the whole MAW) to the case of one waveguide (45 nm width, being the whole MAW) with small periodic perturbation (the further discussion with the numerical results will be presented in sub–Sec. 8.2.2). In the PWM, the pinning is exactly at the edges of Py, whereas in MS the pinning was applied in the layer of the finite thickness. This difference can slightly influence results obtained with both methods. The effect of magnetization pinning is seen in the profiles of SW dispersion relations shown in Figs. 8.2 and 8.3. Due to the small thickness of the MAW and relatively large ratio of the width to thickness of MAW, a uniform SW profile across the thickness is assumed.

8.2. The Influence of Structural Changes in the MAW on the SW Band Structure

The dispersion relation, i.e., frequency as a function of the wavevector, $f(k)$, is a periodic function with the period equal to the reciprocal lattice vector $G = 2\pi/a$. This dispersion

*In MS the discrete mesh size of $1.5 \times 1.5 \times 1$ nm^3 along X, Y and Z axis, respectively, was used. The MSs were performed for 4 ns. In the PWM we use 781, 1065, 1647 plane waves, depending on the value of the period a.

also has a mirror symmetry with respect to the point $k = 0$. Because of that it is enough to show $f(k)$ only in the half of the first Brillouin zone (BZ) but for the purpose of clarity of analysis, we will present results in the full BZ.

8.2.1. The Influence of Antidot Size

Figure 8.2 presents the SW spectra of MAW for three different sizes $s \times s$ of the square antidots: for $s = 4$, 6 and 8 nm. We kept the period of the MAW constant ($a = 20$ nm). For fixed period a, the increase of the antidot size makes the two sub-waveguides (formed by halves of MAW) more isolated, because it reduces the crosstalk between magnetization dynamics in these two sub-waveguides. It is noticeable both in the SW dispersion and in the profiles of the squared amplitudes of the dynamical magnetization in Fig. 8.2 (the profiles in Fig. 8.2 show the out-of-plane component of the magnetization vector). Let us compare two lowest modes for $s = 4$ and 8 nm denoted in Fig. 8.2 by (a) and (b). For $s = 4$ nm the lowest mode (a) is formed by strongly coupled SWs propagating in two sub-waveguides. This mode, as the lowest one, has no nodal line in the center of MAW and therefore the SWs are allowed to penetrate in the areas between the antidots. The antidot with larger size ($s = 8$ nm) can however successfully extinguish the SW dynamics in the MAW center. In this case ($s = 8$ nm) the modes (a) and (b) are almost degenerate with in-phase (a) and out-of-phase (b) SWs precession between two sub-waveguides. Their amplitudes and position of dispersion branches are almost the same. The mode (b) is however more robust to the changes in the antidot size. It is due to the fact that this mode has a nodal line in the center of the MAW, which leads to the decaying of the SW dynamics in the vicinity of the antidots row. As a result the SWs mode (b) is weakly affected by the presence of the series of antidots placed in the middle of the structure. The comparison of the maps of mode (b) for $s = 4$ nm and for $s = 8$ nm do not show significant differences.

It is also visible that the shrinking of the antidots size, from 8 nm to 4 nm splits the levels of modes (a) and (b) gradually. The difference between the frequencies of these modes become larger as the antidot sizes decreases. This increase of splitting between these modes can be attributed to increasing of dynamical coupling between SWs in sub-waveguides, as is discussed in the next paragraph. One can notice also the small changes in the position

for two lowest modes in the frequency scale. The lowering of frequency of the modes can be attributed to the slight increase in the effective width of each sub-waveguide with the reduction of the size of antidots.

The red dashed lines in the dispersion plots show the SW spectra for plain waveguide of width of 19.5 nm,[79] which corresponds to the width of single sub-waveguide with $s = 6$ nm. The artificially introduced periodicity ($a = 20$ nm) folds the parabolic dispersion branches (typical for exchange dominated regime) to the first BZ. In the considered frequency range (0-300 GHz) two folded-back dispersion parabolas are visible related to the mode confinement and quantization across the waveguide. By comparing MAW spectra to the spectrum of the plain sub-waveguide the following features can be noticed. (i) The MAW dispersion branches, which mimic the spectrum of the plain sub-waveguide (e.g., modes (a) and (b)) are confined mostly in the interior of the sub-waveguides of MAW, whereas modes of MAW completely distorted from the parabolic shape (e.g. modes (c) and (d)) have amplitudes concentrated at the row of antidots. (ii) When the interaction between sub-waveguides in MAW increases (for smaller antidot size), then the distortion of parabolic-like dispersion branches is more significant. This effect is stronger for higher modes. For our system already MAW modes related to the second parabola of plain sub-waveguide are strongly perturbed. We can recognize at least two features of such distortion: the splitting between the modes being even and odd with respect to the MAW center (e.g., modes (a) and (b)), the frequency down–shift (stronger for modes originating from the second parabola) resulting form the increase of the effective width of the sub-waveguides in MAW. For instance the modes (e) and (f) can be hardly identified as those related to the crossing of the folded arms of the second parabola in the BZ center(the modes have one nodal line in the center of each sub-waveguide). They are significantly shifted down as the antidots are reduced.

Due to the periodicity in the system the magnonic band gaps can be opened in the SW spectrum. If the periodicity can be regarded as a small perturbation in a plain waveguide possible bandgaps occur in three different scenarios: (i) at BZ edges – it happens for the lowest dispersion branch (originating from the first dispersion mode of the uniform waveguide), (ii) in the BZ center – as a result of the first self-crossing of the branches related to the same dispersion mode, after folding-back to the first BZ (only if there is no overlapping with higher

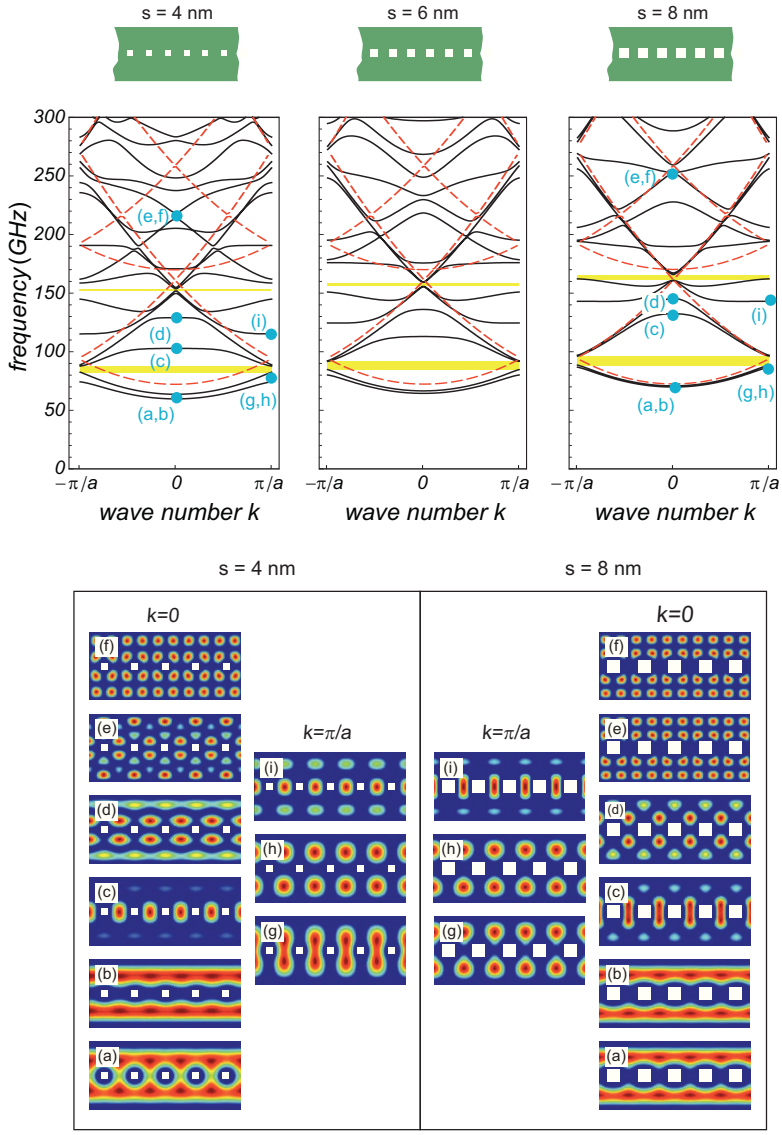

Figure 8.2.: The dependence of size of antidots on SW spectra of MAW. The inset above the central part of the figure shows the system under investigation: 1 nm thick and 45 nm wide, infinitely long Py stripe with a periodic series of square antidots of size $s \times s$, where $s = 4$, 6, and 8 nm, disposed along the waveguide with a period of $a = 20$ nm. Bias magnetic field $\mu_0 H_0 = 1$ T is oriented along the waveguide. The row of antidots divides the waveguide into two sub-waveguides. The coupling between sub-waveguides is controlled by the size of antidots with small antidots resulting in strong coupling ($s = 4$ nm) and big antidots in weak coupling ($s = 8$ nm). Red dashed lines show the dispersion for homogeneous waveguide of the width $w = 19.5$ nm with artificial folding-back of the dispersion to the first BZ. The coloured maps present the squared amplitude of the out-of-plane component of dynamical magnetization for bands marked by letters from (a) to (i) in the SW spectra. Source: Ref. 66.

modes, which can be supported by the sufficiently large value of the ratio period/width), (iii) inside of the BZ – being the effect of the anti-crossing of branches related to different dispersion modes. The scenarios (i) and (ii) are related to the Bragg scattering for the spin waves differing in wave number by $\Delta k = (2n)2\pi/a$ and $\Delta k = (2n+1)2\pi/a$, respectively, where n is integer number. Such simple picture of the mechanisms can be used for very weak periodic modulation, where the dispersive branches in the system can be referred to as modes of the plain waveguide, and does not exhaust all possible mechanisms of band gap formation.[294–296] The magnonic gaps marked by yellow bars in Fig. 8.2 are related to the first and second scenario mentioned above. The gap generated by the anti-crossing of branches related to the different dispersion parabolas of the plain sub-waveguides (i.e, the third scenario) can be observed in the first column in Fig. 8.3 (see the second gap for $a = 15$ nm). For considered range of antidot sizes ($s = 4$, 6 and 8 nm) both gaps (the first and the second one) become slightly wider with the increase in the antidot size. However, introduction of much larger antidots (when $s \approx a$) will cancel the periodicity in the system and will lead to the gaps closing. This behaviour can be understood by considering two competing mechanisms. The gap will be wide when the periodicity is strong (large antidots with the inter–antidot distance comparable to the antidot sizes) and the crosstalks between sub-waveguides are small (values of the ratio s/a close to 1 allows to separate sub-waveguides). The first condition will enhance the Bragg scattering, the second one will reduce the splitting of the even and odd modes with respect to the MAW center.

8.2.2. The Influence of Lattice Period

Figure 8.3 shows the variation in the magnonic spectra with the lattice constant ($a = 15$, 21 and 30 nm). We change the separation between the antidots keeping their size constant ($s = 6$ nm). The increase of lattice constant a contracts the size of the BZ. We decided not to change the range of the wave number k for successive values of a in Fig. 8.3. Therefore, the dispersion plots for $a = 15$, 21 and 30 nm encompass: 1, $1\frac{1}{3}$ and 2 BZs, respectively. To, discuss the impact of the lattice constant on the MAW spectrum one has to include this additional factor. The reduction of the BZ size can affect the spectrum of the 1D periodic SW waveguide in two ways: (i) The SW spectrum contains more bands in the same

frequency range. The edges of successive BZ appear more frequently in wavevector domain and therefore the dispersion foldings at the BZ edges splits the bands more often in frequency domain. (ii) The group velocity is reduced. If the spectrum is folded back multiple times, thus the number of bands reaching the BZ edge and center (where the group velocity drops to zero) increases. Both the Bragg scattering and self-crossing of bands leads to the band repulsion and their flattening.

Because of much more complex evolution of the magnonic spectrum with changes in the lattice constant, it is more difficult to trace the variations in the origin of the bandgaps width. The shrinking of the BZ (with the increase of a) changes the frequency position of the bandgaps opened at the BZ edges and can also result in opening or closing of gaps formed due to self-crossing or anti-crossing of dispersion branches. Nevertheless some characteristic features for this evolutions can be noticed. (i) The magnonic bandgaps are shifted down in the frequency range. It is caused by the dense folding of the dispersion branches in the narrower BZ. The reasonably strong bands overlapping, for larger values of a, can also close the bandgaps in higher frequency range [see Fig. 8.3 for $a = 30$ nm]. (ii) There is no simple answer to what value of a is optimal for the existence of a wide magnonic bandgap. The limits of very small and very large lattice constant (with a fixed antidot size) do not support the wide bandgaps in the system. For short periods the antidots start to overlap, which cancels the periodicity and makes two sub-waveguides isolated (in terms of exchange interactions) and the bandgap closes. In the limit of large lattice constants ($a \gg s$) the periodicity in the system can be treated as a small perturbation and therefore, the Bragg scattering should be weak and it leads to a gradual bandgap closing. But the localized modes with flat bands appear in the low frequency spectra [see mode (a) in Fig. 8.3 for $a = 30$ nm] and the simple picture does not hold.

The increase of the lattice constant with the fixed size of the antidots makes the separation between the antidots larger. For $a \gg s$, MAW can not be treated as two weakly coupled sub-waveguides. The data presented in the right column of Fig. 8.3 shows that considered system ($a = 30$ nm) is close to this limit. For even larger values of a, one may interpret the spectrum as a perturbation of the spectrum of the plain waveguide of width 45 nm (equals to the total width of MAW and shown in the right column of Fig. 8.3 with dashed lines),

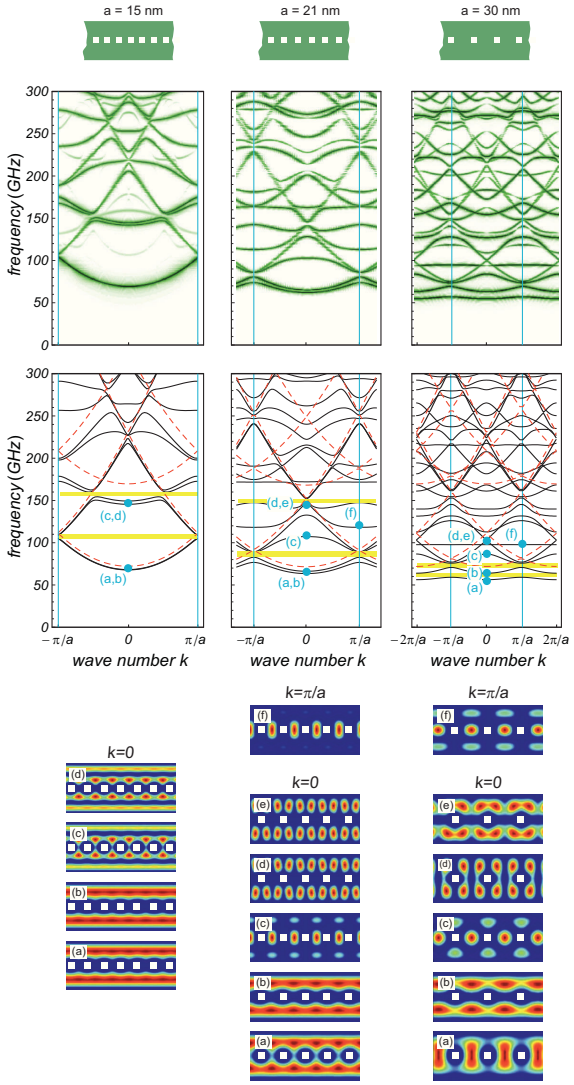

Figure 8.3.: The dependence of SW spectra of MAW on the waveguide period. The size of the antidots is kept constant $s = 6$ nm. The increase of the period (from $a = 15$ to 21 and 30 nm) leads to increase of the coupling between SWs in the sub-waveguides. Note the change in location of the BZ edges marked by blue vertical lines. In the first row schematic plots of the MAW are shown, in the second and third row the dispersion of SWs calculated by micromagnetic simulations (OOMMF) and PWM are presented respectively. Together with the PWM results the dispersion for homogeneous waveguides of width $w = 19.5$ nm (for $a = 15$ and 21 nm) and $w = 45$ nm (for $a = 30$ nm) with artificial folding-back of the dispersion to the first BZ is shown with dashed (red online) lines. The coloured maps on the bottom of the figure show the squared amplitude of the out-of-plane component of magnetization calculated with PWM for points of the magnonic band structure labelled by (a) - (f). Source: Ref. 66.

rather than those in two sub-waveguides. Let us discuss how the increase in the ratio a/s affects the spatial distribution of modes [bottom row in Fig. 8.3]. Two trends are evident.

(i) The modes localized at the antidots row are shifted to the lower frequency range. Modes (c) and (f) for $a = 21$ and 30 nm have SW amplitudes localized between the antidots. With the increase of the period the size of these areas extend; and the SWs confined in the larger areas decrease their frequencies. (ii) The modes even with respect to the MAW center, start to leak their amplitudes to the middle of MAW. For larger values of a, the pinning at the antidot edges is not sufficient to diminish the SW power at the center of the MAW even for the lowest modes. We can observe this process by analysing the evolution of modes (a) and (b) while increasing lattice constant. For $a = 15$ nm it is almost impossible to distinguish between the profiles of the (a) and (b) modes. When $a = 21$ nm the power from even mode (a) starts to penetrate in the areas between the antidots. It leads to the coupling of excitation in the two sub-waveguides and splits the dispersive branches of even (a) and odd (b) modes. The lowest mode of the large considered lattice constant $a = 30$ nm spreads its amplitude over the whole MAW width with maximum concentration in its center. Due to smoother spatial variation of the amplitude across the whole width of MAW (in comparison to the cases $a = 15$ nm or $a = 21$ nm) the frequency of this mode is lowered.

The second row in Fig. 8.3 presents the dispersions obtained from MS. The agreement with PWM is evident. The small discrepancies start to appear in the high frequency range where the bands calculated using OOMMF are slightly shifted down. This can be attributed to finite cell sizes used in the finite difference method based solver. The maximum difference between the positions of the bands calculated in OOMMF and PWM reaches about 5% at the top of the presented spectra.

8.2.3. The Influence of Antidot Shape

The effect of antidot shape on SW dispersion in MAW has been discussed in some detail for dipole dominated SWs[45,63] and exchange dominated SWs without pinning at Py/air interfaces.[68] Here, we revisit some of those findings for the completeness of this study. In order to make the systems of various antidots shape comparable, we fixed the area of the antidots independent of their shape. We compared two basic antidot shapes: the square shape and the circular shape. The results for $a = 15$ nm, $s = 6$ nm for square antidots and radius of 3.38 nm for circular antidots are presented in Fig. 8.4. The SW spectra for

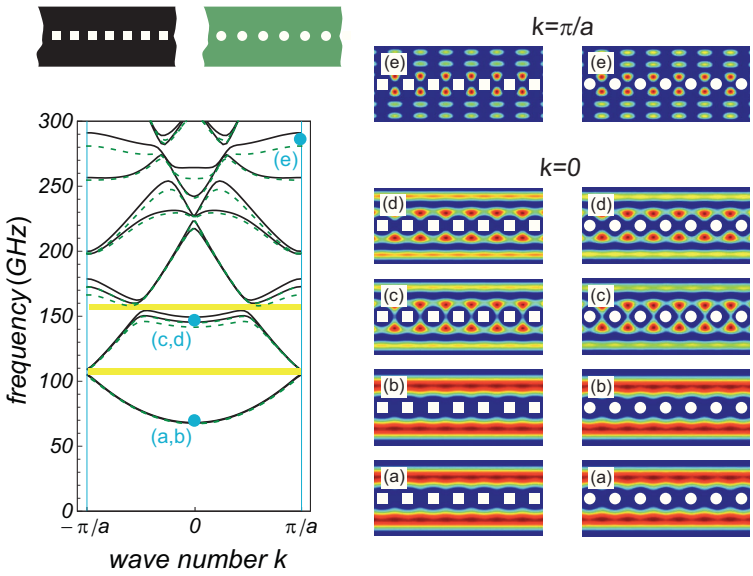

Figure 8.4.: The SW spectra for the MAW with square (black solid line) and circular (green dashed lines) antidots. The lattice constant is fixed ($a = 15$ nm) and areas of square and circular antidots are the same (36 nm^2). The maps in the two columns on the right presents the out-of-plane components of dynamical magnetization for selected modes in the center and the edge of the BZ for square and circular antidots, on the left and right, respectively. Source: Ref. 66.

these two antidot shapes do not differ significantly. The branches coinciding with the first dispersion parabola [cf. the red dashed line in the left column of the Fig. 8.3] almost overlap with other. There is no discernible difference between modes (a) and (b) for both the MAWs with square and circular antidots. The levels associated with the second dispersion parabola [e.g. modes (c) and (d)] for the MAW with circular antidots are slightly lowered in reference to the corresponding modes of the MAW with square antidots. The differences in the profiles of (c) and (d) mode are also very subtle for two considered geometries. The more pronounced dissimilarity can be noticed for the modes localized at the row of antidots (e). For this case almost all SW amplitude is focused in the vicinity of the antidots. Therefore this kind of excitation is relatively sensitive to the difference in shape of antidots, which is in fact the very small change in the geometry of the whole system. Similar effects were also found for other structures investigated in this chapter, i.e., for lattice constants 21 and 30 nm, and antidots sizes of 4 and 8 nm. Antidot geometry affects the exchange and demagnetizing field distribution around itself. Thus their periodicity in an MAW provides the periodic and inhomogeneous potential necessary for the Bragg scattering and the resultant characteristic

SW spectrum. The demagnetizing field distribution is shown to play a more prominent role on larger length scales.[63] On the considered length scales, where we have exchange dominated SWs, the spectrum is affected only if the hole shape causes the exchange field distribution to change.[68] From the application point of view, perhaps the first direct magnonic bandgap and related dispersive modes are the most important in the SW spectrum. Thus we find that, for exchange dominated SWs, even if minor periodic deformations of antidot shape occur during the fabrication of an MAW, its SW spectrum will remain practically unaffected as long as the exchange field distribution is unchanged.

8.2.4. The Influence of Size Factor

For the MAW of the width 45 nm discussed in the previous subsections, the exchange interaction dominates over magnetostatic interactions. It results from the small values of dynamic demagnetizing fields in comparison to exchange field for large values of wave numbers. Even the amplitudes of static demagnetizing field reach the values 0.1 T at the interfaces of Py/air perpendicular to the direction of external filed, which are quite small in comparison to the value of external filed 1 T and to the width of the bands [taking $\gamma\mu_0 H_{\mathrm{dm}}$ for comparison]. Therefore the SW dispersion manifest purely exchange behaviour with parabolic trend visible even for wave numbers close to the BZ center [see e.g., Fig. 8.4].

The models we use in calculations include both kinds of interactions: exchange and dipolar. To observe the noticeable impact of dipolar interaction on the SW dispersion, one has to scale up the structure of MAW. We magnified the MAW structure with square antidots presented in Fig. 8.4 by the factor of 6 [the width, thickness, antidots size and lattice constant were all increased 6 times]. For this structure in the first BZ we observe a negative group velocity near the BZ center for the first two bands [Fig. 8.5], i.e., the feature characteristic for the backward volume magnetostatic waves.[28] For lager values of the wave number, a quadratic dispersion typical for exchange interaction begin to dominate. As a result the two lowest dispersion branches have a minimum with a group velocity reaching zero away from the BZ center. The discussion of SW eigenmodes presented in the previous section has assumed the domination of exchange interactions. We have interpreted the magnonic band structure as an effect of cross-talks of two quasi-parabolic dispersion relations related to two sub-waveguides

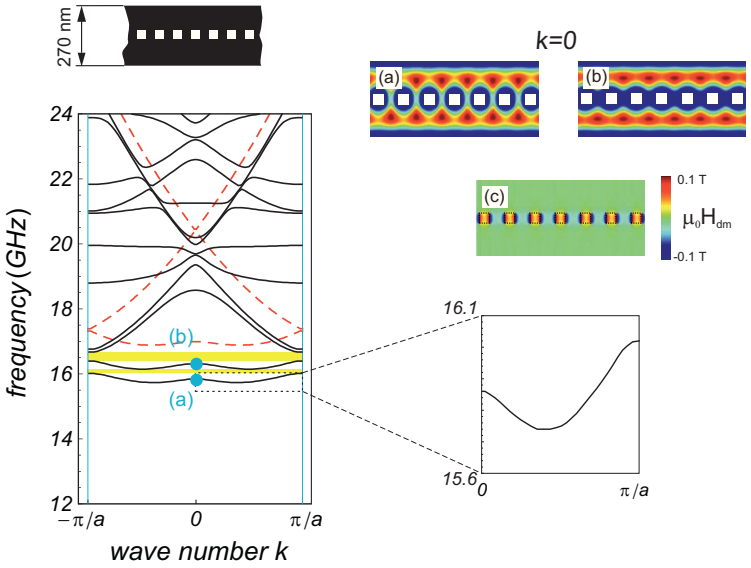

Figure 8.5.: The PWM calculations of SW spectra for the MAW magnified by the factor of 6 in reference to the structure presented in Fig. 8.4 with square holes showing the crossover of exchange and dipolar effects related to the stronger manifestation of dipolar interactions. The structural parameters are: the lattice constant: $a = 90$ nm, antidots size: $s = 36$ nm, thickness and width: 6 nm and 270 nm, respectively. Red dashed lines show the dispersion for homogeneous waveguide of the width 135 nm [i.e., half of the total MAW width]. The maps (a) and (b) presents the out-of-plane components of dynamical magnetization for two modes in the center of the BZ. (c) The map of the static demagnetizing field, its component along the waveguide, H_{dm}. The peaks of the static demagnetizing field are significantly smaller than the value of external magnetic field $\mu_0 H_0 = 1$ T. Source: Ref. 66.

folded at the edges of the BZ. From Fig. 8.5 it is clear, that even in a crossover of dipolar and exchange regime, this picture can be still valid and the spectrum presented in Fig. 8.5 preserves most of the features found for exchange dominated systems [cf. Figs. 8.2, 8.3 and 8.4]. We can also link the spectrum of the MAW [black lines in Fig. 8.5] to the spectra of homogeneous sub-waveguides [red dashed lines] as well.

One of the important differences in comparison to exchange dominated systems, is the increase of the strength of interactions between two sub-waveguides. This effect is manifested by the stronger splitting of the levels of even [Fig. 8.5(a)] and odd [Fig. 8.5(b)] modes with respect to the MAW center. The increase of the coupling between these two SW excitations in different sub-waveguides can be attributed to three factors: (i) to the enhancement of long range dipolar interactions due to increased thickness of MAW, (ii) to the decrease of

the band width [resulting from the large lattice constant and consequently smaller first BZ] and thus the relative increases of the role of a non–uniformity of the static demagnetizing field [Fig. 8.5 (c)], and finally (iii) to the increase of separation between antidots, thus the lowering of frequency of quantize SWs between neighboring antidots.

The considered regime of sizes [the width of the MAW presented in Fig. 8.5 equal to 270 nm] can be realized by a much broader spectrum of fabrication techniques which make this system more interesting from experimental point of view.

8.3. Conclusions

We have presented in-depth theoretical study of the impact of structural changes on the spin wave spectrum of the new type of thin nanoscale magnonic waveguides with the row of antidots placed in its center. The influence of the antidots size and shape, distance between antidots and the scale factor of antidots waveguides on magnonic band structure and magnonic band gaps have been investigated. These studies allow us for the identification of main parameters and mechanisms which influence the width of magnonic band gaps in nanoscale MAW. Moreover we have described the roles of exchange and dipolar interactions in the formation of the magnonic band structure in the thin MAW with widths from tens to hundreds of nm. In summary we have found that:

- The increase of antidot size in relation to the waveguide period makes the effective pinning in the center of the waveguide stronger. By controlling the strength of this pinning one can affect the crosstalk between SWs propagating in two adjacent halves of the waveguide (sub-waveguides). The gradual degeneracy of the (a, b) modes occurs as the antidot size increases.

- When the size of antidots is small enough, or the edge to edge distance between the neighboring antidots are large enough, the SWs localized on the periodic row of antidots are observed in lower frequency range (together with the lowest dispersion branches for modes propagating in sub-waveguides)–see, e.g. modes (c) and (i) in Fig. 8.2 [and also modes (c) and (f) in Fig. 8.3].

- The magnonic gaps are expected to open at the BZ edges or BZ center (Fig. 2). The gap can be opened for the intermediate values of the wave number as well, where it is caused by the anti-crossing of the bands originating from different transverse modes in homogeneous sub waveguides cf. the modes (a,b) and (c,d) in the left panel in Fig. 8.2 [modes (a,b) and (c,d) differ in the number of horizontal nodal lines] and the second gap in this sub-figure [$a = 15$ nm, $s = 6$ nm].

- When the waveguide period a is fixed then the existence of magnonic band gap and change of its width and position is easier to analyse as a function of the antidot size s [Fig. 8.2], than for the opposite case, s fixed and a–varied [Fig. 8.3]. It is because a change in a alters not only the strength of the periodicity but also affects the location of BZ edges. Nevertheless, the period of the MAW, and its relation to the antidots size, are important factors which influenced magnonic band gaps and the group velocity of SW. Thus, its proper choice will be crucial for application of nanoscale MAW in magnonics, to transmit or filter SW signals.

- The shape of the antidots does not affect the SW spectrum of exchange dominated SWs unless the exchange field distribution is altered. High frequency modes, which contain power close to the row of antidots show greater sensitivity towards changes in the shape of the antidots. Thus for modes from the low frequency part of the spectra the antidots shape is not important parameter in nanoscale MAW.

- Enhancement of the size of the MAW increases the crosstalk between SWs propagating in two adjacent halves of the waveguide (sub-waveguides) and the backward volume magnetostatic wave character of dispersion relation near BZ center for these SWs is found. But still the main features the magnonic band structure in the exchange dominating systems are preserved.

Thus, we have shown that SW waveguides based on thin ferromagnetic stripes with single row of periodically spaced antidots in nanoscale are promising for magnonic applications in frequencies from few to tens of GHz. Only a single row of antidots offer enough room for manipulation of the SW spectra to design single mode waveguides or waveguides with filtering properties due to existence magnonic band gaps. The insensitivity of main part of the